NORTHWESTERN UNIVERSITY

Breakout Reactions from the CNO−cycle

A DISSERTATION

SUBMITTED TO THE GRADUATE SCHOOL

IN PARTIAL FULFILLMENT OF THE REQUIREMENTS

for the degree

DOCTOR OF PHILOSOPHY

Field of Physics and Astronomy

By

Louis Joseph Jisonna, Jr.

EVANSTON, ILLINOIS

December 2008

ABSTRACT

Breakout Reactions from the CNO−cycle

Louis Joseph Jisonna, Jr.

Breakout reactions from the CNO cycles leading into the *rp*-process in explosive stellar hydrogen burning environments have been studied using the Argonne Tandem Linac Accelerator System (ATLAS). Earlier work is reported and summarized with an introduction to the beam, target and detector development in the nuclear astrophysics group at Argonne National Laboratory. The ^{18}Ne(α,p)^{21}Na reaction has been studied via the time inverse reaction p(^{21}Na,α)^{18}Ne. A 5×10^{-5} particle nanoamp ^{21}Na beam was produced at the ATLAS in-flight facility via the p(^{21}Ne,n)^{21}Na reaction. Cross sections were obtained at five energies covering the region between $9.4 \leq E_x \leq 9.9$ MeV in the compound nucleus ^{22}Mg, and compared with previous measurements. The ^{19}Ne(p,γ)^{20}Na reaction was also studied by populating proton unbound states via the ^{3}He(^{20}Ne,t)^{20}Na* reaction. We have observed for the first time evidence for the γ-decay of the astrophysically important 2.645 MeV state in ^{20}Na. Branching ratios obtained for the first two proton unbound states in ^{20}Na were $\Gamma_p/\Gamma_\gamma(2.645\ \text{MeV}) = 15.1^{+28.8}_{-8.9}$ and a lower limit of $\Gamma_p/\Gamma_\gamma(2.849\ \text{MeV}) \geq 26.0$ (1-σ CL). The experimental branching ratios were compared with theoretical predictions

based on shell-model calculations and on the properties of mirror states in ^{20}F. Our results favor a $J^\pi = 1^+$ assignment for the 2.645 MeV state and a $J^\pi = 3^+$ for the 2.849 MeV at the 1-σ confidence level. Our result also suggests that the resonance strength for radiative capture through the 2.645 MeV state is close to the value $\omega\gamma \approx 6$ meV, in agreement with the value calculated assuming it to be the mirror of the 3.172 MeV intruder state in ^{20}F with a $6p2h$ configuration.

Acknowledgements

The author would like to acknowledge the many people who have contributed to this work and those who have enriched my life both professionally and personally.

First and foremost, I would like to thank my thesis advisor, Ralph Segel, for his generous support and for seeing this project through to the end, for pushing me forward when I needed to be pushed and for acknowledging that life existed outside of graduate school. His painstaking efforts in editing this document were greatly needed and appreciated. Thanks to the Northwestern University Physics and Astronomy faculty and staff; to Dave Buchholz and Ron Taam for their suggestions and corrections on this document and for serving on my thesis committee, to Farhad Zadeh-Yusef and Michael Smutko for letters of recommendation, and to Anupam Garg and Heidi Schellman for spending their summers coaching the qualifying exam "boot camps."

I would also like to thank my collaborators at Argonne National Lab for their technical instruction and support throughout my long tenure; especially my supervisor, Ernst Rehm, for his patience in answering my questions for the third and fourth times, for suggesting experiments and steering them through the various committees, and for editing this manuscript; Alan Wuosmaa, for mentoring and teaching me many aspects of experimental nuclear physics and for his friendship; Robert Janssens, for encouraging me to continue to pursue my goal and for generously offering his advice and support; Cheng-lie Jiang for teaching me the data acquisition and analysis packages and how to interpret

the results; Ken Teh, Don Cyborski, Torben Lauritsen, and Dave Potterveld for their help and support with computer related issues inherent in continually switching between Linux, VMS, Sun, and Windows based operating systems; Dale Henderson for his technical assistance with the detectors and gas handling system; the ATLAS operators for providing beams and for many interesting discussions during the overnight shifts; and Colleen Tobolic for moral support and for being a great listener!

Many other scientists, staff members, post docs, and fellow students also helped pass the many hours spent at the lab, in particular, Jason Clark, Xiadong Tang, Xiaofeng Wang, Shrabani Sinha, Hye Young Lee, Bill Sheehan and the Argonne Aikido Club.

Thanks to Don Peterson and Paul DeYoung for their expertise and assistance in translating this document into LaTeX and to Catherine Mader for converting some of the figures.

Special thanks to my fellow graduate students and post-docs at Northwestern who helped keep me sane during those first few years of courses and for their help and friendship: especially, Megan Krejny, Bram van Rens, Anne Dabrowski, Pratim Sengupta, Dale Stentz and Silvia Goy-Lopez; and to Harald Fox, Victoria Martin and Ed Wang for their continuing friendship. Props to Michael Smutko and the Dearborn Observatory folks for keeping the public observing sessions going, providing a wonderful diversion from the endless homework assignments.

Very special thanks to Tammie Page for her love and friendship and for giving me something to look forward to after many long days at the lab and for inspiring me to start running again; and to Judith Caballero for inspiring me to pursue an advanced degree and for her love and support during my undergraduate years in Arizona.

Finally, I would like to thank my family, who has not seen much of me over the past decade: my mother, Barbara Webb, for her unconditional love and acceptance and for supporting and believing in me; my brother, Chris Webb, and my sister-in-law Angela, for keeping me centered and in touch with life outside of academia; my sister, Stephanie Szorenyi and her family for their love and for supporting my sushi habit.

A special debt of gratitude is owed to Dr. Gary Mechler, who refueled my passion for science and astronomy, helped me learn how to think critically, and started me on this long journey, graciously offering personal advice, guidance and friendship along the way.

Preface

A long time ago in a galaxy far, far away...

I started graduate school.

Table of Contents

List of Tables

List of Figures

Introduction

Over the past few decades, there has been much interest and emphasis on making laboratory-based measurements of a wide range of observed cosmic phenomena from the afterglow of the primordial Big Bang to supernova explosions. The far-reaching goals of nuclear astrophysics are to understand these phenomena, to explain the astronomical observations such as the light curves of explosive events and the cosmic abundances of the elements, and to incorporate these into a coherent picture of the observable universe. Many of these phenomena are understood to be the result of nucleosynthesis, which provides the energy that powers the stars and "cooks" the lighter elements into heavier elements. Nuclear burning processes also define the various stages of stellar evolution, and can be classified into two major categories – quiescent (or "normal"), and explosive. Normal burning involves primarily reactions with stable isotopes, while explosive processes, such as supernovae, novae and X-ray bursts (XRBs), involve unstable nuclei. The available nuclear fuel (composition) and physical conditions (temperature and density) determine the type of nuclear processes involved and the rate at which they occur. Nuclear reactions that bridge the gap between quiescent and explosive processes in novae and X-ray bursts are of particular interest. In proton-rich environments, three reaction pathways have been identified that can bridge this gap. All three of these reactions have been studied using the Argonne Tandem Linear Accelerator System (ATLAS).

This thesis describes the experiments performed at ATLAS to study these reactions, with particular emphasis on the ^{19}Ne(p,γ)^{20}Na reaction. Chapter 1 provides the background and astrophysical motivation for this work, beginning with a brief outline of the astrophysical environments for stellar hydrogen burning in Section 1.1. The CNO-cycles and "breakout" are defined in Section 1.2, and a brief introduction to the theoretical nuclear astrophysics needed for this thesis is given in Section 1.3. A brief summary is provided in Section 1.4. Chapter 2 describes the experimental methods used in this work including the production of radioactive ion beams in Section 2.1. A brief description of the targets used is given in Section 2.2. The detection techniques, detectors, and experimental setups are described in Section 2.3. A survey of the earlier work is given in Chapter 3. Chapter 4 describes the two experiments that were performed to study the ^{19}Ne(p,γ)^{20}Na reaction by determining the resonance parameters of the 2.645 MeV state in ^{20}Na. Conclusions and future outlook concerning the ^{19}Ne(p,γ)^{20}Na reaction are discussed in Chapter 5.

CHAPTER 1

Nuclear Astrophysics Background and Motivation

1.1. Astrophysical environments and conditions

Many nuclear processes occur in stellar environments, which have been proposed and summarized in the seminal "B^2FH" paper [**13**]. The primary focus of this thesis is on hydrogen burning. Two general classifications discussed in the literature are referred to as "normal" or quiescent burning, and "explosive" burning, also known as thermonuclear runaway [**14, 3**]. These terms reflect the rate at which the energy is generated in various astrophysical environments. The following is a brief summary of the physical conditions present where the H-burning plays a significant role. Estimates of the temperatures and densities in the various astrophysical environments are used to determine the important nuclear reactions and the energies at which they take place.

1.1.1. "Normal" or quiescent stellar hydrogen burning environments

"Normal" or quiescent stellar H-burning refers primarily to the way stars generate energy in their cores during the main sequence phase of stellar evolution by converting hydrogen into helium. The two major processes by which stars convert hydrogen to helium are called the Carbon-Nitrogen-Oxygen (or CNO-) cycle, described in Section 1.2, and the proton-proton (or *pp*-) chain[a]. The CNO cycle, independently proposed by Bethe [**16**]

[a]The *pp*-chain is not relevant for the purposes of this thesis. For details, see the Rolfs & Rodney [**2**], or Clayton [**15**] texts.

and von Weizsäcker [**17**], is the dominant source of energy generation in the cores of stars with masses greater than ≈ 1.5 times the mass of the sun[b]. One solar mass is $\approx 2 \times 10^{33}$ grams and is commonly denoted $M_{\odot}$. Temperatures in the core typically range from $T_9 \approx 0.01$ – 0.05, where T_9 is in units of 10^9 K (also denoted GK), at densities of $\rho \approx 2$ – 200 g cm^{-3}. Under these conditions, the stellar plasma behaves as a "normal" gas, i.e. one that obeys the ideal gas equation of state[c], $PV = NkT$, which serves as a regulatory mechanism on the nuclear reaction rates and allows normal stars, with M $\approx 1\ M_{\odot}$, to burn hydrogen at a relatively constant rate for periods of the order of 10^9 years.

Quiescent H-burning also occurs in the shells of stars during the asymptotic giant branch (AGB) phase. Shell burning requires higher temperatures, $T_9 \approx .05$ – .08, to offset the lower densities $\rho \approx 2 \times 10^{-2}$ g cm^{-3} outside the core [**1**]. Shell burning is also regulated by the ideal gas equation of state.

1.1.2. Explosive hydrogen burning environments

Explosive hydrogen burning ([**14**], reviewed in [**3**]) is associated with stellar explosions such as novae and X-ray bursts (XRBs). Both novae and XRB's have been observed to be recurrent events. The "standard" scenario for both events is similar and is shown in Figure 1.1. They are both attributed to binary star systems, consisting of an evolved, compact star and a normal or red giant star, separated by distances small compared to

[b]Bethe originally called it the CN-cycle and proposed it as the dominant source of energy production in the Sun. It was later determined that the core temperatures in the Sun were too low. (Rolfs & Rodney [**2**])

[c]The equation of state usually varies as a function of the stellar radius. For the purposes of this discussion, it is sufficient to note that the behavior of the gas in the nuclear burning region can be described by the ideal gas law.

the sum of their diameters. For novae, the compact object is a white dwarf, for XRBs the compact object is a neutron star.

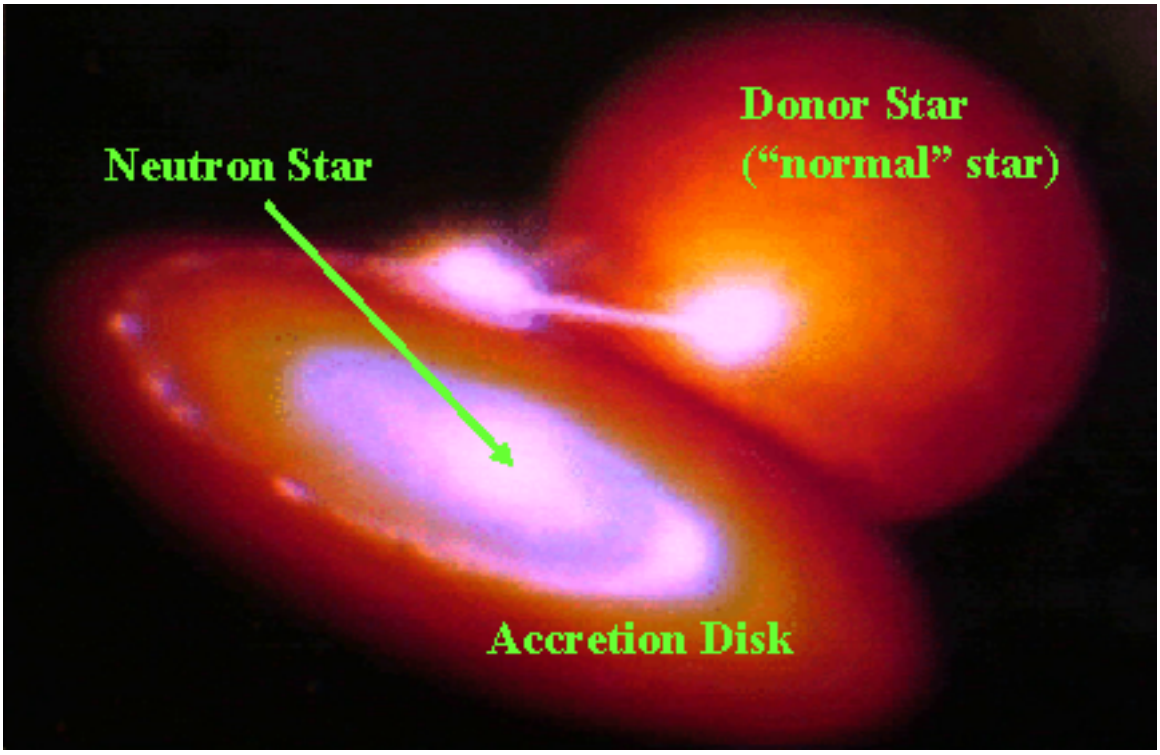

Figure 1.1. The "standard model" scenario for X-ray bursts and Novae. A binary system consisting of a "donor star," and a compact object such as a neutron star or white dwarf, are gravitationally bound in a close orbit. Hydrogen rich material from the outer envelope of the normal star is transferred to the compact object via an accretion disk. When the material falling onto the object ignites, the resulting thermonuclear runaway produces a dramatic increase in luminosity.

In a close binary system, the gravitational and tidal forces of the two objects form an equipotential surface called the Roche lobe and cancel at the Lagrange point, L_1. For each star, material contained within its Roche lobe is gravitationally bound to that object. When the outer radius of the larger star extends beyond its Roche lobe, the hydrogen-rich material can be transferred to the compact star, usually via an accretion

disk [**18, 19**]. As the material falls onto the surface of the compact star, it is compressed and heated until it ignites under degenerate gas conditions. The temperature, and hence the rate of the nuclear reactions, increases rapidly resulting in an explosive outburst or thermonuclear runaway [**20**], which is observed as a sharp increase in luminosity over a short period of time, followed by an exponentially decaying tail. Typical temperatures during the outburst range from $T_9 \approx 0.2 - 0.35$ in novae and occur on a timescale of 10^3 to 10^4 seconds with an increase in luminosity of $\approx 10^4 - 10^6$. Because of the higher temperatures $T_9 \approx 0.5 - 2$ and densities $\rho \approx 10^6$ g cm^{-3} near the surface of the neutron star, thermonuclear ignition is thought to occur via the hot CNO cycles, which are described in the next section. The initial phase of the burning is temperature independent [**1**] so, as the temperature increases the energy generation remains constant. A thermonuclear runaway cannot occur until the energy generation becomes sensitive to temperature. For XRBs, the HCNO cycles occur on a timescale of ≈ 200 s, while the thermonuclear runaway during which the energy generation increases from 10^{17} to 10^{19} erg g^{-1} s^{-1}, occurs in less than a second [**14**]. The rapid increase in the energy generation rate is the signature of CNO cycle breakout processes. In this case, the runaway is believed to be initiated by helium burning via the triple-α process and by the ^{15}O(α,γ)^{19}Ne reaction. Shortly after the ignition, when the temperature reaches $T_9 \geq 0.3$, the ^{18}Ne(α,p)^{21}Na reaction begins to dominate over the β-decay ^{18}Ne(e$^+\nu$)^{18}F ($\tau_{1/2} = 1.67$ s), rapidly converting the CNO isotopes into heavier nuclei via the *rp*-process. Therefore, an experimental rate for the ^{18}Ne(α,p)^{21}Na reaction is necessary to constrain the theoretical calculations for this phase of the runaway. Temperatures continue to rise to $T_9 \approx 0.8 - 2$ at densities $\rho \approx 10^6$ –

10^7 g cm^{-3}, depending on the column depth in the accreted layer where the burning is initiated.

The temperature and density regimes for these various astrophysical environments are illustrated in Figure 1.2.

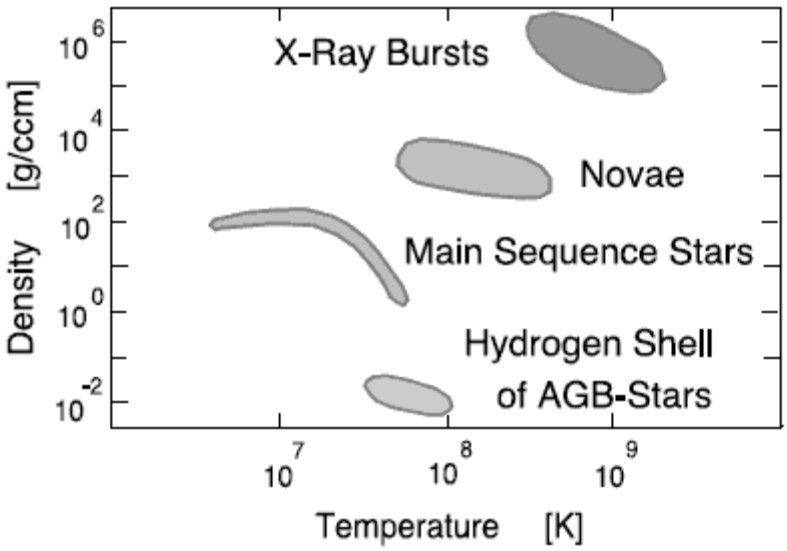

Figure 1.2. Density and temperature conditions in various astrophysical environments. (Taken from Ref [**1**])

For explosive hydrogen burning, the CNO cycles initially play an important role. However, they are insufficient to produce the observed increase in luminosity in novae and XRBs. Rapid proton capture, or the *rp*-process, is expected to be the major source of energy generation in these events. Nuclear reactions that provide a link between these two reaction networks are of particular interest. The network calculations used to model these phenomena depend critically on the associated reaction rates [**1**], particularly for the slowest, or "bottleneck", reactions. For these "key" reactions, experimental data is necessary to constrain the reaction rates, and hence, to accurately model these phenomena.

The reaction networks and the critical reactions that have been identified are described in the following section.

1.2. The CNO-cycles, HCNO- cycles, and "breakout" reactions

1.2.1. The CNO cycles

The standard CNO cycle is a closed network of nuclear reactions consisting of radiative proton captures, β-decays and a (p,α) reaction that convert hydrogen to helium in stellar environments, using carbon and nitrogen as catalysts. This CNO cycle proceeds through the following series of reactions

$$^{12}\mathrm{C(p,}\gamma)^{13}\mathrm{N}(\beta^{+}\nu_{e})^{13}\mathrm{C(p,}\gamma)^{14}\mathrm{N(p,}\gamma)^{15}\mathrm{O}(\beta^{+}\nu_{e})^{15}\mathrm{N(p,}\alpha)^{12}\mathrm{C}.$$

The net result is the conversion of hydrogen into helium, releasing energy:

$$4p \rightarrow \alpha + 2\nu_{e} + 2\beta^{+} + \ 24.688 \text{ MeV} \tag{1.1}$$

This reaction sequence is sometimes referred to as the "cold" CNO cycle. For quiescent burning, the energy generation rate depends on the rate of slowest reaction in the sequence, which is the proton capture on ^{14}N. The proton capture rate is hindered by the Coulomb barrier, and because the particle velocities and hence, their energies, are described by a Maxwell-Boltzmann distribution function (Section 1.3, the reaction rate is temperature dependent. Therefore, increasing the temperature increases the rate at which energy is generated. At higher temperatures, proton capture on higher Z nuclei becomes possible and more reaction channels become available, leading to additional CNO-cycles, illustrated in Figure 1.3. Each of the four CNO-cycles yields the same net result as Eqn

(1.1); four hydrogen nuclei are converted to one helium nucleus, releasing the same amount of energy per cycle.

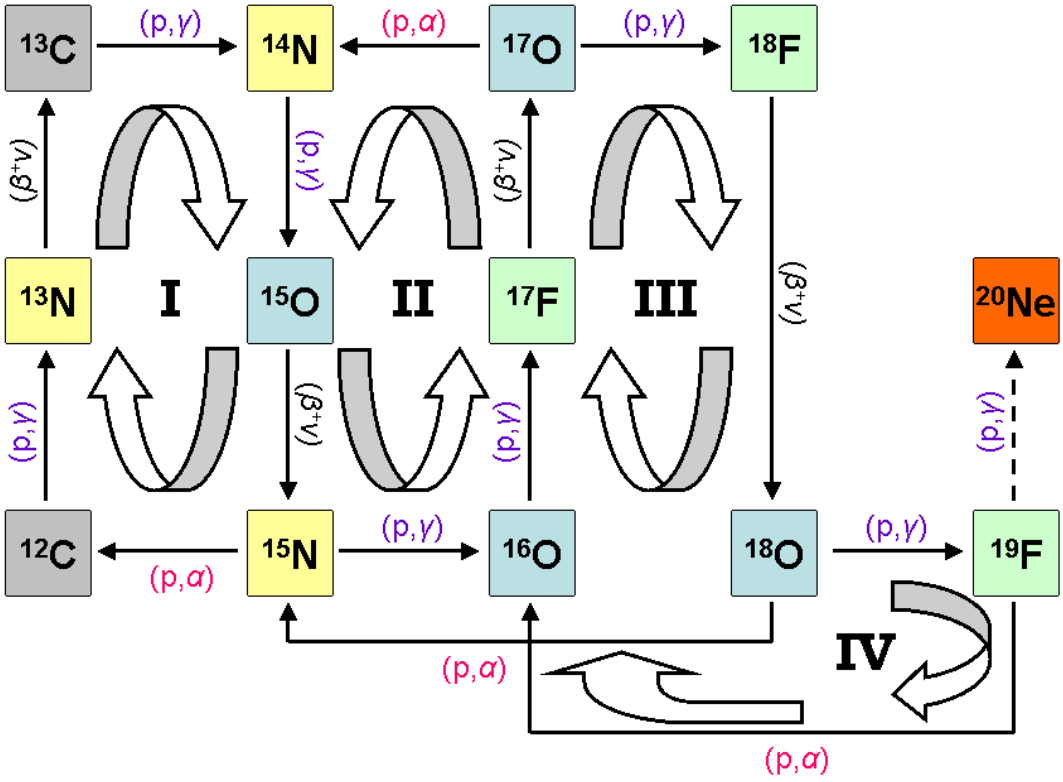

Figure 1.3. Schematic representation of the four CNO cycles. Cycle I, also called the CN-cycle, was first proposed by von Weisäcker and by Bethe. Cycles I and II are collectively known as the CNO bi-cycle. The exact pathway along this network depends on temperature, density and composition. Multiple cycles may operate simultaneously. (Rolfs & Rodney [**2**])

1.2.2. The hot-CNO cycles

The energy generation rate of the CNO-cycles continues to increase with temperature until the timescale for proton capture on ^{13}N becomes comparable to the β-decay lifetime

of ^{13}N ($\tau_{1/2}$ = 9.97 minutes). At this point, the ^{13}N($\beta^+\nu$)^{13}C decay is bypassed by the ^{13}N(p,γ)^{14}O reaction, leading to the reaction sequence

$$^{12}\text{C(p,}\gamma)^{13}\text{N(p,}\gamma)^{14}\text{O}(\beta^+\nu)^{14}\text{N(p,}\gamma)^{15}\text{O}(\beta^+\nu)^{15}\text{N(p,}\alpha)^{12}\text{C}.$$

The net result is the same as for the "cold" CNO cycles. However, the energy generation occurs at a much faster rate and continues to increase with temperature. In order to proceed to heavier nuclei the reaction network must bridge the proton-unbound nuclei ^{15}F and ^{16}F. Because these nuclei are unbound, the conversion rate of hydrogen to helium becomes limited by the β-decay of the so-called "waiting point" nuclei ^{14}O and ^{15}O, with $\tau_{1/2}$ = 70.6 and 122.2 s, respectively. The energy generation rate reaches an upper bound and becomes independent of temperature. For this reason, the resulting network of reactions is called the β-limited, or hot-CNO (HCNO) cycle. When the temperatures reach $T_9 \approx 0.4$, α-induced reactions become competitive, which bypass the waiting point nuclei via the sequence [**3**]

$$^{14}\text{O}(\alpha\text{,p})^{17}\text{F(p,}\gamma)^{18}\text{Ne}(\beta^+\nu)^{18}\text{F(p,}\alpha)^{15}\text{O}.$$

Because ^{19}Na is proton unbound proton capture on ^{18}Ne cannot take place, but because the ^{18}Ne half-life, $\tau_{1/2}$ = 1.67 s, is shorter than that of ^{14}O and ^{15}O, ^{18}Ne is not considered a "waiting point" of the network. However, the production of ^{18}Ne provides another possible path for higher mass flow as discussed in the following section.

1.2.3. Breakout reactions

For temperatures $T_9 \geq 0.5$, additional α-induced reactions, such as (α, γ) and (α,p), can occur that produce nuclei that do not cycle back into CNO material. This leakage of CNO material into heavier elements is commonly referred to as "breakout" from the

CNO-cycles. The nucleus ^{19}Ne is an important gateway since the reaction Q-values for nuclei with A $\geq$ 20 prohibit any sequences that can cycle back into CNO material. The nucleus ^{19}Ne β-decays, with $\tau_{1/2}$ = 17.22 seconds, to ^{19}F which, at lower temperatures[d] and densities, cycles back into CNO material via ^{19}F(p,α)^{16}O(p,γ)^{17}F (see Figures 1.3 and 1.6). The following three breakout reaction pathways through or around ^{19}Ne have been identified:

a. ^{18}F(p,γ)^{19}Ne(p,γ)^{20}Na

b. ^{18}Ne(α,p)^{21}Na

c. ^{15}O(α,γ)^{19}Ne(p,γ)^{20}Na

All three of these pathways have been investigated at ATLAS. The ^{18}F(p,γ)^{19}Ne reaction in path (a) was studied prior to this work and the results are summarized in Section 3.1. Path (b) has been studied via the time-inverse reaction ^{21}Na(α,p)^{18}Ne and the results are reported in Section 3.2. The last pathway (c) has been studied in two parts. The ^{15}O(α,γ)^{19}Ne reaction was studied by populating states in ^{19}Ne and observing the decay particles, as described in Section 3.3. The ^{19}Ne(p,γ)^{20}Na reaction, which is the primary focus of this thesis, is discussed in Chapter 4.

The HCNO cycles and breakout reactions are shown schematically in Figure 1.4.

As stated previously, HCNO-cycle breakout is characterized by an increase in the energy generation rate by a factor of 100 or more than given by the HCNO cycle alone [**14**]. Figure 1.5 shows the energy generation rate vs. temperature calculated for solar H and He abundances at $\rho = 10^6$ g cm^{-3}. After breakout, explosive H-burning proceeds

[d]Typically, for temperatures $T_9 \approx 0.3$, the β-decay rate of ^{19}Ne can compete with the proton capture rate. The critical temperature at which proton capture becomes dominant strongly depends on the density and composition of the accreted material, and on the depth in the accreted layer where ignition takes place. (Fisker, et al 2007)

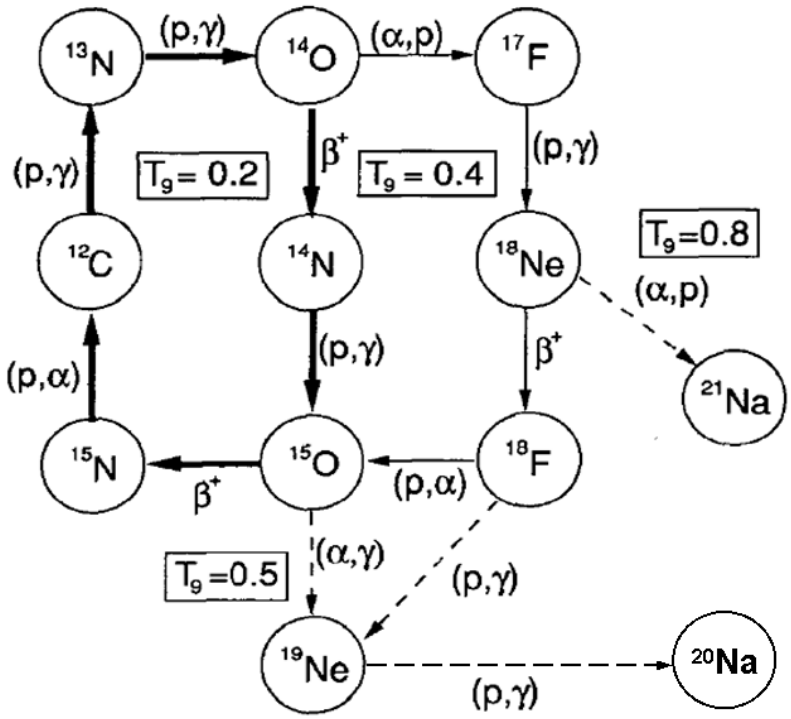

Figure 1.4. The HCNO cycles and onset temperatures for each breakout path. The dominant path is shown by the heavy arrows. The weaker path becomes important at higher temperatures, indicated by the lighter arrows. The three possible breakout paths are depicted by the dashed arrows. (Adapted from Ref [**3**])

through a series of (p,γ) and β^+-decays, which can compete with (α,p) reactions for some nuclei, quickly producing elements up to and beyond the iron group. The process is qualitatively similar to the r-process for rapid neutron capture, and has therefore been called the rapid proton (*rp*) process.

The CNO-cycles, breakout paths, and onset of the *rp*-process are shown in Figure 1.6 (taken from [**4**]). The neighboring neon-sodium (NeNa) and magnesium-aluminum

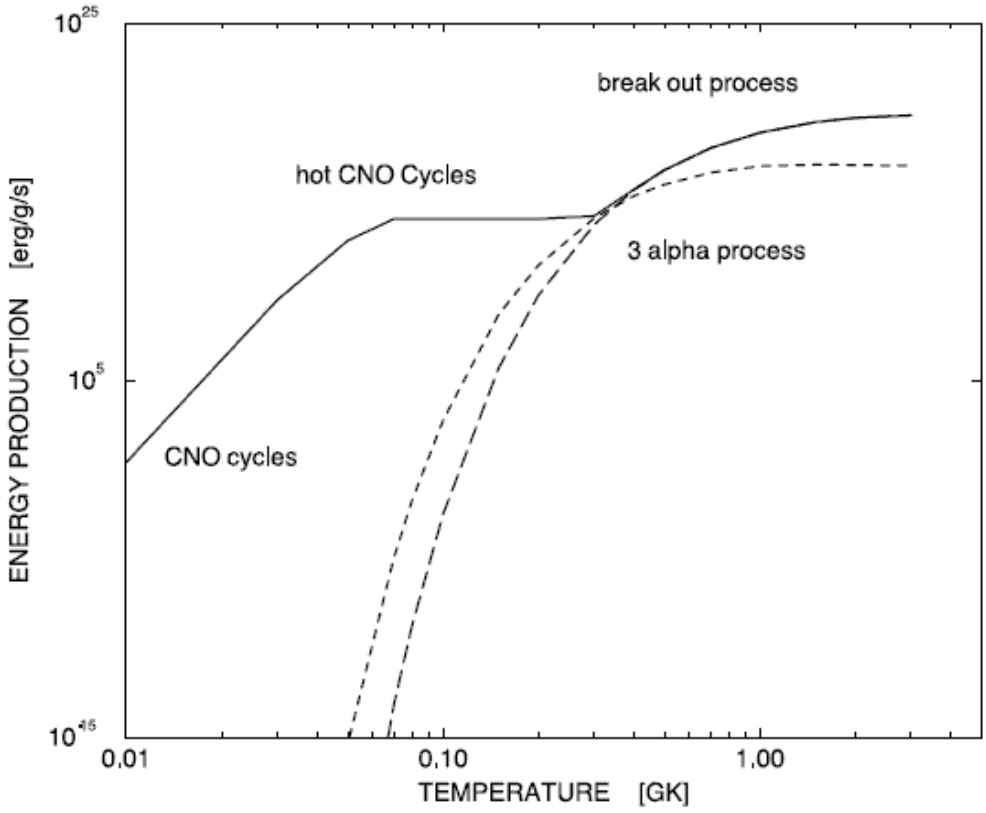

Figure 1.5. Energy generation as a function of temperature for the CNO-cycles and breakout. (Taken from Ref [**1**]) The flat region is characteristic of the hot CNO cycles. Thermonuclear runaway can be triggered by either the triple-α process (dotted line) or by the CNO-breakout processes such as the ^{15}O(α,γ)^{19}Ne reaction. For solar hydrogen and helium abundances at a density of $\rho = 10^6$ g cm^{-3}, the ignition temperature for thermonuclear runaway is $\approx$ 0.3 GK.

(MgAl) cycles as well as α-induced reactions are also shown for completeness. The NeNa- and MgAl-cycles are not the subject of this thesis. However, it should be noted that these (and other) cycles might occur simultaneously whenever these isotopes are present, whether or not CNO-cycle breakout occurs.

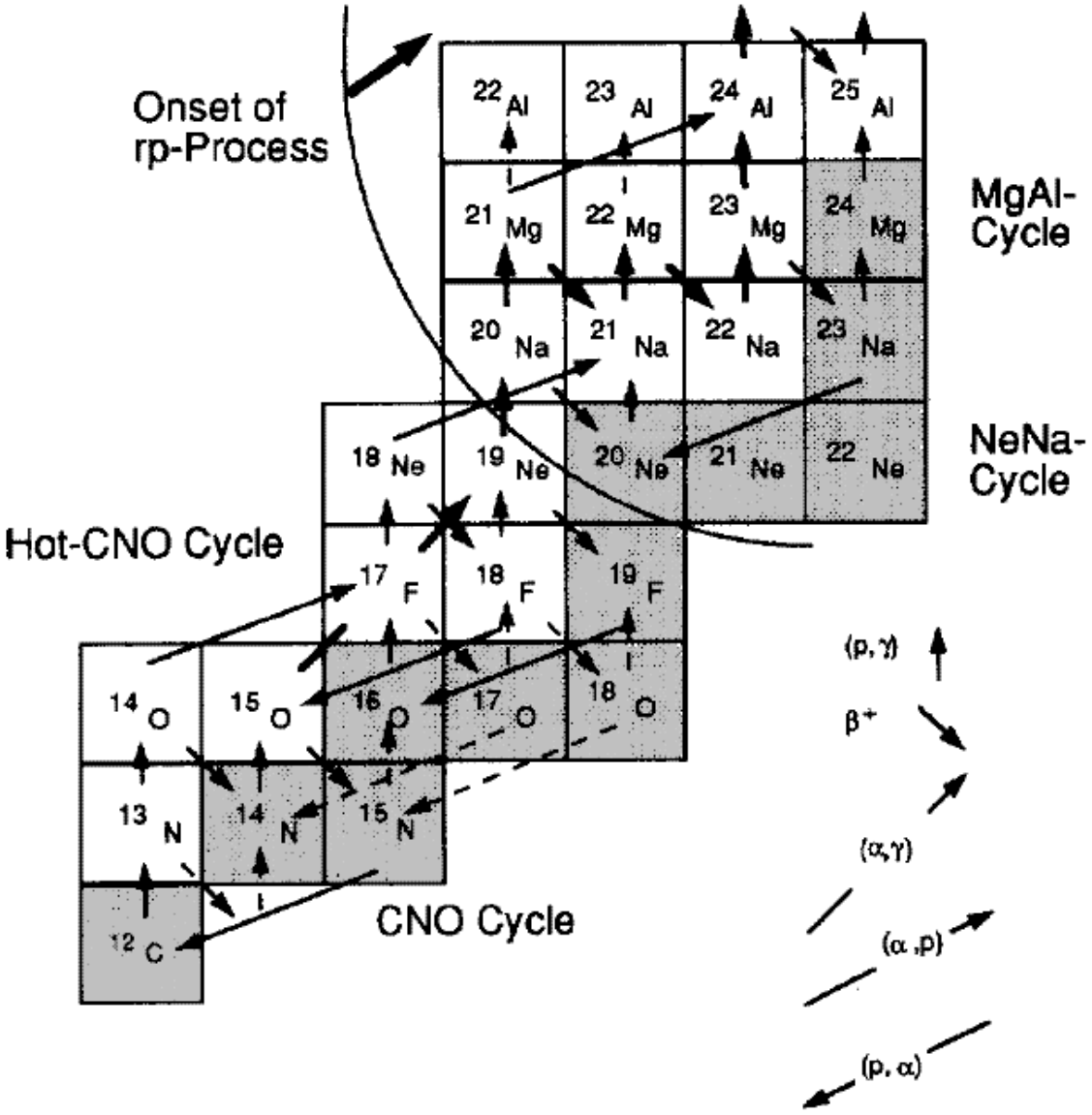

Figure 1.6. The CNO and hot CNO cycles and onset of the *rp*-process. Another way to represent a nuclear reaction network schematically is to show the region of interest in the Chart of the Nuclides, with proton number (Z) vs. neutron number (N). The nuclei shaded in gray are stable and the arrows indicate the various reaction paths. ^{19}Ne has been referred to as a gateway for breakout as described in the text. (Taken from Ref [**4**])

1.3. Relevant Nuclear Astrophysics

1.3.1. Reaction rates for non-resonant processes

This section introduces the nuclear astrophysics[e] relevant for this thesis. The quantity of astrophysical interest is the thermonuclear reaction rate, which for a reaction of the form $1 + 2 \rightarrow 3 + 4$, is given by

$$r = N_1 N_2 \int_0^\infty \sigma(v)\Phi(v)\, v dv \tag{1.2}$$

where N_1 andN_2 represent the number of particles 1 and 2 respectively. The integral, which represents the reaction rate per particle pair, contains the nuclear reaction cross section σ(v) folded with the Maxwell-Boltzmann velocity distribution Φ(v)

$$\Phi(v) = 4\pi \left(\frac{\mu}{2\pi kT}\right)^{3/2} v^2 \exp\left(-\frac{\mu v^2}{2kT}\right) \tag{1.3}$$

where μ is the reduced mass, k is the Boltzmann constant, T is the temperature, and v is the relative velocity between particle 1 and particle 2. The cross section, σ(v) depends on the relative velocity of the two particles which is determined by the Maxwell-Boltzmann distribution. The quantity r in Eqn (1.2) therefore represents the probability that a thermonuclear reaction will occur. In terms of particle energy the reaction rate per particle pair can be expressed

$$\langle \sigma \mathrm{v} \rangle = \sqrt{\frac{8}{\pi\mu}} (kT)^{-3/2} \int_0^\infty \sigma(E)\, E \exp\left(-\frac{E}{kT}\right) dE \tag{1.4}$$

[e]For a more complete treatment, see Rolfs & Rodney [**2**] or Clayton [**15**].

The total reaction rate (Eqn 1.2) can be written as

$$r_{12} = N_1 N_2 \langle \sigma \mathrm{v} \rangle \tag{1.5}$$

The energy generated by a nuclear reaction is the Q-value, which for the reaction 1 + 2 $\rightarrow$ 3 + 4, is given by[f]:

$$Q = (m_1 + m_2 - m_3 - m_4)\, c^2 \tag{1.6}$$

The energy generated in a thermonuclear reaction is given by the product of the total reaction rate and the Q-value, $\varepsilon_{12} = Q r_{12}$, and has units of ergs s^{-1} cm^{-3}. This quantity is usually written in terms of the density ρ of the stellar material, so that $\varepsilon_{12} = Q r_{12}/\rho$, in units of ergs s^{-1} g^{-1}. For energy to be released in a given reaction, the Q-value must be positive. However, at high enough temperatures, the inverse reaction can also occur (3 + 4 $\rightarrow$ 1 + 2), which is endoergic with $\varepsilon_{34} = -Q r_{34}/\rho$. Then the net energy generated is given by

$$\varepsilon_{net} = \varepsilon_{12} + \varepsilon_{34} = (r_{12} - r_{34})\, Q/\rho \tag{1.7}$$

[f]It is better to use atomic masses in the Q-value calculation because this will automatically account for the electrons or positrons emitted in β-decay. The difference between atomic and nuclear Q-values is given by the differences of the electron binding energies in the entrance and exit channels ($\mathrm{Q}_{atomic} = \mathrm{Q}_{nuclear} + \Delta \mathrm{B}_e$).

1.3.2. Non-resonant Reaction rates involving charged particles

When charged particles are involved in a nuclear reaction, one must take into account the Coulomb barrier, given by

$$V_C = \frac{Z_1 Z_2 e^2}{r} \approx \frac{Z_1 Z_2}{(R_1 + R_2)} 1.44 \text{ MeV fm} \tag{1.8}$$

Here e is the fundamental electric charge unit, $Z_{1,2}$ and $R_{1,2}$ are the nuclear charge and radii of the particles in the entrance channel, respectively. The nuclear radii can be approximated by $R \approx 1.2\ A^{1/3}$ fm. The Coulomb barriers for the ^{18}Ne(α,p)^{21}Na and ^{19}Ne(p,γ)^{20}Na reactions are approximately 5.7 and 3.4 MeV, respectively. Most stellar thermonuclear reactions occur at temperatures and energies that are far below the Coulomb barrier. Even at $T_9 = 1$, well into the thermonuclear runaway phase of an XRB (Figure 1.5, the Boltzmann factor is only $kT = 86$ keV. At energies well below the Coulomb barrier, the barrier penetration probability can be approximated by

$$P = \exp\left(-2\pi\eta\right) \tag{1.9}$$

Where η is the Sommerfeld parameter

$$\eta = \frac{Z_1 Z_2 e^2}{\hbar v} = \frac{Z_1 Z_2 e^2}{\hbar} \sqrt{\frac{2\mu}{E}} \tag{1.10}$$

The exponential behavior of the tunneling probability causes the cross section to decrease rapidly for energies below the Coulomb barrier. The cross section $\sigma(E)$ in Eqn (1.4) can be thought of as a geometrical area, which in quantum mechanical terms is governed by the deBroglie wavelength $\lambda\!\!\!^{-} = \frac{m_1+m_2}{m_2} \frac{\hbar}{\sqrt{2m_1 E_1}}$, where E_1 is the kinetic energy of particle 1

with mass m_1 incident on a target particle at rest with mass m_2. Combining the barrier penetration term with the geometrical cross section $\sigma(E) = \pi\lambda^2 \propto \frac{1}{E}$, we can write the energy dependent cross section for charged particles as

$$\sigma(E) = \frac{1}{E} S(E) \exp(-2\pi\eta) \tag{1.11}$$

All nuclear effects beyond phase space and penetrability are contained in the function $S(E)$, which is called the astrophysical S-factor and is defined by this equation. While not essential for the purposes of this thesis, the S-factor is worth noting because it appears often in the literature. $S(E)$ varies smoothly with energy for non-resonant reactions and is less sensitive to the laboratory incident beam energy than the cross section. Historically, therefore, the S-factor has been useful in extrapolating cross sections measured at energies above the Coulomb barrier, to astrophysical energies. Inserting Eqn (1.11) into Eqn (1.4) gives

$$\langle \sigma v \rangle = \sqrt{\frac{8}{\mu\pi}} (kT)^{-3/2} \int_0^\infty S(E) \exp\left[-\frac{E}{kT} - \frac{b}{\sqrt{E}}\right] dE \tag{1.12}$$

The quantity b is given by

$$b = \sqrt{2\mu}\, \pi\, e^2 Z_1 Z_2 / \hbar \tag{1.13}$$

The square of this quantity is called the Gamow energy, E_G. Neglecting any dependence of S on energy, the two exponential terms determine the energy dependence of Eqn (1.12). The first term in the exponential is due to Boltzmann distribution, which drops off rapidly with energy. The second term is the penetrability of the Coulomb barrier, which increases

rapidly with energy. The product of these two terms gives rise to a maximum value of the integrand at energy E_0 called the "Gamow peak". Obtaining the maximum (i.e. least negative value) of the exponent by setting its first derivative to zero gives

$$E_0 = \left(\frac{bkT}{2}\right)^{2/3} = 0.122 \left(Z_1^2 Z_2^2 \mu\right)^{1/3} T_9^{2/3}\, MeV \tag{1.14}$$

The exponential term in (1.12) can be approximated by a Gaussian function

$$\exp\left(-\frac{E}{kT} - \frac{b}{\sqrt{E}}\right) \approx \exp\left[-\left(\frac{E - E_0}{\Delta/2}\right)\right] \tag{1.15}$$

with a characteristic $1/e$ width determined by matching the second derivatives of both sides of Eqn (1.15).

$$\Delta = 4\left(\frac{E_0 kT}{3}\right)^{1/2} = 0.2368 \left(Z_1^2 Z_2^2 \mu\right)^{1/6} T_9^{5/6} MeV \tag{1.16}$$

This width defines the energy window in which most of the reactions take place and is called the Gamow window associated with the Gamow peak at E_0. Figure 1.7 shows the relative probabilities of the energy dependent terms of Eqn (1.12) and the calculated Gamow peak E_0 = 351 keV with full width of the Gamow window Δ = 284 keV for the ^{19}Ne(p,γ)^{20}Na reaction at T_9 = 0.5. The peak of the Maxwell-Boltzmann distribution kT = 43 keV is also shown.

1.3.3. Resonant reactions and the compound nucleus

Many astrophysical reactions of interest proceed through resonances in the compound nucleus. Compound nuclear reactions can be represented as two-step processes 1 + 2

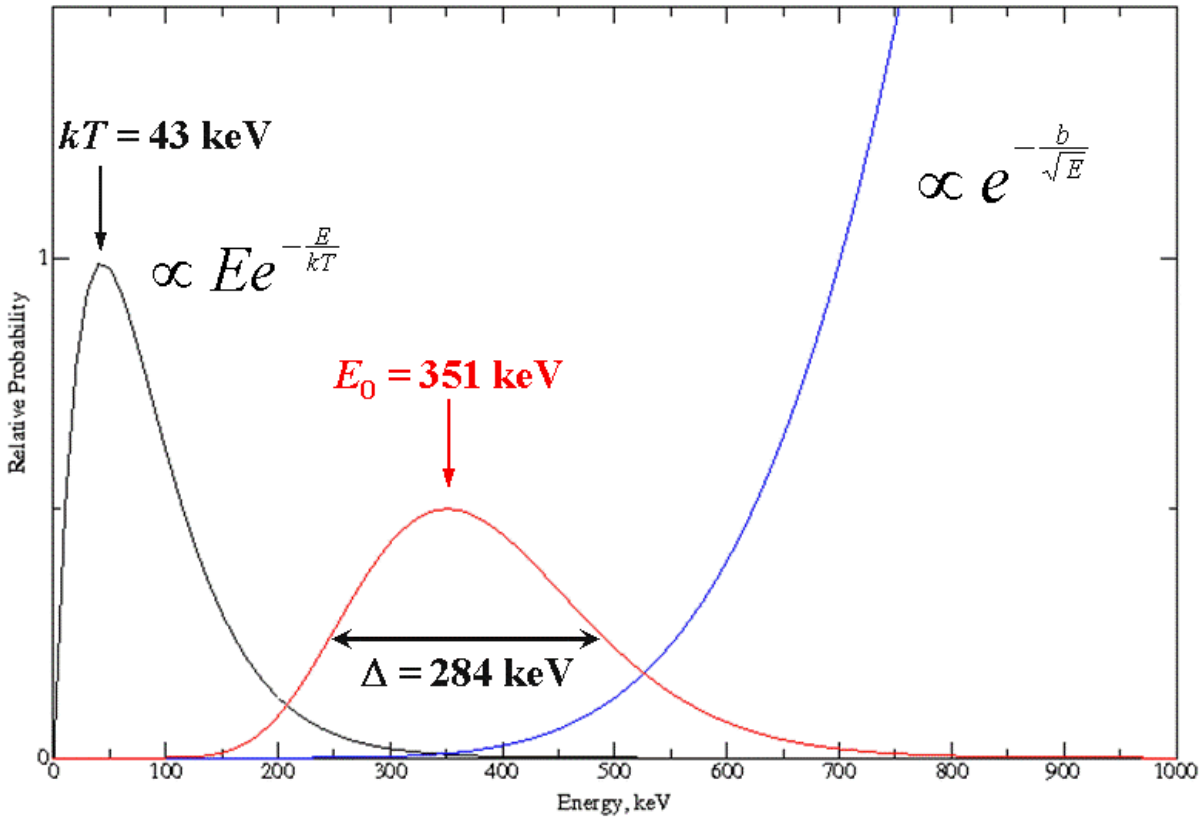

Figure 1.7. The relative probabilities of the energy dependent terms governing the reaction rate for non-resonant charged particles. The Boltzmann distribution (black), penetrability (blue) and the Gamow peak (red) are shown for ^{19}Ne + p at $T_9 = 0.5$.

$\rightarrow C_r \rightarrow 3 + 4$. A resonance in the compound nucleus, C_r, at energy E_r is first formed in the entrance channel. Once formed, the state can decay by γ-emission, or by particle emission to a different "daughter" nucleus or back to the same particles in the entrance channel. The subsequent decay is independent of the how the state was formed. The process is shown schematically in Figure 3.2 for the p(^{21}Na,α)^{18}Ne experiment. For an isolated, narrow resonance, in which particle 1 and particle 2 combine to form a state r

centered at energy E_r the cross section is given by the Breit-Wigner formula

$$\sigma(E) = \pi\lambda\!\!\!^{-2}\frac{2J_r+1}{(2J_1+1)(2J_2+1)}\frac{\Gamma_1\Gamma_3}{(E-E_r)^2+(\Gamma/2)^2} \tag{1.17}$$

where J_i represents spin of particle i and Γ_i the partial width for emitting particle i. The total width of the resonance is given by the sum of the partial widths

$$\Gamma = \sum\nolimits_i \Gamma_i \tag{1.18}$$

The Breit-Wigner formula is strictly valid only for isolated resonances, in which the separation of energy levels is larger than the widths, and narrow resonances, in which the total width is much smaller than the resonance energy. Integration of the Breit-Wigner formula leads to

$$\int_0^\infty \sigma_{BW}(E)\,dE \;=\; \pi\lambda\!\!\!^{-2}_r\omega\Gamma_1\Gamma_3\int_0^\infty \frac{1}{(E-E_r)^2+(\Gamma/2)^2}dE \;=\; 2\pi^2\lambda\!\!\!^{-2}_r\omega\frac{\Gamma_1\Gamma_3}{\Gamma} \tag{1.19}$$

The product of the statistical spin factor, ω, and the ratio of the widths, $\gamma = \Gamma_1\Gamma_3/\Gamma$, is called the "resonance strength":

$$\omega\gamma = \frac{2J_r+1}{(2J_1+1)(2J_2+1)}\frac{\Gamma_1\Gamma_3}{\Gamma} = \omega\frac{\Gamma_1\Gamma_3}{\Gamma} \tag{1.20}$$

The integrated cross section for an isolated, narrow resonance can be calculated from the resonance strength, and combining these into the expression for the reaction rate per particle pair (Eqn 1.4), we obtain

$$\langle\sigma \mathrm{v}\rangle = \left(\frac{2\pi}{\mu kT}\right)^{3/2}\hbar^2(\omega\gamma)_r\exp\left(-\frac{E_r}{kT}\right) \tag{1.21}$$

For the narrow resonance case, the stellar reaction rate can be calculated from the resonance parameters E_r and $\omega\gamma$ that can be measured in the laboratory. If the reaction of interest has several narrow resonances within the Gamow window, the contribution to the reaction rate from each resonance can be summed:

$$\langle \sigma \mathrm{v} \rangle = \left(\frac{2\pi}{\mu kT} \right)^{3/2} \hbar^2 \sum\nolimits_i (\omega\gamma)_i \exp\left(-\frac{E_i}{kT} \right) \tag{1.22}$$

1.4. Summary

In order to understand the energy generation mechanisms that power the observed astrophysical phenomena discussed above and to test the theoretical models for thermonuclear burning at these extreme conditions, the network calculations need to be improved. Experiments provide the data (i.e. – resonance strengths, cross sections, etc.) necessary to better constrain the network calculations. The focus of this work is to measure key reaction parameters for the three CNO-cycle breakout reactions that lead to the *rp*-process.

CHAPTER 2

Radioactive Ion Beam production and detector setups at the ATLAS facility

2.1. In-flight Production of Radioactive Ion Beams (RIBs)

The three possible reaction pathways breaking out of the CNO cycles (identified in Section 1.2.3) have been studied using the Argonne Tandem Linear Accelerator System (ATLAS). As is the case for many nuclear reactions of astrophysical interest, the CNO cycle breakout reactions involve radioactive nuclei with half-lives ranging from a few seconds to a few hours. Radioactive targets would often require handling prohibitively large amounts of radioactivity and in any event are limited to nuclei with half-lives of a few hours or longer. Therefore, the development and use of radioactive ion beams (RIBs) is essential to studying these reactions. Three techniques for producing RIBs of short-lived nuclei have been developed around the world – isotope separator on-line (ISOL) [**21**], projectile fragmentation [**22, 23, 24**], and in-flight production [**25, 26**]. The ISOL method uses radioactive isotopes that have been produced by neutrons from a reactor or by the beam of a driver accelerator impingent upon a thick production target. A second device is used to accelerate the isotopes of interest after they have diffused out of the production target, making it difficult to produce beams of shorter-lived (≤ 1 second) isotopes. The projectile fragmentation method uses heavy-ion beams at around 50 – 100 MeV per nucleon impingent upon a thin primary target. The beam fragments

are separated electromagnetically and delivered to the experimental area with energies comparable to that of the incident primary beam. The in-flight technique is similar to projectile fragmentation, using lower mass beams, A $\leq$ 40, of lower energies impingent upon a thin primary production target to produce secondary beams of radioactive isotopes with energies of a few MeV/u. The in-flight technique is therefore better suited for studying astrophysical reactions, which typically take place with energies $\leq$ 2 MeV/u. Each of these techniques has its advantages and drawbacks, which have been summarized by Smith and Rehm [**27**]. The nuclear astrophysics group at Argonne has developed an in-flight production facility [**28, 5**], which has been used in the present work. In contrast to projectile fragmentation, the in-flight method can utilize lighter mass primary beams to produce secondary beams at energies that can be changed by varying the incident primary beam energy. Single nucleon transfer reactions, such as (d,n) and (d,p) or the charge exchange reaction (p,n), have primarily been used at ATLAS to produce isotopes one or two nucleons beyond stability with masses ranging from A = 6 – 37[a]. These reactions are most effective because they have relatively large cross-sections and their angular distributions are forward peaked. With a heavy beam incident on a light target, or "inverse kinematics" the center-mass angles are compressed by a factor of 10 or more when transformed to the laboratory frame improving the transmitted intensity of the secondary beam [**29**]. Because the beams are produced by nuclear reactions, their intensities are generally 4 to 8 orders of magnitude weaker than the primary beam. Thicker targets degrade the quality of the beam, increasing both the energy and angular spread. The challenge is to maximize the intensity of the secondary beam while minimizing the energy

[a]http://www.phy.anl.gov/atlas/facility/radioactive_beams.html

spread and the size of the beam spot. For details of the in-flight facility at ATLAS, including the beam transport system and a summary of the beam tuning procedure, see Harss et al. [**5**]. The following discussion briefly describes the production of the radioactive beams used in this work – a ^{21}Na beam to study the ^{18}Ne(α,p)^{21}Na reaction via the time inverse reaction p(^{21}Na,α)^{18}Ne (Chapter 3), and a ^{19}Ne beam used to measure the ^{3}He(^{19}Ne,d)^{20}Na angular distribution (Chapter 4).

A series of 3.75-cm long gas production cells have been constructed [**28, 5**] and installed in the ATLAS beam line 15 meters upstream of the experimental target area. The gas cells are filled with isotopes of hydrogen or helium and cooled with liquid nitrogen. For producing the ^{21}Na ($\tau_{1/2}$ = 22.48 s) beam via the d(^{20}Ne,n)^{21}Na reaction, the production gas cell was filled with D_2 at a pressure of 700 mbar and maintained at 83 K, for an overall thickness of 1.53 mg cm^{-2}. A primary ^{20}Ne beam was accelerated to 135 MeV and focused onto the gas cell. Because the ^{20}Ne ions in the primary beam are heavier than the deuterium nuclei, energy and momentum conservation require that the reaction products be forward-focused to within a cone with small opening angles, $< 4^\circ$ in this case. The emerging ^{21}Na beam was refocused and delivered to a secondary target area through an ion-optical transport system consisting of a refocusing superconducting solenoid, a debunching resonator and a bending magnet, as shown in Figure 2.1.

The refocusing solenoid is used to capture the reaction products and focus them through a 22° bending magnet, which selects and steers the secondary beam to the experimental target area. A superconducting debunching resonator located between the production cell and the bending magnet is used to reduce the energy spread of the secondary beam by matching the RF phase of the resonator with the correlated energy and

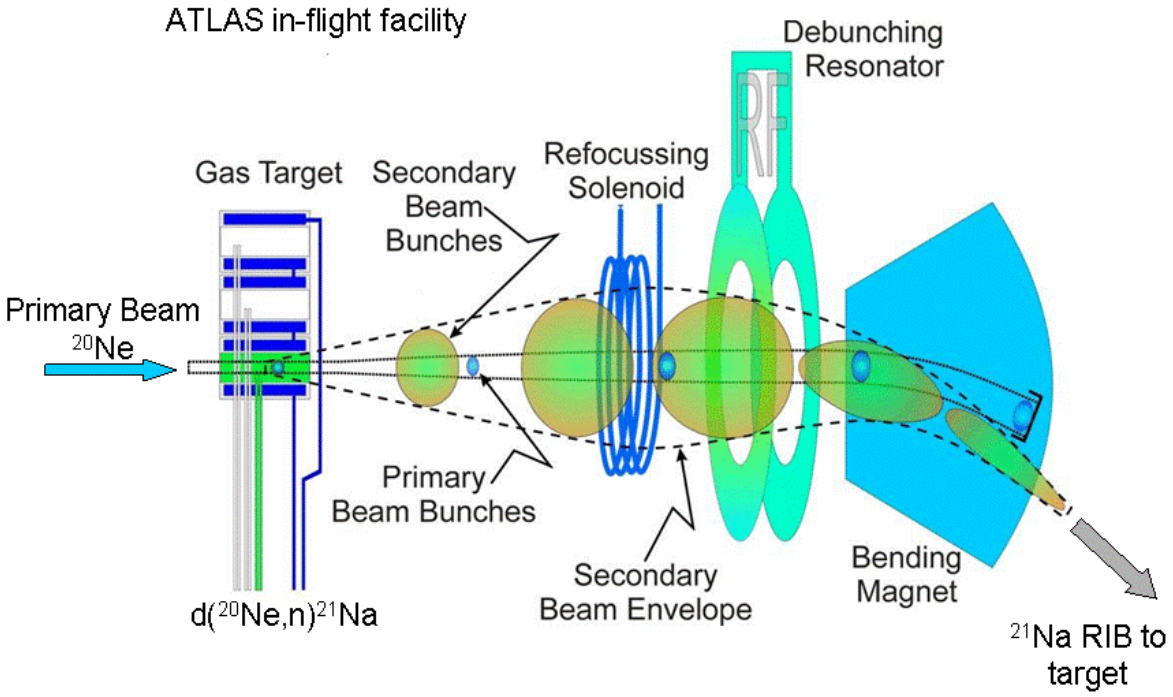

Figure 2.1. The ATLAS in-flight beam production facility shown for the production of a ^{21}Na beam via the d(^{20}Ne,n)^{21}Na reaction (Adapted from Ref [**5**]).

time of the secondary beam. The time correlation is further enhanced by using another superconducting "bunching" resonator (not shown) 10 meters upstream of the production target, providing a time focus of the primary beam at the gas cell. By tuning the resonators, the energy spread of the emergent secondary beam was reduced by a factor of ≈ 3 and the beam current was improved by a factor of ≈ 2 [**5**]. The bending magnet separates the secondary beam from the primary beam according to their magnetic rigidity (see next section), resulting in suppression of the primary beam by a factor of $\approx 10^{-6}$ [**30**].

The gas cells are enclosed at either end by 1.9 mg cm^{-2} Havar® foils. The secondary beams are produced with energies determined by the reaction kinematics for the energy of the primary beam at the point of the reaction. The secondary beams must then traverse the remainder of the gas cell and the exit foil before being directed to the experimental target. Energy loss calculations were performed using the SRIM 2006 code [**31**] to determine the energy spread and straggling of the primary and secondary beams. For the first p(^{21}Na,α)^{18}Ne reaction study the incident ^{20}Ne energy was 135 MeV and the calculated energy loss in the Havar entrance foil was 6.5 MeV. The primary ^{20}Ne beam entered the ^{3}He gas volume with 128.5 MeV and lost 11.9 MeV through the length of the gas cell. The d(^{20}Ne,n)^{20}Na reaction therefore took place with energies ranging from 128.5 – 116.6 MeV. For the d(^{20}Ne,n)^{21}Na reaction at the beginning of the gas cell the secondary ^{21}Na particles emitted in the forward direction had energies of 127.6 MeV. These ^{21}Na ions lost 13.9 MeV through the gas and emerged with 113.7 MeV. The ^{21}Na ions produced at the end of the gas cell had energies of 115.7 MeV. The energy spread of the secondary beam due to the thickness of the gas cell was therefore 2 MeV. For comparison, the calculated energy straggling in both the primary and the secondary beam was 120 keV.

The bending magnet, solenoid, and resonators were adjusted to select a narrow range of energy determined by the momentum acceptance of the magnet, $\Delta p/p$. The details of beam tuning are beyond the scope of this thesis. To summarize, the primary beam was first tuned without the gas cell in place, and then re-tuned through the gas cell. The bending magnet settings were then scaled for the secondary beam by the ratio $\sqrt{mE}/q$, where m is the mass, E is the kinetic energy and q is the atomic charge state of the ion. The energies of both the primary and the secondary beams were measured in the

spectrograph (discussed in the following section), which was calibrated using an alpha source. The bending magnet, refocusing solenoid and debunching resonator were re-tuned to minimize the on-target ratio of the primary beam to the secondary beam and to minimize the energy spread while maximizing the intensity of the secondary beam. Adjustable slits located between the bending magnet and the experimental target area provide an additional way to control the energy spread and purity of the beam by limiting size of the beam spot and by blocking portions of the low-energy tails of the scattered beams.

The magnetic spectrograph (described below) was positioned at zero degrees and used to measure the secondary beam energy at the beginning, the end and intermittently throughout the experiment. At the start of the p(^{21}Na,α)^{18}Ne experiment, the energy measured in the spectrograph was 113.7 MeV for the $^{20}Ne^{10+}$ and 110.3 MeV for $^{21}Na^{11+}$, with a full-width at half-maximum of 2 MeV, in good agreement with the calculated energy spread. During the production runs a 100 μg cm^{-2} gold foil was placed in the spectrograph scattering chamber and the scattered ^{21}Na beam counted in the spectrograph. The beam current was (2.5 – 5) $\times$ 10^{-5} particle nanoamps (pnA) or (1.5 – 3) $\times$ 10^{5} ^{21}Na s^{-1} on target. The beam intensity was improved by a factor of about 2 in later runs by using the p(^{21}Ne,n)^{21}Na production reaction. For this run, the gas cell was filled to 1250 mbar for a thickness of 1.35 mg cm^{-2}. The improvement in the transmitted primary to secondary beam ratio was primarily due to the smaller opening angle of the outgoing ^{21}Na ions, $\theta_{max} \leq 1^{\circ}$, rather than $\theta_{max} \leq 4^{\circ}$ for the d(^{20}Ne,n)^{21}Na reaction. In the later runs, a germanium detector was placed near the entrance of the spectrograph to monitor the β-decay of the stopped ^{21}Na by counting the 511 keV γ-rays from e^+e^- annihilation. The

beam current was also monitored by using the annular Bragg curve detector (described below) to measure the Rutherford scattering of the beam off the carbon in the CH_2 target.

The ^{19}Ne ($\tau_{1/2}$ = 17.22 s) beam for the ^{3}He(^{19}Ne,d)^{20}Na* reaction was produced via the p(^{19}F,n)^{19}Ne reaction using a 126 MeV ^{19}F primary beam using the same technique as for the ^{21}Na beam described above. The gas cell was filled with 1400 mbar of H_2 gas for a thickness of 1.66 mg cm^{-2}. The ^{19}Ne beam intensity was (0.3 – 3.5) $\times$ 10^{5} s^{-1} on target and the ratio of primary to secondary beam was 2:1. The goal of this experiment was to measure the shape of the angular distribution of the outgoing deuterons rather than the cross sections. Therefore, precise knowledge of the beam energy and intensity was less crucial and the spectrograph was not used to measure the beam energy. Instead, two silicon barrier detectors were used in tuning the beam – one before and one after the experimental target. The details of the ^{3}He(^{19}Ne,d)^{20}Na experiment are given in Section 4.3.2.

2.2. Targets

For the p(^{21}Na,α)^{18}Ne experiment a 380 μg cm^{-2} polypropylene $(CH_2)_n$ target was used. The other three experiments discussed here used a 10 mm diameter 1 mm long cylindrical gas cell. The cell was filled with ^{3}He or ^{4}He, cooled with liquid nitrogen to about 80 K, and maintained at 700 – 750 mbar using a gas handling system. The effective target length varied between 1.5 and 3.5 mm depending on the gas pressure and the thickness and type of foils used. The details for each experiment are given in Chapters 3 and 4.

2.3. Detector setups and particle identification

Because the reactions studied in this work were done in inverse kinematics, unwanted isotopes produced by reactions in the targets and the pressure foils are also forward focused creating background. Beams produced via the in-flight technique contain contamination due to leakage of the primary beam through the transport system. Small-angle scattering in the foils and the gas cell produce a low-energy tail in the primary beam. Those particles that have the magnetic rigidity of the secondary beam are transported to the experimental area. For the d(^{20}Ne,n)^{21}Na production reaction the ratio of the primary beam to the secondary beam delivered to the target area was about 2:1. The primary beam that leaks through the transport system also induces reactions in the target producing a background of products with masses and energies similar to the particles being studied. Because of the large number of unwanted reaction products the kinematic coincidence technique [**32**] was used to identify the reaction of interest. The light particles were detected in position-sensitive, double-sided silicon strip detectors (DSSDs), providing angle and energy information. The heavy recoils were detected in a system that consisted of a parallel plate avalanche counter (PPAC) followed by an ionization chamber (IC). A homogeneous electric field is maintained between the entrance foil of the ionization chamber, which serves as the cathode, and the anode at the back of the chamber, which is shielded by a fine wire mesh Frisch grid. As the ionizing particle loses energy in the gas it produces a track of electrons and ions. The ionization rate increases as the particle slows down and reaches a maximum, the Bragg peak, just before it loses all its energy. The electrons produced by the ionization drift towards the anode at the back of the chamber where the charge is collected. The drift velocity is constant in the uniform electric field

and the drift time is long compared to the time it takes the particle to lose all its energy. Therefore, the time-dependence of the anode signal gives dE/dx. The resulting pulse is split into two output signals. One signal is processed using a shaping time longer than the total charge collection time of a few μs and measures the total ionization charge, which is proportional to the energy deposited in the gas (*E signal*). The second signal is processed using a shorter shaping time ≈ 0.5 μs and measures the height of the Bragg peak, which is proportional to the nuclear charge (*Z signal*) of the ionizing particle. Details of this technique, known as Bragg-curve spectroscopy, have been given by Schiessl et al. [**33**]. The range signal (*RANGE*) of the particle measures the time it takes the ionization electrons to drift through the chamber. The parallel-plate avalanche counter (PPAC) mounted at the front of the chamber provide the start signal for a time-to-analog converter (TAC) and the IC anode provide the stop signal. Because the drift velocity is constant in the gas, the drift time is inversely proportional to the distance traveled by the ionizing particle in the chamber. The range (R) of the particle is given by

$$R = \int_0^E \left(-\frac{dE}{dx}\right)^{-1} dE \propto -\frac{E^2}{MZ^2} \tag{2.1}$$

Therefore, a two-dimensional histogram of *RANGE* vs. E^2 produces bands with different slopes corresponding to different Z (and M) values. While the height of the Bragg peak is independent of the initial particle energy there was some recombination as the electrons drifted towards the Frisch grid, and so the Z signal was higher for higher energy particles (i.e., those that penetrated further into the IC). Therefore, a contour plot of *Z signal* vs. *E signal* is needed to separate particles of different Z. (Note: This defect

has since been corrected.) The timing signals from the DSSD and the PPAC together provide a time spectrum that is used to identify coincidences. An additional time signal is provided by the RF frequency of ATLAS, which in combination with the PPAC timing signal provides time of flight (TOF) information.

2.3.1. "Ludwig's Castle"

For the p(^{21}Na,α)^{18}Ne and the ^{3}He(^{19}Ne,d)^{20}Na experiments, an array of annular DSSDs dubbed Ludwig[b], and an annular PPAC – ion chamber system was used. The annular DSSDs were 500 μm thick with an active area covering radii from 24 to 48 mm, with both sides providing independent energy and timing signals. One side was segmented into 16 1.5-mm wide rings providing a measure of the light particle angle, θ_{lab}. For the ^{3}He(^{19}Ne,d)^{20}Na experiment the angular resolution was $\approx 0.9^{\circ}$ near the angle range of interest, $\theta_{lab} \approx 55^{\circ}$. For the p(^{21}Na,$\alpha$)^{18}Ne experiment the angular resolution for the α-particles was $\approx 0.3^{\circ}$. The other side of the annular DSSD was divided into16 wedges. For this work, the azimuthal angle was not required. The energy signals from the two sides of the DSSD were compared and used as a gating condition as described in Section 4.3.3. The annular ionization chamber and PPAC have inner diameters of 15 mm to allow the beam to pass through the center. The effective radii of the entrance windows extended from 9.5 to 40 mm and covered recoil angles $1.4 \leq \theta_{lab} \leq 6^{\circ}$. Aluminized Mylar foils are used to contain the gas and to serve as electrodes. The PPAC foils were 2.5 μm thick with the entrance foil kept at an operating voltage of 600 V for the p(^{21}Na,α)^{18}Ne experiment and the exit foil was kept at ground. The 10 mm long PPAC was maintained at 3 torr of

[b]The "Large Universal Detector with Immense Granularity" was named in honor of two Bavarian kings by a student from Munich. .

isobutane (C_4H_{10}). A 6.25 μm thick entrance foil serves as the IC cathode. A wire mesh grid is mounted at the front to minimize the stretching of the foil under pressure. The 9 cm long IC was maintained at 330 torr of Freon (CF_4). The active length between the cathode and the Frisch grid is 6.3 cm. The grid was operated at 700 V and the anode, 13 mm behind the Frisch grid, was operated at 2360 V. A gas handling system was used to maintain a constant pressure and flow rate. The detectors were mounted in an annular vacuum chamber, "Ludwig's Castle," that was placed along the ATLAS beam line in front of the Enge split-pole spectrograph. The setup is shown in Figure 2.2.

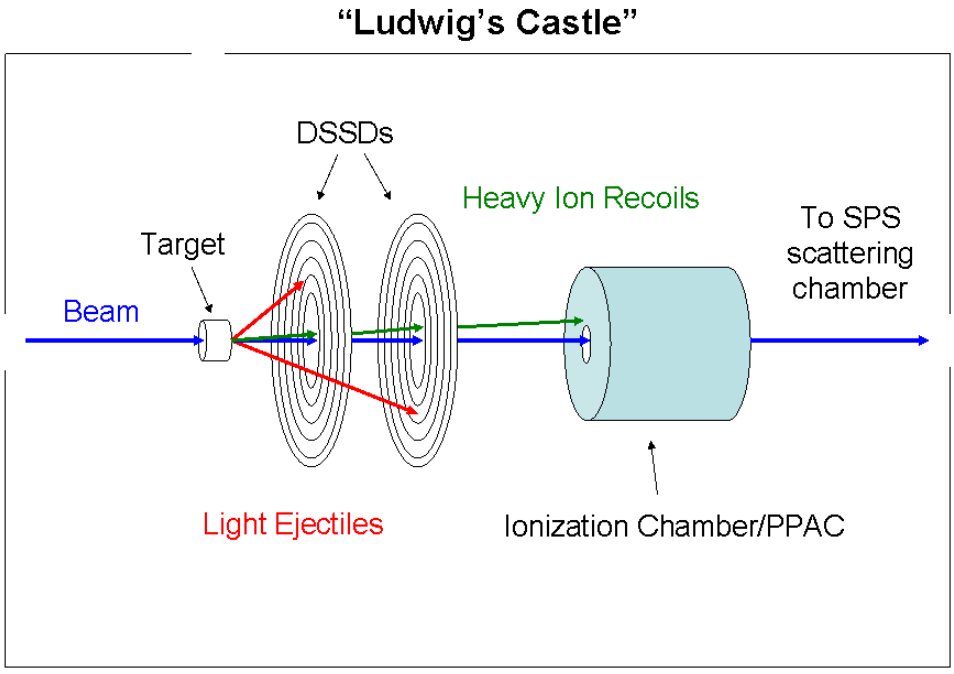

Figure 2.2. Schematic of the Ludwig detector setup. This configuration was used to measure the alphas from the p(^{21}Na,α)^{18}Ne reaction, and to measure the deuterons from the ^{3}He(^{19}Ne,d)^{20}Na reaction.

2.3.2. The scattering chamber and the Enge split-pole spectrograph

To measure the branching ratios, $\Gamma_\alpha/\Gamma_\gamma$ for the 4.033 MeV state in ^{19}Ne (described in Chapter 3) and Γ_p/Γ_γ for the 2.645 MeV state in ^{20}Na (Chapter 4), absolute cross sections were not required. For these two experiments, excited states above the particle threshold were populated via a transfer or charge exchange reaction. The excited states were tagged by the energy and angle of the light particle. The recoiling heavy nuclei then break up by particle emission or γ-decay. The light particles were measured in a 500 μm thick square DSSD, located on one side of the beam axis. The active area of the DSSD was divided into 30 1-mm horizontal strips and 31 1-mm vertical strips. Because the ^{19}Ne ions produced in these reactions have the same Z as the primary ^{20}Ne beam and differ by only one mass unit, clean separation of the recoil nuclei by mass was crucial. Therefore, the Enge split-pole spectrograph was used to detect the recoils. This setup is shown schematically in Figure 2.3. The geometry of the DSSD and the spectrograph was determined by the reaction kinematics for the state of interest.

A magnetic spectrograph separates ions by their magnetic rigidity, $B\rho = \frac{p}{q} \approx \frac{\sqrt{2mE}}{q}$, where B is the magnetic field in the spectrograph, ρ the radius of curvature, q the atomic charge state, and p the momentum[c] of the ion. Particles with different magnetic rigidity are focused at different positions along the focal plane. A position-sensitive PPAC measures the position along the focal plane. A two-dimensional histogram of E vs. focal plane position separates ions by q^2/m. The PPAC, together with a gas-filled ionization chamber mounted behind the focal plane, measures E, R, and Z of the recoils, as described above.

[c]The non-relativistic approximation is valid. For recoil nuclei with A = 20 at 100 MeV, $\beta = v/c \approx 0.1$.

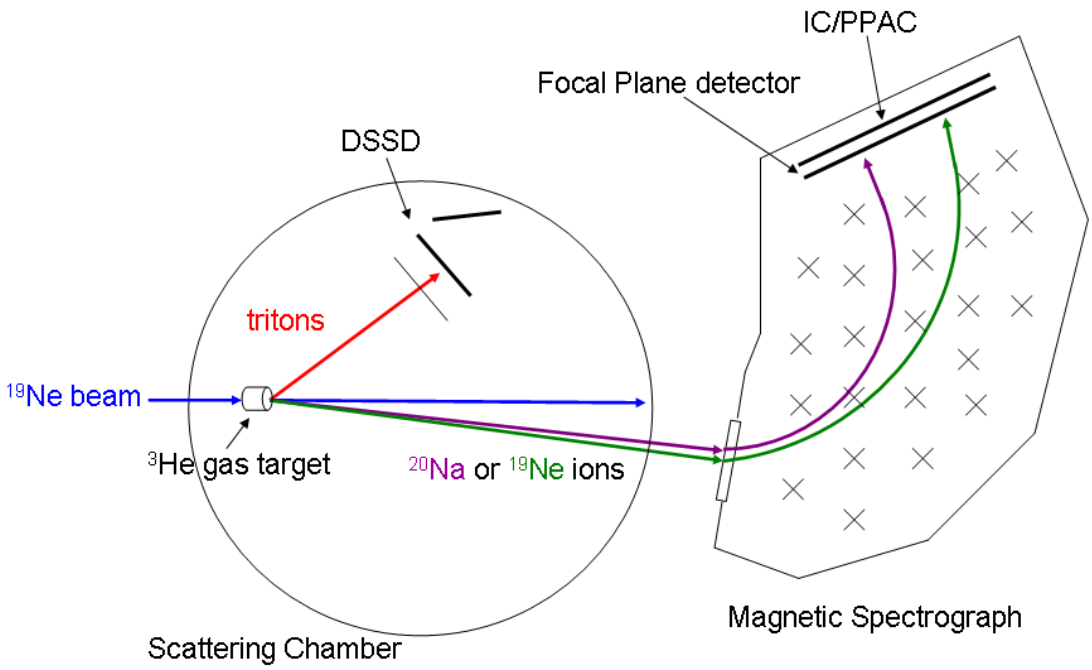

Figure 2.3. Schematic of the detector setup used to measure the branching ratio $\Gamma_\alpha/\Gamma_\gamma$ for the ^{3}He(^{20}Ne,α)^{19}Ne*, and Γ_p/Γ_γ for the ^{3}He(^{20}Ne,t)^{20}Na* experiment.

A block diagram of the electronics used for the branching ratio experiments is given in Figure 2.4. The fast timing signal from the PPAC anode with a rise time of 2 – 3 ns was fed into a fast pre-amplifier (FP) and then further amplified by a fast amplifier (FA) The amplified signal was then fed into a constant fraction discriminator (CFD, ESN CF4000). This signal served as a start signal for four different time measurements – a common start for the focal plane position *POSPP*, the range signal (*RANGE*), the time of flight (*TOF*) and the coincidence time (*TSI*). The position-sensitive PPAC (480 wires spaced 1.25 mm

apart) at the spectrograph focal plane was divided into two sides, high and low energy, providing four signals from the multi-wire plane – high energy position inside/outside (*HEPI*/*HEPO*), and low energy position inside/outside (*LEPI*/*LEPO*). Each of these signals is fed into an inverting fast amplifier (EG&G ESN FTA810) followed by a CFD (Phillips 715). These four signals were passed through a delay box and served as the stop signals for a time-to-digital converter (TDC, Lecroy 2228A) of ≈ 500 ns range. The PPAC position was determined by analyzing the time difference between these output signals and recorded as a pseudo-event parameter[d] (*POSPP*). The anode signal of the IC/BCD was fed into a Canberra 2010 low-noise pre-amplifier (PA) and split into two signals that were fed into two Tennelec amplifiers (TC 244 and TC 245) with shaping times of 3 μs for the energy signal E, and 0.5 μs for the nuclear charge signal Z. One output of TC 244 was fed into a timing single channel analyzer (Ortec 455, TSCA) and provided the stop signal for a time-to-pulse height converter (Ortec 467 TPHC/SCA), giving the particles range as described above. The time of the flight (*TOF*) through the spectrograph was measured by a TAC (Tennelec TC 862) with a 100 ns range. The stop signal for the *TOF* TAC was provided by the RF signal from the ATLAS debuncher unit, which was fed through a discriminator (Lecroy 623B) and a delay unit (TC 412A). The coincidence time was measured between the spectrograph PPAC and the DSSD with a TAC (TC 862). The E, Z, *RANGE*, *TOF*, and *TSI* signals were digitized by an analog-to-digital converter (ADC, Phillips AD 811). Each of the 64 channels of the DSSD – 32 channels per side with two 16-channel sections each (EF1, EF2, EB1 and EB2 for the front and back respectively) – were fed into their own pre-amplifier (PA) and then into four 16-channel

[d]A pseudo-event (PEV) parameter is an arithmetic combination of two or more real event (EV) parameters.

spectroscopic amplifiers (CAEN SPEC AMP). For each of these the fast output signal of the amplifier was fed into a CFD (LEC 3420), delayed, and used as the stop signal for TSI. The slow output signals from the DSSD amplifier were digitized by four 16-channel Phillips ADCs (ADC 7164H), providing the energy signals from the front (EF) and back (EB) of the DSSD.

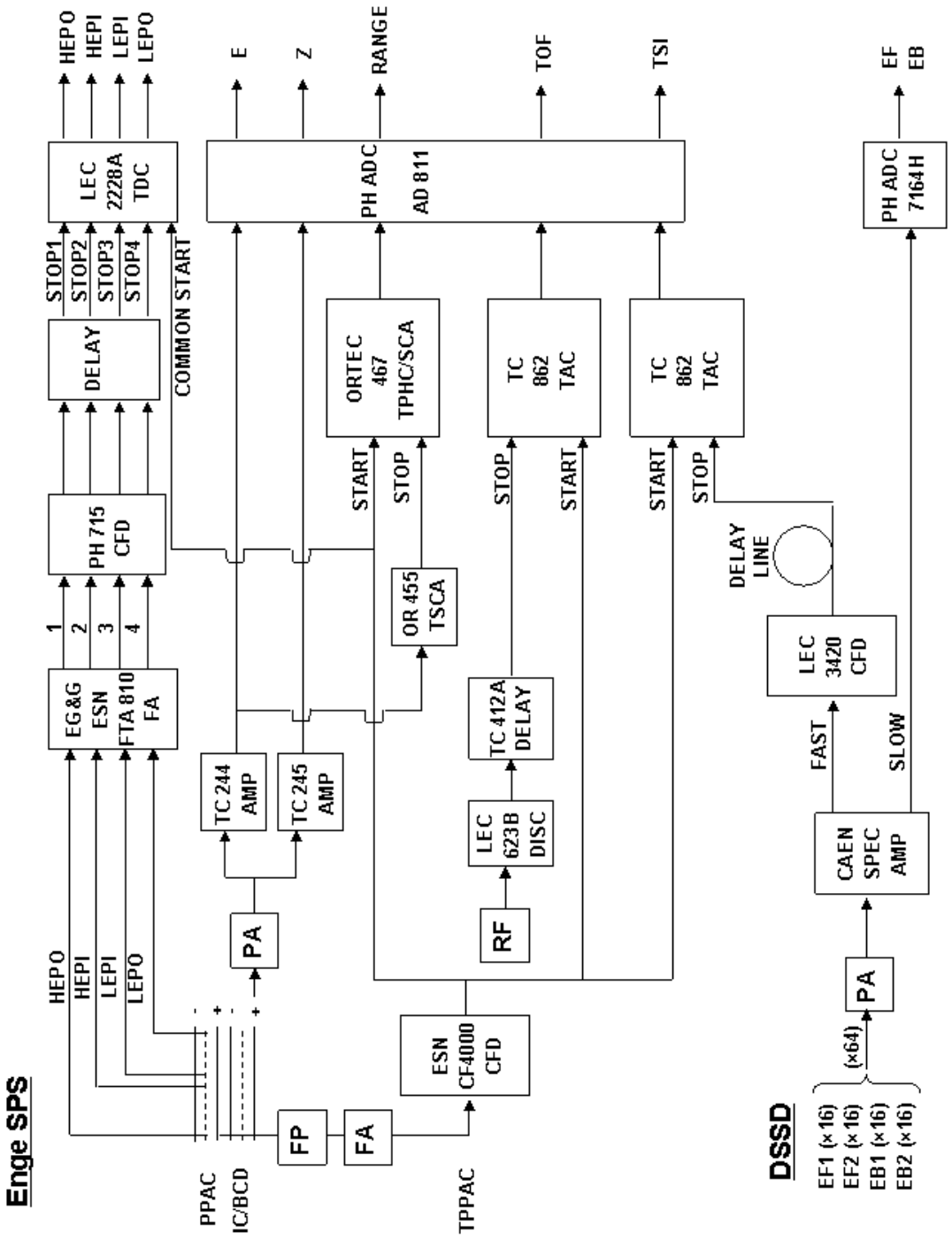

Figure 2.4. Block diagram of the electronics used in the ^{3}He(^{20}Ne,t)^{20}Na experiment.

CHAPTER 3

Earlier work

3.1. The ^{18}F(p,γ)^{19}Ne and ^{18}F(p,α)^{15}O reactions

The first reaction pathway (a) identified in Section 1.2.3 as a possible breakout path from the CNO cycle is ^{18}F(p,γ)^{19}Ne(p,γ)^{20}Na. The first reaction in this chain was studied using the ATLAS facility before the author's participation [**34, 35, 36**]. A brief summary is provided for context. The ^{18}F(p,γ)^{19}Ne reaction competes with the ^{18}F(p,α)^{15}O reaction during the HCNO-cycles, both proceeding mainly via resonant states in the compound nucleus ^{19}Ne. The branching ratio to the two products, ^{15}O and ^{19}Ne, determines to what degree breakout proceeds to the *rp*-process through ^{18}F(p,γ)^{19}Ne, or whether the ^{18}F is cycled back into CNO-material via the (p,α) reaction.

From the results of these earlier experiments it was determined that the ^{18}F(p,α)^{15}O reaction is stronger than the corresponding ^{18}F(p,γ)^{19}Ne reaction by at least 3 orders of magnitude. Thus, ^{18}F gets mainly recycled into CNO material rather than breaking out into the *rp*-process. The upper limit determined for the ^{18}F(p,γ)^{19}Ne reaction rate was a factor of three to four smaller than the previously estimated values [**37, 38, 3**]. This upper limit implies that the production of ^{19}Ne in the temperature range $T_9 \geq 0.5$ through this reaction channel is negligible.

3.2. Measuring the ^{18}Ne(α,p)^{21}Na reaction via the time inverse reaction p(^{21}Na,α)^{18}Ne

The next possible pathway (b) breaking out of the CNO cycle that has been identified is the ^{18}Ne(α,p)^{21}Na reaction (Section 1.2.3). Two measurements of this reaction have been reported from Louvain-la-Neuve in Belgium using a radioactive ^{18}Ne beam and an extended ^{4}He gas target [**7, 6**]. However, comparison of these two measurements reveals inconsistencies. The reaction proceeds through broad, overlapping states in ^{22}Mg. The resonance parameters were extracted from the efficiency corrected excitation functions of protons feeding the various states in the residual nucleus. E_R and Γ were determined from the centroid and width of a Lorentzian fit to the yield curve based on the assumed decay channel. The resonance strengths $\omega\gamma$ were then determined by inserting the fitted resonance parameters into the Breit-Wigner formula. The extracted resonance strengths were used to calculate the total stellar reaction rate. Cross sections were not reported. We have reconstructed the yield curves using the resonance parameters reported in references [**7**] and [**6**] and find that the two sets of cross sections differ by a factor of about 4. This discrepancy, along with the results of the present work (discussed below), is shown in Figure 3.4.

From the resonance strengths and spins reported in [**7**] and [**6**], lower limits for the α-widths Γ_α were extracted. An estimate of the maximum width for decay is the Wigner limit which takes the time that it takes a particle to cross the nucleus and converts it into a width using the uncertainty principle $\Delta E \Delta t = \hbar$. If there is a barrier that has to be penetrated, that has to be factored into the calculation of how long it should take

a particle to escape the nucleus. For a charged particle with angular momentum ℓ, the partial width can be expressed as

$$\Gamma_\ell = \left(\frac{2\hbar}{R_n}\right)\sqrt{\frac{2E}{\mu}}P_\ell\left(E, R_n\right)\theta_\ell^2 \tag{3.1}$$

where R_n is the nuclear radius, E is the center mass energy, μ is the reduced mass, and $P_\ell(E, R_n)$ is the penetration factor for tunneling through the Coulomb and the centrifugal barrier for a given orbital angular momentum ℓ. The quantity θ_ℓ^2 is a dimensionless number called the "reduced width"[a] of the state and contains information about the nuclear structure. In the case of α-decay, this factor represents the probability that an α-particle is preformed in the compound nucleus. The Wigner limit is obtained by setting $\theta_\ell^2 = 1$. The parameters reported in [**6**], lead to alpha spectroscopic factors close to unity for all the high-lying 2^+ states, much larger than the expected values of a few percent.

The measurements in [**7, 6**] covered an excitation energy range in the compound nucleus ^{22}Mg from 10 – 11 MeV. Although the Gamow peak does not strictly apply to resonance reactions, it can be used to predict the most effective stellar energy range for charged particle reactions to occur for a given temperature, and hence, which resonances would most likely dominate the astrophysical reaction rate. The Gamow energy window (Eqns 1.14 and 1.16) for the ^{18}Ne(α,p)^{21}Na reaction and the corresponding excitation energies in the compound nucleus ^{22}Mg are shown in Figure 3.1. The temperature range relevant for breaking out of the HCNO cycles in X-ray bursts is $T_9 \approx 0.3 - 1$ (see Figure 1.5). For the ^{18}Ne + α system, the corresponding Gamow peak leads to excitation

[a]The term "reduced width" is also called the "spectroscopic factor". The two terms have been used interchangeably and one must take care to note whether the authors are reporting θ_ℓ^2, C^2S, or S.

energies in the compound nucleus ^{22}Mg of ≈ 8.5 – 10 MeV. It is therefore desirable to measure this reaction at lower energies. The excitation energies between ≈ 9.4 and 10 MeV in ^{22}Mg studied in this work correspond to a temperatures T_9 ≈ 1 – 2 indicated by the heavy vertical bars.

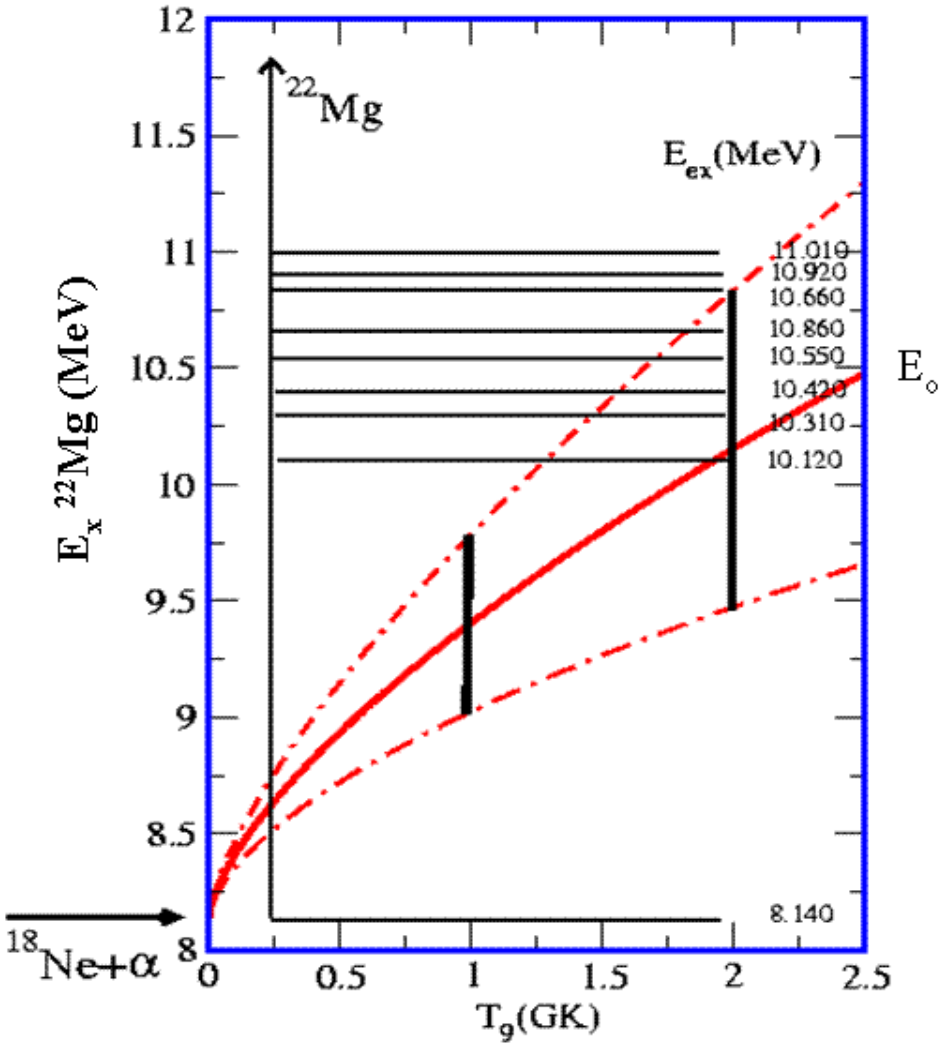

Figure 3.1. Energy levels in the compound nucleus ^{22}Mg reported by Ref [**6**]. The Gamow peak E_O and width Δ are shown in red for temperatures of astrophysical interest. The vertical bars indicate the temperature range studied in this work. The ^{18}Ne + α threshold is indicated on the left.

In order to resolve the discrepancies between the two reported measurements and to extend the measurements to lower energies, we have measured the time inverse reaction p(^{21}Na,α)^{18}Ne. An advantage of measuring the time inverse reaction is that the incident beam energy required to populate these states in the compound nucleus is higher than for measuring the forward reaction. The 10.66 MeV state in ^{22}Mg is 2.52 MeV above the ^{18}Ne + α threshold at 8.14 MeV. However, this same state is 5.16 MeV above the ^{21}Na + p threshold at 5.50 MeV. The Louvain-la-Neuve experiments required a bombarding energy of 30 MeV for the ^{18}Ne beam. Populating the same state via the time inverse reaction requires a 110 MeV ^{21}Na beam. Higher incident beam energies lead to better kinematic focusing of the reaction products increasing the detection efficiency. A partial energy level scheme of ^{22}Mg is shown in Figure 3.2, with both the forward (red) and inverse (blue) reaction thresholds and states in the energy region of astrophysical interest.

3.2.1. Experimental details

Two separate measurements were performed at ATLAS. First, a ^{21}Na beam was produced via the d(^{20}Ne,n)^{21}Na reaction as described in Section 2.1. The ^{21}Na beam was focused onto a 380 μg cm^{-2} thick CH_2 target. The Ludwig detector setup (shown schematically in Figure 2.2 and pictured in Figure 3.3) was used with two annular DSSDs covering the angular range from $5 - 20^\circ$ for the outgoing α-particles. The annular IC/PPAC was positioned to cover the angular range from $1 - 5^\circ$ for the recoiling ^{18}Ne and ^{21}Na ions. The incident energy was chosen to measure the excitation function near the 2.52 MeV 2^+ resonance in ^{18}Ne + α (E_x = 10.66 MeV in ^{22}Mg) because it had been reported to decay predominantly to the ground state of ^{21}Na [**6**]. Time reversal invariance dictates that the

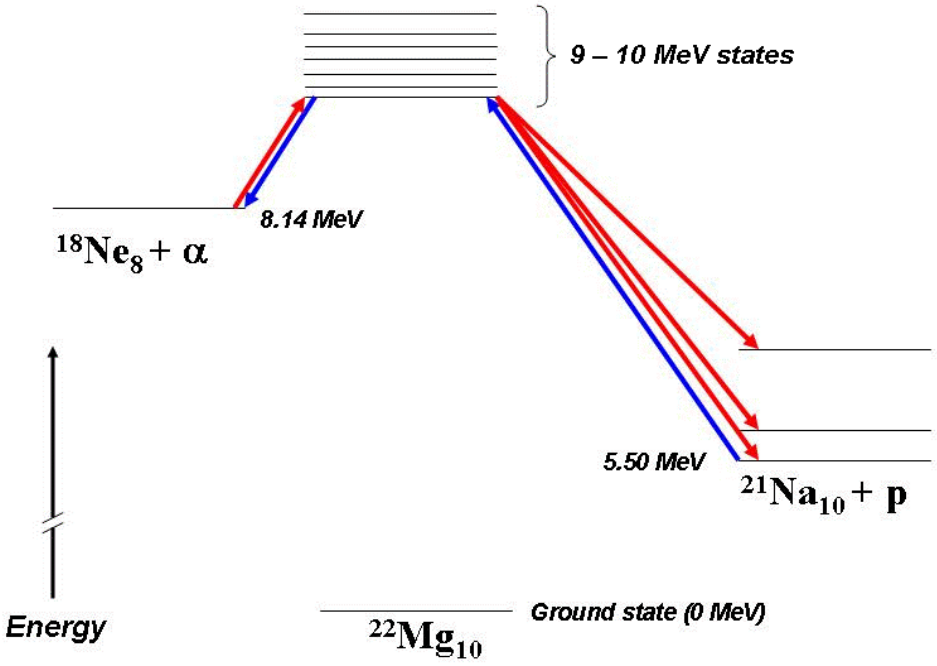

Figure 3.2. Energy level scheme of ^{22}Mg comparing the alpha and proton thresholds and states of astrophysical interest between 9 – 10 MeV. The blue arrows represent how these states were populated in the laboratory (right to left) via the inverse reaction p(^{21}Na,α)^{18}Ne. The red arrows show how the ^{18}Ne(α,p)^{21}Na reaction proceeds in a star (left to right). The first two excited states in ^{21}Na, at 331 and at 1716 keV are also shown.

cross sections for the forward and inverse reactions are related by

$$\sigma_{(18Ne+\alpha)} = \frac{(2J_p+1)\,(2J_{21Na}+1)\,\lambda\!\!\!^{-2}_{(21Na+p)}}{(2J_\alpha+1)\,(2J_{18Ne}+1)\,\lambda\!\!\!^{-2}_{(18Ne+\alpha)}}\sigma_{(21Na+p)} \tag{3.2}$$

For the second run, the beam was produced via p(^{21}Ne,n)^{21}Na with ^{21}Na energies between 82 – 92 MeV ^{21}Na on target covering excitation energies between 9.4 – 9.9 MeV in ^{22}Mg.

Measurement of the time inverse reaction only provides values for Γ_α and Γ_{p0}. Because the ^{18}Ne first excited state is at 1.89 MeV there will be no significant decay to it from ^{22}Mg states in the energy region of interest and we can take $\Gamma_\alpha = \Gamma_{\alpha 0}$. However, the astrophysical reaction can also proceed to excited states in ^{21}Na. To obtain the total cross section of the ^{18}Ne(α,p)^{21}Na reaction via the time inverse reaction, it is also necessary to determine the partial widths $\Gamma_{p'}$. Therefore, a third DSSD was added to detect the protons at angles between $40-60^\circ$ in order to measure the inelastically scattered protons. This technique had been successfully used previously at ATLAS to determine resonance partial widths in ^{18}Ne via measurement of the ^{17}F(p,α)^{14}O and ^{17}F(p,p')^{17}F* reactions [**39**]. The energy resolution, $\Delta E \approx 450$ keV, in the previous experiment was sufficient to separate the 495 keV first excited state in ^{17}F from the ground state. The energy spread of the ^{21}Na beam due to the CH_2 target was measured to be 3.5 MeV on average, corresponding to an energy spread for the outgoing protons of 200 keV. However, due to the 3 mm diameter of the beam spot, the Q-value resolution was limited to $\Delta E \approx 500$ keV for the protons at $\theta_{lab} \approx 50^\circ$. The first excited state in ^{21}Na is only 331 keV above the ground state and, therefore, it could not be separated from the ground state. Two of the DSSDs and the IC/PPAC used for these experiments are pictured in Figure 3.2.

3.2.2. Results

Cross sections were obtained at five energies. The (p,α) cross sections were converted to the (α,p) cross section using Eqn (3.1). The results are plotted as a function of cm energy in the ^{18}Ne + α system in Figure 3.4 along with the cross sections obtained from the two previous experiments described above. The horizontal error bars arise from the

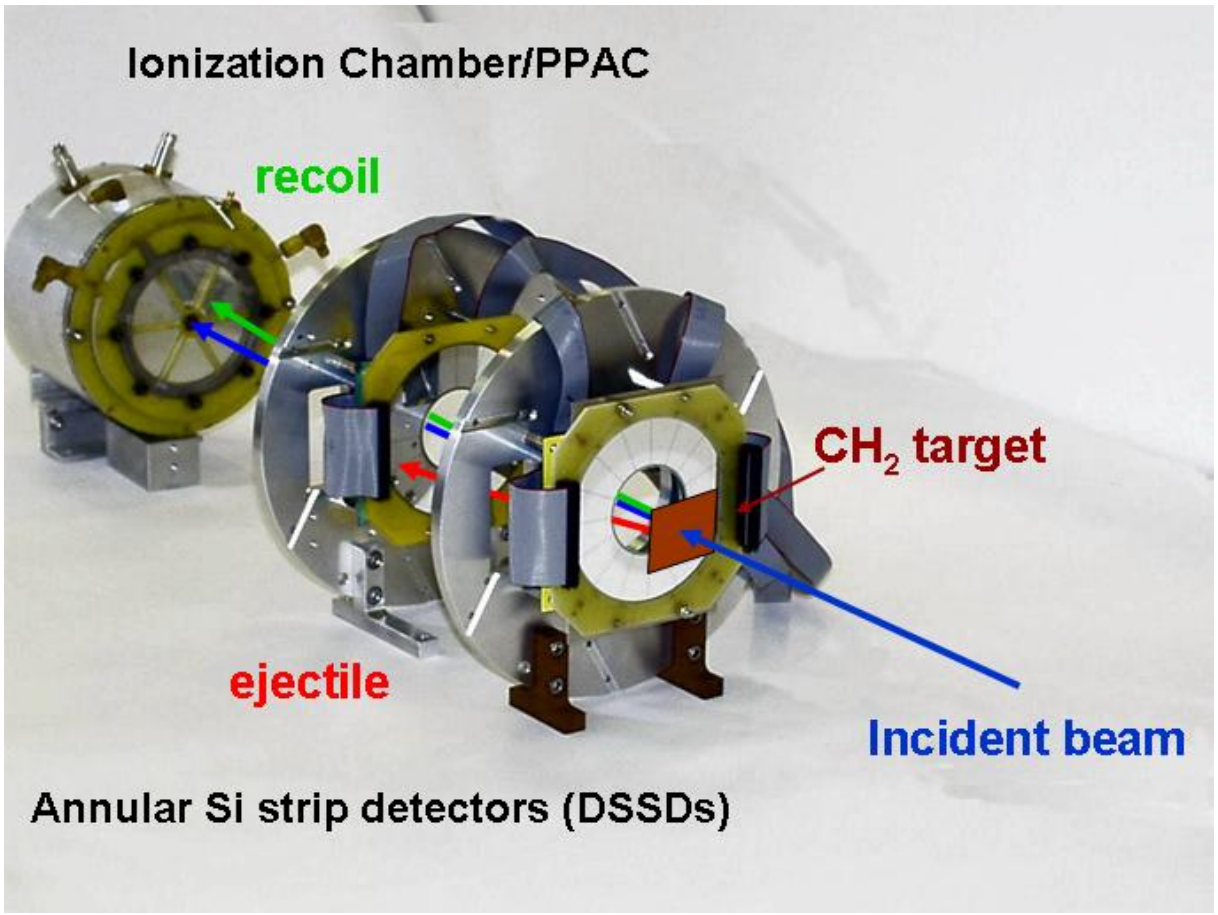

Figure 3.3. The Ludwig detectors with the placement of the solid CH_2 target and particle trajectories of the beam (blue), the recoils (green) and the ejectiles (red). For the first measurement, only the α-particles were measured. A third annular DSSD (not shown) was added for thesecond run to measure the protons as described in the text.

1.6 MeV energy spread of the beam and the 3.5 MeV thickness of the CH_2 target, which corresponds to an average width of 225 keV in the center of mass system. Better resolution was obtained for the alphas because they were detected between $5 \leq \theta_{lab} \leq 20°$, where the angular spread due to the beam spot was smaller than for the protons[b]. No counts were

[b]The protons emitted at angles $\theta_{lab} < 20°$ had energies greater than 11 MeV, and did not stop in the DSSD, or less than 1 MeV and were below the DSSD threshold.

observed above the background for the three lowest energy runs and the upper limits are shown at the 90% confidence level assuming a Poisson distribution.

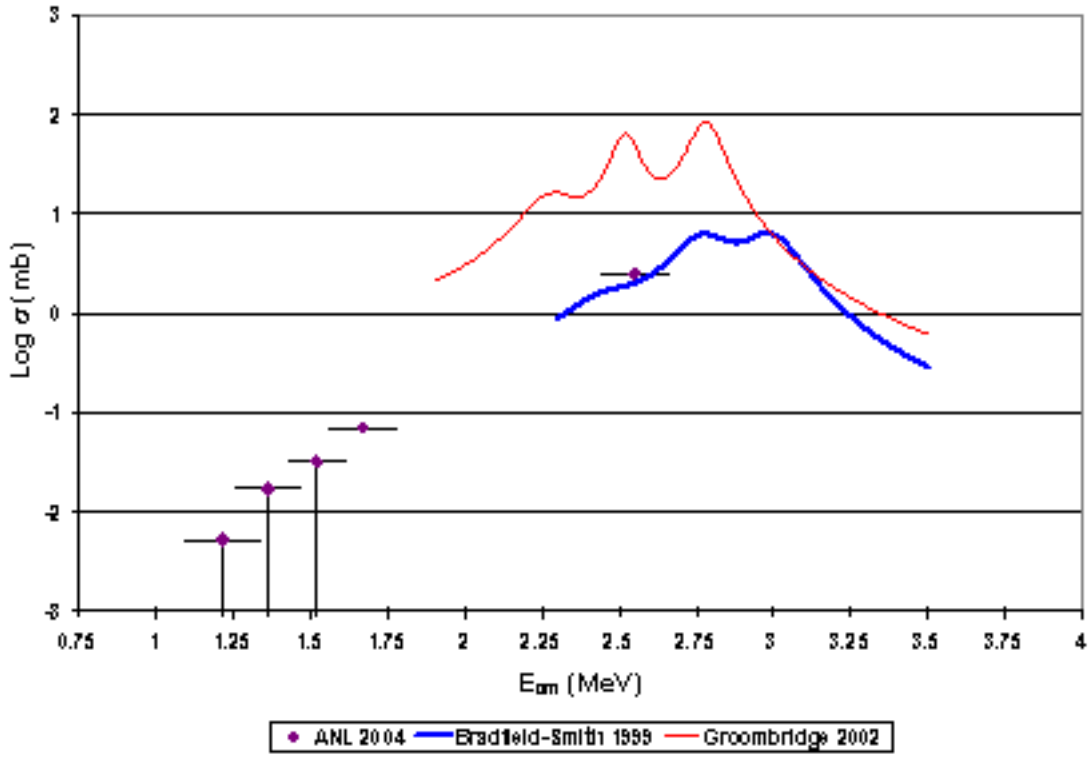

Figure 3.4. Cross sections obtained for the ^{18}Ne(α,p)^{21}Na reaction in this work, compared with those of Bradfield-Smith [**7**] in blue and Groombridge [**6**] in red for ground state transitions only.

Because we were unable to obtain the partial proton widths for states that can decay to excited states in ^{21}Na, the (α,p) cross sections from the present work represent a lower limit. However, we can compare our cross sections with those obtained from references [**7, 6**] for resonances reported to decay primarily to the ground state in ^{21}Na. For the highest energy point, corresponding to the reported resonance at 2.52 MeV, the cross section is consistent with [**7**] and about a factor of 5 smaller than that of [**6**]. The cross

section obtained at an energy corresponding to 1.7 MeV was $\sigma \approx 100$ μb. The upper limits obtained for the cross sections at energies from $1.2 \leq E_{cm} \leq 1.5$ MeV.

3.2.3. Astrophysical implications

The cross section obtained for the ^{18}Ne(α,p)^{21}Na reaction near 2.5 MeV in this work is in good agreement with the earlier measurement of [**7**] for transitions to the ground state of ^{21}Na. It is clear from Figure 3.1 that measurements need to be extended to even lower energies. However, these measurements are exceedingly difficult with the available beam intensities. The upper limit for the lowest energy point in Figure 3.4 was obtained after 2.5 days of run time, with a beam current of $\approx 9 \times 10^5$ pps.

3.3. Studying the ^{15}O(α,γ)^{19}Ne reaction via the branching ratio $\Gamma_\alpha/\Gamma_\gamma$ of the 4.033 MeV 3/2$^+$ state in ^{19}Ne

The first reaction in CNO-cycle breakout path (c) of Section 1.2.3 was also studied using the ATLAS facility. The 123 s half-life of ^{15}O is sufficiently long to allow α-capture, ^{15}O(α,γ)^{19}Ne, which had been considered to be the most likely path for CNO-cycle breakout at novae temperatures, $0.1 \leq T_9 \leq 0.6$, due to the smaller Coulomb barrier, $V_C \approx$ 4.4 MeV, compared to that of the ^{18}Ne(α,p)^{21}Na reaction, $V_C \approx 5.3$ MeV. In this temperature regime, the reaction has been predicted to proceed predominately through the ^{19}Ne 3/2$^+$ state at 4.033 MeV, which is the first state above the ^{15}O + α threshold at 3.529 MeV [**40**]. A partial energy level scheme of ^{19}Ne showing the first few levels above the ^{15}O + α threshold is provided in Figure 3.5.

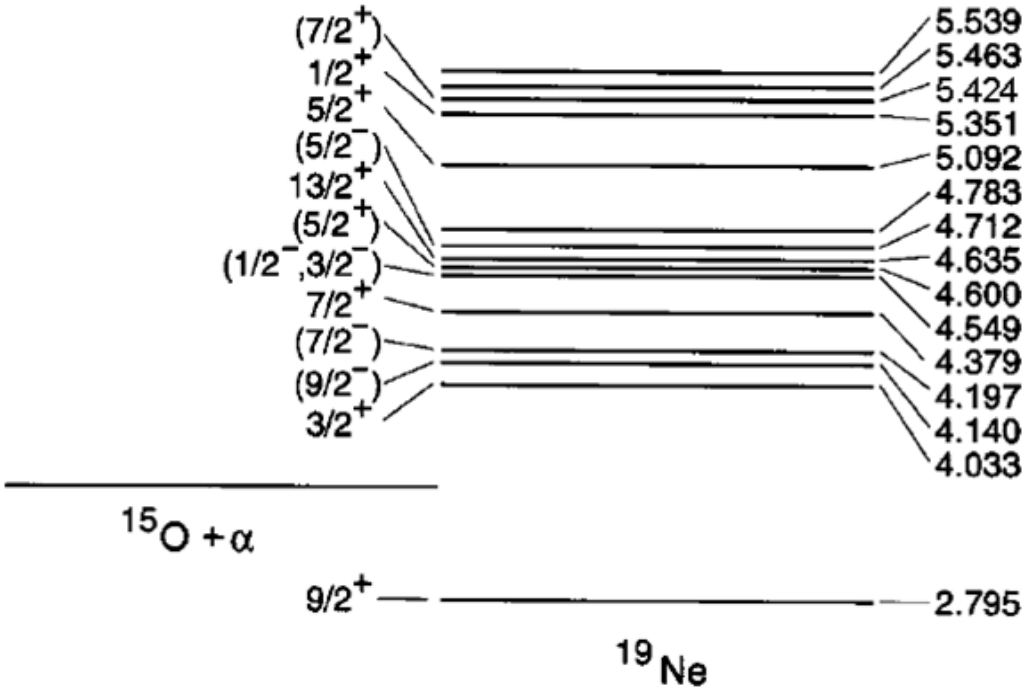

Figure 3.5. Level scheme of ^{19}Ne relevant for the ^{15}O(α,γ) reaction showing the energies in MeV (right) and the assigned spin-parity values (left). The ^{15}O + α threshold is at 3.529 MeV.

The centrifugal barrier for α-capture to this state ($\ell = 1$) is lower than for the next higher states, which are the $9/2^-$ state at 4.140 and the $7/2^-$ state at 4.197 MeV, both of which are suppressed because they require $\Delta\ell = 4$. To calculate the astrophysical reaction rate Eqn (1.22), values for the resonance strengths, $\omega\gamma = \omega\Gamma_\alpha\Gamma_\gamma/\Gamma$, are needed. Due to the high Coulomb barrier ($V_C \approx 4.7$ MeV) for α-decay of this state Γ_α is much smaller than Γ_γ and the resonance strength reduces to $\omega\gamma = \omega\Gamma_\alpha$. The branching ratio for the α-decay of this state has been estimated to be $\approx 10^{-4}$ based on the partial widths of the analog state in the mirror nucleus ^{19}F [**41, 42**].

Many earlier attempts were made to populate the 4.033 MeV state via transfer reactions and to observe the subsequent alpha decay. However, it was found that the state was weakly populated by the ^{19}F(^{3}He,t)^{19}Ne* reaction and that the resulting alpha energies for states near the α-threshold were too low to be detected using normal kinematics [**43, 44**]. One measurement in inverse kinematics was only able to put an upper limit $\Gamma_{\alpha}/\Gamma_{\gamma} < 10^{-2}$, two orders of magnitude larger than the predicted value [**45**]. Attempts were also made to measure the branching ratio at ATLAS by populating states in ^{19}Ne via d(^{20}Ne,t)^{19}Ne* and ^{3}He(^{19}F,t)^{19}Ne* and to look for their subsequent decay to ^{15}O + α or ^{19}Ne + γ. These reactions also weakly populated the 4.033 MeV state and only yielded not very stringent upper limits.

A high resolution study of the ^{20}Ne(^{3}He,α)^{19}Ne reaction at E_{lab} = 15 MeV, revealed a more favorable cross section, $\approx$ 100 μb sr^{-1} in the angular region $\geq 30^{\circ}$ in the center mass system, for populating the 4.033 MeV state [**46**] [c]. It was therefore decided to use the ^{3}He(^{20}Ne,α)^{19}Ne at the same center of mass energy (5 MeV per nucleon). The magnetic spectrograph and scattering chamber detector setup that was used is described in Chapter 2 (Figure 2.3). A $\approx$ 1 pnA 105 MeV ^{20}Ne beam was impingent on the 1.5 mm long gas target containing ^{3}He gas at 700 mbar and cooled to LN_2 temperatures. The resulting target thickness was 50 μg cm^{-2} of ^{3}He, contained within 1.5 mg cm^{-2} Ti foils. The ^{15}O and ^{19}Ne ions were separated in the Enge split-pole magnetic spectrograph (Section 2.3.2), and their timing and energy signals were measured by the gas-filled PPAC and ionization chamber, respectively, located behind the focal plane. The spectrograph was moved to 3.7° off the beam axis to eliminate the background from small-angle scattering of the

[c]Garrett et al. performed a spectroscopic study to determine the properties of states in ^{19}Ne and did not attempt to measure the subsequent α-decay.

primary ^{20}Ne beam. The α-particles were detected in a silicon detector telescope covering an angular range of $6.1 \leq \theta_{lab} \leq 17.2°$. The Si-telescope consisted of a 500 μm thick, 40×40 mm^2 square DSSD to measure position and ΔE and a second 300 μm thick, 50×50 mm^2 silicon detector to measure the residual energy. The second Si-detector was tilted by an angle of 50° to increase the effective thickness to $\approx$ 500 μm for the incident α-particles.

After 3.5 days of running time, no events in the ^{15}O coincidence spectrum were observed from decays of the 4.033 MeV state in ^{19}Ne placing an upper limit on the branching ratio $B_\alpha \leq 6 \times 10^{-4}$ [**47**]. At about the same time an experiment performed at the Kernfysisch Versneller Institute (KVI) in the Netherlands populated the state via the p(^{21}Ne,t)^{19}Ne reaction and obtained an upper limit on B$_\alpha$ of 4.3×10^{-4} [**48**]. These experiments show that the ^{15}O(α,γ)^{19}Ne reaction is not a significant breakout path from the CNO-cycle at nova temperatures (T$_9$ = 0.1 – 0.4). However, this reaction may become important for CNO-cycle breakout at higher temperatures, such as those found in x-ray bursts and in super-massive stars [**49**]. A recent publication claims to have experimentally determined the branching ratio, $B_\alpha = 2.9 \pm 2.1 \times 10^{-4}$, for the 4.033 MeV state [**50**]. Their result was obtained through a measurement of the α-decay of the 4.033 MeV state populated via ^{19}F(^{3}He,t)^{19}Ne* reaction. However, this result appears to be questionable. Based on the signal to background ratio of the data presented, it appears that alpha branching ratio should have been quoted as an upper limit of $\leq 4 \times 10^{-4}$. Doppler Shift Attenuation Method measurements of the lifetime of this state have been made by various groups: $\tau = 13^{+9}_{-6}$ fs [**51**],$\tau = 11^{+4}_{-3}$ [**52**], and $\tau = 6.9^{+2.1}_{-2.1}$ [**53**]. The most recent lifetime corresponds to Γ_γ = 95 meV. Using the relation $\Gamma_\alpha = B_\alpha \Gamma_\gamma$, with the upper limit on

the branching ratio of 4×10^{-4} gives $\Gamma_\alpha \leq 38$ μeV. The resonance strength can then be determined from $\omega\gamma = \frac{(2J+1)}{2} B_\alpha \left(1 - B_\alpha\right) \frac{\hbar}{\tau} \leq 0.76$ μeV.

CHAPTER 4

^{19}Ne(p,γ)^{20}Na and the 2.645 MeV state in ^{20}Na

4.1. Introduction and Background

The ^{15}O(α,γ)^{19}Ne(p,γ)^{20}Na reaction path is expected to be the dominant path for breaking out of the HCNO cycle into the *rp*-process in the early ignition stages of X-ray bursts [**40, 1**]. The leakage rate for breakout is determined by the slower of the two reactions, which is assumed to be the first reaction (discussed in the previous chapter) due to the higher Coulomb barrier. The ^{19}Ne(p,γ)^{20}Na reaction is thought to proceed predominantly through the 2.645 MeV state in ^{20}Na, which is the first state above the ^{19}Ne + p threshold at 2.195 MeV [**40**]. For an isolated, narrow resonance at energy E_r, the reaction rate per particle pair depends onlyon the temperature and the resonance strength $\omega\gamma$, given by Eqn (1.21):

$$\langle \sigma \mathrm{v} \rangle = \left(\frac{2\pi}{\mu k T} \right)^{3/2} \hbar^2 \omega\gamma \exp\left(-\frac{E_r}{kT} \right). \tag{4.1}$$

The strength of a ^{20}Na resonance for proton capture by ^{19}Ne is given by Eqn (1.20). Here, $J^\pi = 1/2^+$ for the ground state of ^{19}Ne and also for the proton in the entrance channel, so that the resonance strength becomes

$$\omega\gamma = \frac{(2J_r + 1)}{4} \frac{\Gamma_{p0}\Gamma_\gamma}{\Gamma}, \tag{4.2}$$

where Γ_{p0} represents the ground state proton width and Γ_{γ} represents the total width for γ-decay. Ideally, the resonance strength can be obtained by measuring the ^{19}Ne(p,γ)^{20}Na reaction directly. To measure the relatively small strength of this astrophysically important first resonance above the proton threshold requires a ^{19}Ne beam of intensity not presently available. Therefore, the resonance strength was first estimated from the known level structure of the mirror nucleus ^{20}F [**40**] because there was very little information available about the level structure of ^{20}Na above the proton threshold. It has been stated that, 'the rate of the ^{19}Ne(p,γ)^{20}Na reaction cannot be estimated with any degree of confidence until J^{π} for the 447 keV resonance has been established' [**3**]. Due to its importance in the breakout from the HCNO cycle, many attempts have been made to determine the resonance parameters of this state, though none has succeeded in unambiguously identifying the spin. The next section summarizes the work that was done to determine the level structure and resonance parameters of the first few states above the proton threshold in ^{20}Na.

4.2. Survey of previous work

Information about the level structure and resonance parameters (E_r, Γ_{γ}, Γ_{p0}, Γ_{p1}, and J) of ^{20}Na can be obtained in various ways. Resonance energies are obtained from nuclear reaction measurements. Partial widths can sometimes be extracted from a line shape analysis of the decay particle spectrum as mentioned in the previous chapter. However, the partial widths of the narrow resonances of interest here are of the order of a few eV, while typical experimental energy resolutions are between tens and a few hundred keV. Properties of states in ^{20}Na have been determined in a variety of nuclear reactions described

below. Figure 4.2 shows a level scheme of ^{20}Na with the various ways of populating states above the proton threshold. These include the charge exchange reactions ^{20}Ne(^{3}He,t)^{20}Na, ^{20}Ne(p,n)^{20}Na, and the β^{+}-decay of ^{20}Mg. These experiments are summarized below.

4.2.1. ^{20}Ne(^{3}He,t)^{20}Na

The previous (^{3}He,t) measurements to determine the spin and parity of the 2.645 MeV state were conducted in "normal kinematics" with a ^{3}He beam on a ^{20}Ne gas target (Refs [**54, 55, 56, 57, 58, 12, 59, 60**]). The authors of references [**54**] through [**12**] measured angular distributions and compared them to DWBA calculations. While these measurements agree at larger angles $\theta_{CM} > 40°$, there is some discrepancy at smaller angles and no data at $\theta_{CM} < 10°$. The minimum angle is significant, because a peak at 0° is characteristic of an $\ell = 0$ transition, and would unambiguously rule out the $J^{\pi} = 3^{+}$ assignment. However, without having data near $\theta_{CM} = 0°$, the resulting angular distributions have been variously argued to be consistent with $\ell = 0$, $\ell = 2$, or a combination of both. This ambiguity has led to controversy regarding the spin of this state. The authors of [**56**] and [**58**] assigned a 1^{+} spin based on comparison with DWBA calculations and guided by associating the states with the known level scheme of the mirror nucleus ^{20}F. Initially, Kubono et al [**56**] assumed the 2.645 MeV state to be the mirror of the 3.488 MeV 1^{+} state in ^{20}F, which is known to have a dominant single-particle (s-wave) structure. However, Lamm et al [**58**] identified the 2.645 MeV state in ^{20}Na with the 3.172 MeV 1^{+} "intruder" state in ^{20}F (see Section 4.2.5). Clarke et al. [**12**], first concluded that this state was either 1^{+} or 1^{-}, based on DWBA fits to the ^{20}Ne(^{3}He,t) angular distributions at forward angles. They also measured the mirror reaction ^{20}Ne(t,^{3}He)^{20}F at the same beam energy

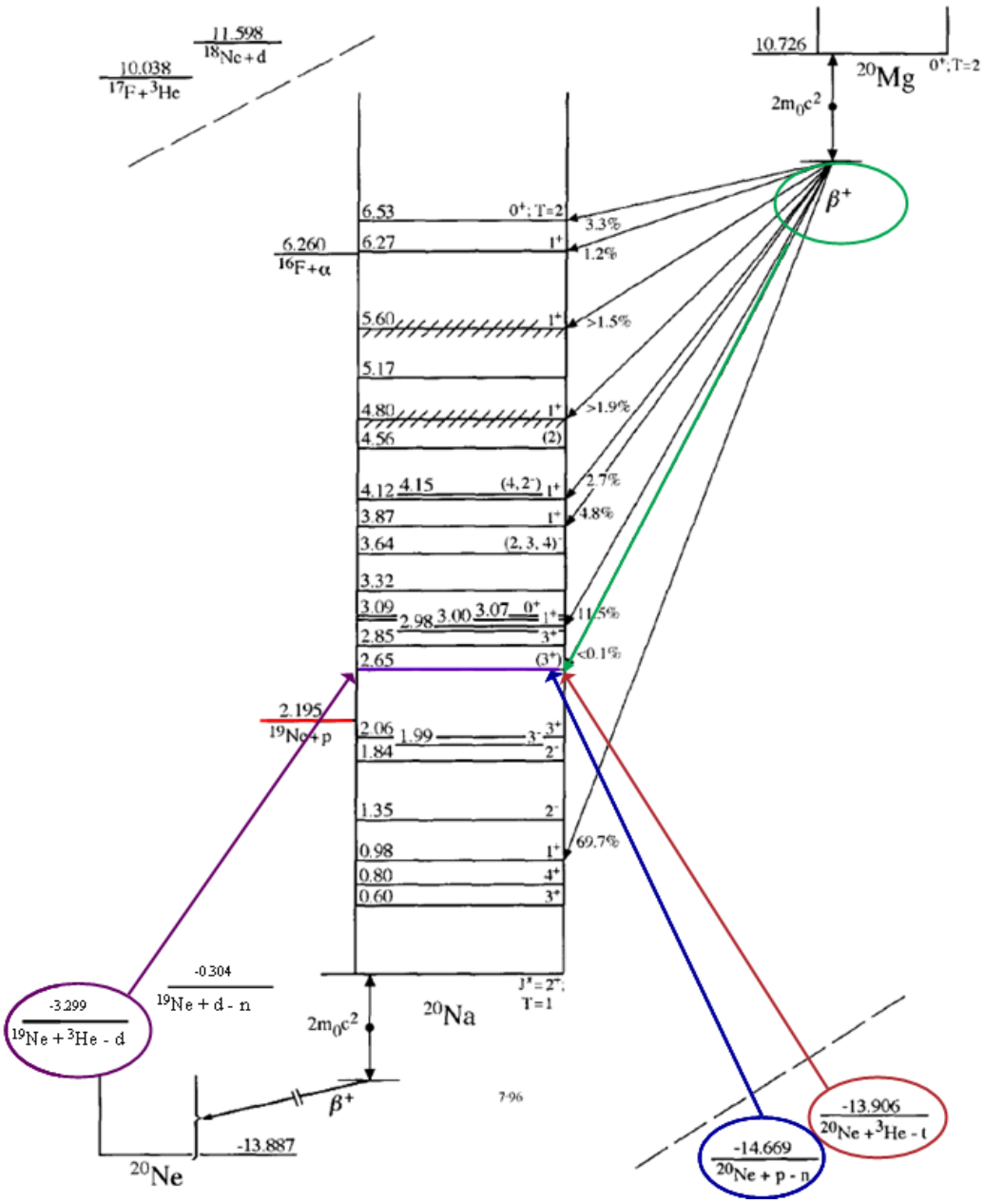

Figure 4.1. Level diagram of ^{20}Na depicting various ways to populate the 2.645 MeV state. The state has been populated via charge exchange reactions ^{20}Ne(^{3}He,t) (brown) and ^{20}Ne(p,n) (blue), the β-decay of ^{20}Mg (green), and the ^{19}Ne(^{3}He,d) transfer reaction (violet). The ^{19}Ne + p threshold is shown in red. (Taken from the compilation by Tilley et al. [**8**])

using the same gas target, and observed only a few counts in their spectra for the 3.172 MeV state and concluded that this state is very weakly excited.

Measurements of the ^{20}Mg β^+-decay (see below) cast some doubt on the 1^+ assignment for the 2.645 MeV state in ^{20}Na. Brown et al. challenged the $J^\pi = 1^+$ spin assignment, arguing that if this state were the mirror of the 3.172 MeV state in ^{20}F, it would be weakly populated in the (^{3}He,t) reaction, and have a negligible Coulomb shift [**61**]. The authors further argued against the $J^\pi = 3^+$ for the 2.849 MeV state in ^{20}Na, stating that this assignment implies a negative parity for the 2.645 MeV state. Based on the available mirror candidates in ^{20}F, Brown et al. proposed $J^\pi = 3^+$ for the 2.645 MeV and $J^\pi = 3^-$ for the 2.849 MeV state, identifying them as the mirrors of the 2.966 MeV and the 2.865 MeV states in ^{20}F, respectively. This prompted Clarke et al. to reanalyze their data and to compare the angular distributions to these two states in ^{20}Na in the ^{20}Ne(^{3}He,t)^{20}Na reaction with those to the proposed mirror states in ^{20}F in the ^{20}Ne(t,^{3}He)^{20}F reaction [**62**]. Based on this comparison, these authors favored the mirror assignments proposed by Brown et al. in Ref [**61**].

Smith et al. [**59**], performed a high-resolution study of the ^{20}Ne(^{3}He,t)^{20}Na reaction giving values for the resonance energies accurate to 9 keV for states above the proton threshold, but did not perform a DWBA analysis. This experiment firmly identified the first four states above the proton threshold in ^{20}Na and eliminated a fifth state at 3.1 MeV proposed by Lamm et al. [**58**].

Hofstee et al, attempted to measure the branching ratio Γ_γ/Γ of the 2.645 MeV state by comparing single triton events to $t-\gamma$ coincidences. They showed that the coincidence yield for states above the proton threshold was low, but due to a large overall background

were only able to report an estimate of $\Gamma_\gamma/\Gamma \approx 10\%$ [**60**]. This estimate is consistent with the present work.

4.2.2. ^{20}Ne(p,n)^{20}Na

Two measurements of the ^{20}Ne(p,n)^{20}Na angular distributions have been reported [**56, 63**]. Kubono et al., showed an enhancement of the cross section at $\theta_{CM} \approx 3^\circ$ with E_p = 35 MeV, and concluded that $J^\pi = 1^+$ based on comparison with DWBA calculations [**56**]. Anderson et al, observed a dip in the cross section at $\theta_{CM} \approx 0^\circ$ with $E_p = 135$ MeV, and concluded that the dip implies an absence of $\ell = 0$ strength, therefore favoring the $J^\pi = 3^+$ assignment [**63**].

4.2.3. β^+-decay of ^{20}Mg

Theoretical calculations [**40**] predicted that states above the proton threshold would decay predominantly by proton emission. This prediction was the basis for the branching ratio measurement by [**60**], and was confirmed in the present work. Three attempts to measure delayed protons following the β^+-decay of ^{20}Mg have been reported [**64, 65, 66**]. None of these experiments observed any protons from the 2.645 MeV state, with the most stringent limits on the branching ratio for β-decay to this state being $\leq 0.1\%$ with log $ft \geq 6.24$ [**66**]. If this state is the analog of the intruder state in ^{20}F, then the β-decay can be strongly inhibited. It should be noted that the proposed $J^\pi = 1^+$ mirror state in ^{20}F at 3.172 MeV also shows no feeding from the β^--decay of ^{20}O (see Section 4.2.5). Piechaczek et al. also point out that in *sd*-shell nuclei there are cases (^{17}N, ^{17}Ne and ^{18}N)

of allowed β-transitions that have $\log ft > 6$ [**67**]. Therefore, a $\log ft \geq 6.24$ may not rule out the 1^+ assignment.

4.2.4. ^{19}Ne(p,γ)^{20}Na

The first attempt to measure the proton capture by the ^{20}Na 2.645 MeV state was made at the cyclotron radioactive ion beam facility in Louvain-la-Neuve, Belgium in 1994 [**68**]. However, they were only able to give an upper limit on the strength of the 447 keV resonance of $\omega\gamma \leq 24$ meV. Subsequent measurements by the same group over the next few years using different targets and detection techniques [**69, 9**] were later combined, renormalized, and summarized in a global analysis by Vancraeynest et al. [**9**]. The data were then analyzed in terms of the resonances strengths of the four lower lying states above the proton threshold. An upper limit on the strength of the 447 keV resonance, which corresponds to the 2.645 MeV state in ^{20}Na, was reported as $\omega\gamma \leq 21$ meV at the 90% confidence level. The next three resonances at 661, 797 and 887 keV, which correspond to the 2.849, 2.992, and 3.082 MeV states in ^{20}Na, were combined to give upper and lower limits on the sum of their strengths (see [**9**] for details). The resonance strengths were then used to calculate the resonant contribution to the ^{19}Ne(p,γ)^{20}Na reaction rate. However, the ^{19}Ne(p,γ)^{20}Na reaction rate was still uncertain by 2 – 3 orders of magnitude over the temperature range $0.3 < T_9 < 1.3$ (see Figure 4.2). The upper limit on the total reaction rate shown in the figure was obtained by taking the sum of the direct capture rate, the upper limit on the resonant rate for the 447 keV resonance, and the upper limit on the sum of the contributions from the three higher resonances. The lower limit was obtained by summing the direct capture rate and the lower limit on the sum of the contributions

of the three higher resonances, and setting the lower limit from the 447 keV resonance to zero.

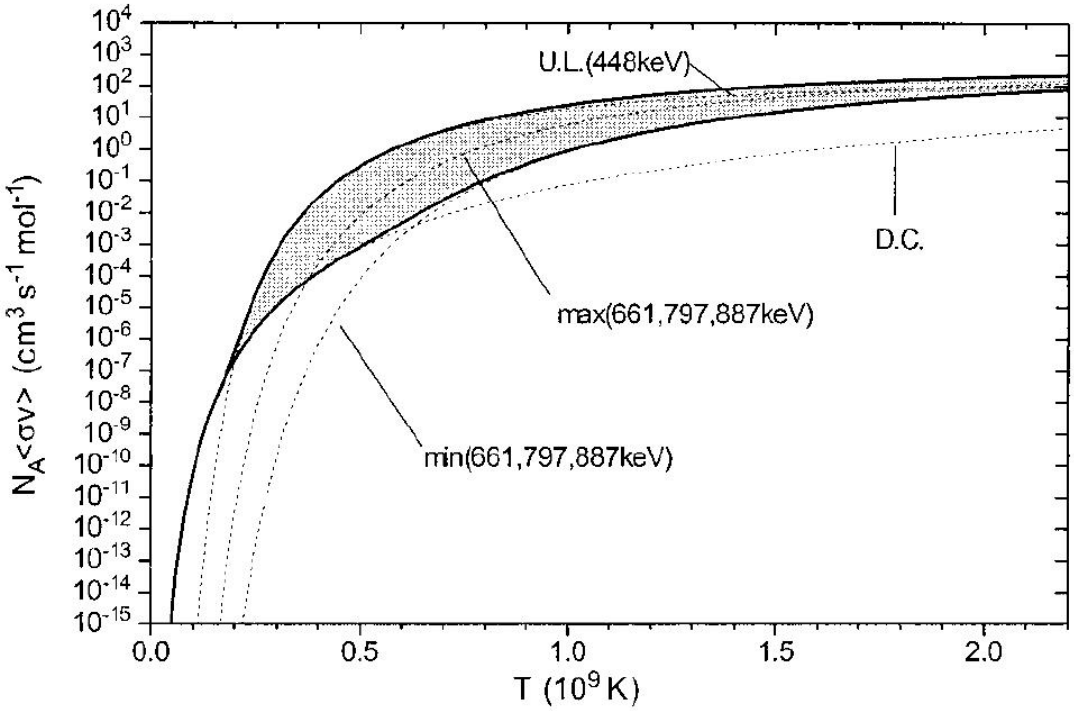

Figure 4.2. Astrophysical reaction rate vs. temperature for the ^{19}Ne(p,γ)^{20}Na reaction (taken from Ref [**9**]). The solid lines show the limits on the total reaction rate and the dotted lines show the contributions to the total reaction rate due to direct capture (DC) component and the limits on the resonant components as described in the text.

A more recent measurement of the ^{19}Ne(p,γ)^{20}Na reaction was reported using a new recoil separator at the same facility, which further reduced the upper limit to $\omega\gamma \leq 15$ meV [**70**].

In summary, measurements of the ^{19}Ne(p,γ)^{20}Na reaction conducted over a 10-year period have been unable to obtain a value for the resonance strength and were only able to reduce the upper limit from $\omega\gamma \leq 24$ meV to $\omega\gamma \leq 15$ meV. This highlights the difficulty

in measuring radiative capture reactions with the low intensity RIBs that are currently available.

4.2.5. Information from the mirror nucleus ^{20}F

Properties of states in ^{20}Na have also been inferred from properties of states in the isospin mirror nucleus ^{20}F (as mentioned above). States in ^{20}F are easily populated via the ^{19}F(d,p)^{20}F reaction, which has a large cross section, charged particle reaction products, and utilizes a stable (deuteron) beam and easily fabricated target. States in ^{20}F can also be populated via thermal neutron capture [**11**] on ^{19}F, and other reactions, which have been compiled [**8**]. Consequently, much more information is available on the level structure of ^{20}F than on ^{20}Na. Shell model calculations based on information from known states in ^{20}F can then be used to predict the properties of analog states in ^{20}Na. The two states in ^{20}F that have been proposed as the possible analog of the 2.645 MeV state in ^{20}Na are the $J^\pi = 3^+$ 2.966 MeV and the $J^\pi = 1^+$ 3.172 MeV states.

The $J^\pi = 3^+$ assignment for the 2.966 MeV is well established from a combination of (d,p) reactions and partial lifetime measurements (summarized in [**11**] and [**8**]). The spin and parity of the 3.172 MeV state in ^{20}F, however, is less certain. The state is weakly populated in transfer reactions and its lifetime is not known. This state is observed to have "small single-particle strength for $\ell = 2$ formation and no discernible $\ell = 0$ strength" [**59**]. A DWBA study of the ^{19}F(d,p)^{20}F reaction is consistent with $\ell = 2$ transfer implying $J^\pi = (1,\ 2,\ \text{or}\ 3)^+$ [**71**]. A similar analysis of the ^{18}O(^{3}He,p)^{20}F reaction revealed $\ell = 0$ and $\ell = 2$ components in the angular distribution of the 3.172 MeV state, consistent with a $J^\pi = 1^+$ assignment [**72**]. The only observed γ-decay of this state, populated

via ^{18}O(^{3}He,p)^{20}F, is an E1 transition to the $J^{\pi} = 1^{-}$ state at 984 keV in ^{20}F [**73, 74**]. No Gamow-Teller strength for a $J^{\pi} = 0^{+} \rightarrow 1^{+}$ transition to this state was observed from the β^{-}-decay of ^{20}O placing an upper limit on the branching ratio BR $< 0.012\%$ and a lower limit on log $ft > 5.08$ [**75**]. These observations are consistent with the state being described as the first 1^{+} 2 $\hbar\omega$ core-excited intruder state with a 6-particle 2-hole configuration – $(1p)^{-2}(2s1d)^{6}$ [**75, 72**]. Evidence against the $J^{\pi} = 1^{+}$ assignment for this state comes from thermal neutron capture experiments. The 3.172 MeV state is weakly populated following thermal neutron capture by ^{19}F [**76, 11, 77**]. The capture is primarily direct capture [**11**] and therefore the initial system is a superposition of 0^{+} and 1^{+} states. No direct capture was observed to the 3.172 MeV state, nor were transitions observed from the $J^{\pi} = 2^{-}$ states at 5.936 and 6.018 MeV, through which most of the capture proceeds [**11, 8**]. Raman et al., observed very weak transitions from the 3.965 MeV 1^{+} state to the 3.172 MeV state, and from the 3.172 MeV state to the 984 keV 1^{-} state [**11**]. The authors therefore prefer $J \geq 3$ or $J = 0$, and favor $J^{\pi} = 0^{-}$ but do not rule out the $J^{\pi} = 1^{+}$ assignment with a $6p2h$ configuration [**11**]. Another spin assignment, $J^{\pi} = 1^{-}$, was proposed for the 3.172 MeV state using a microscopic three-cluster model [**78**]. However, the thermal neutron capture results [**11**] argue against this assignment.

A study of the ^{14}N(^{7}Li,p)^{20}F reaction exploiting the compound-nuclear proportionality rule, or "$2J + 1$" rule, supports the 1^{+} assignment [**10**]. The (^{7}Li,p) cross sections for states below 4.0 MeV in ^{20}F are plotted against $2J + 1$ in Figure 4.3. The proportionality relationships for positive (black) and negative (red) parity states, given by $\sigma_{tot}/(2J+1) = 4.95 \pm 0.22$ and $\sigma_{tot}/(2J+1) = 6.50 \pm 0.47$, respectively, are shown with their uncertainties

(dash-dotted lines) [**10**]. The $15.61 \pm 0.85\mu$b cross section for the 3.172 MeV state (blue) clearly favors $J^\pi = 1^+$.

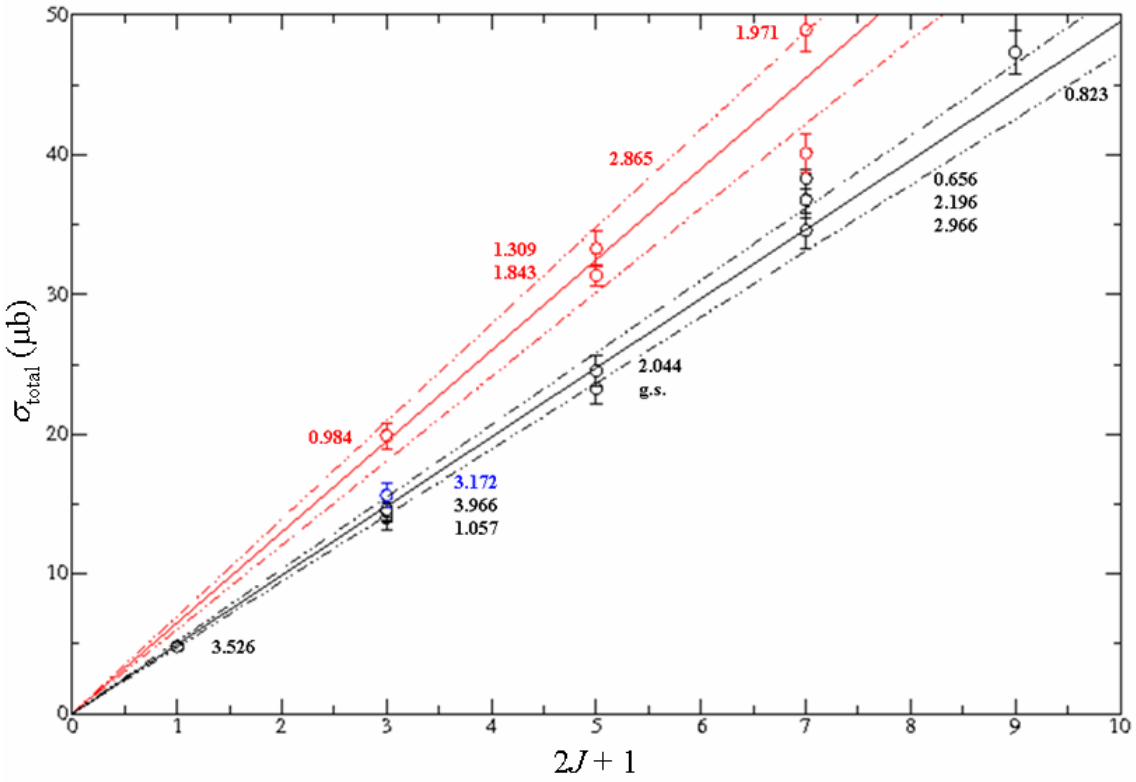

Figure 4.3. Total angle-integrated cross section vs. $2J + 1$ for the ^{14}N(^{7}Li,p)^{20}F reaction at 16 MeV (Ref [**10**]). The solid lines are fits by Fortune & Bishop to the cross section being proportional to $2J + 1$ for positive (black) and negative (red) parity states. The ^{20}F states are labeled by their excitation energy in MeV.

4.2.6. Shell model calculations

Early estimates of the ^{19}Ne(p,γ)^{20}Na reaction rate calculated by Wallace and Wooseley [**14**] included the only then known resonance at 2.89 MeV in ^{20}Na, with all other resonances assumed from the known states in ^{20}F. The partial widths, when known, were taken

directly from the analog states and in some cases were guessed from properties of neighboring analog states. More sophisticated calculations corrected for the Thomas-Ehrmann shift of resonant states in ^{20}Na relative to their bound counterparts in ^{20}F, assuming that the reduced widths were equal, $\theta_p^2 = \theta_n^2$, for analog states [**40**]. Progress over the years has increased the accuracy and the sophistication of shell-model calculations. Shell model calculations in the A = 20, T = 1 system have been made for energies up to 4 MeV [**11**], using two-body matrix elements and interaction potentials constructed by Warburton, Towner, Brown, and Wildenthal [**79, 80, 81**]. The calculated energy levels, labeled by their J^π values and energy, are compared to experimental energy levels in ^{20}F and ^{20}Na in Figure 4.4. All the sub-threshold states in ^{20}Na have been identified with their mirror partners. The level assignments for the first two states above the proton threshold proposed by Lamm et al [**58**] (black) and Brown et al [**61**] (brown) are indicated. The ^{19}Ne + p threshold and the Gamow energy window for this reaction at four different temperatures are shown on the right side of the figure.

Once a state in ^{20}Na has been identified with an analog state in ^{20}F, resonance parameters in ^{20}Na can be calculated, correcting for the Coulomb energy difference and Thomas-Ehrmann shift. Many of the conclusions from the reported work on ^{20}Na states have relied on this identification with analog states in ^{20}F. The choice of the proposed analog of the 2.645 MeV state implies a different analog for the neighboring 2.849 MeV state in ^{20}Na. The two proposed level schemes for the first two states above the proton threshold in ^{20}Na have boiled down to $J^\pi = 1^+$ and 3^+ and $J^\pi = 3^+$ and 3^-, for the 2.645 MeV and the 2.849 MeV states, respectively. These two schemes correspond to three

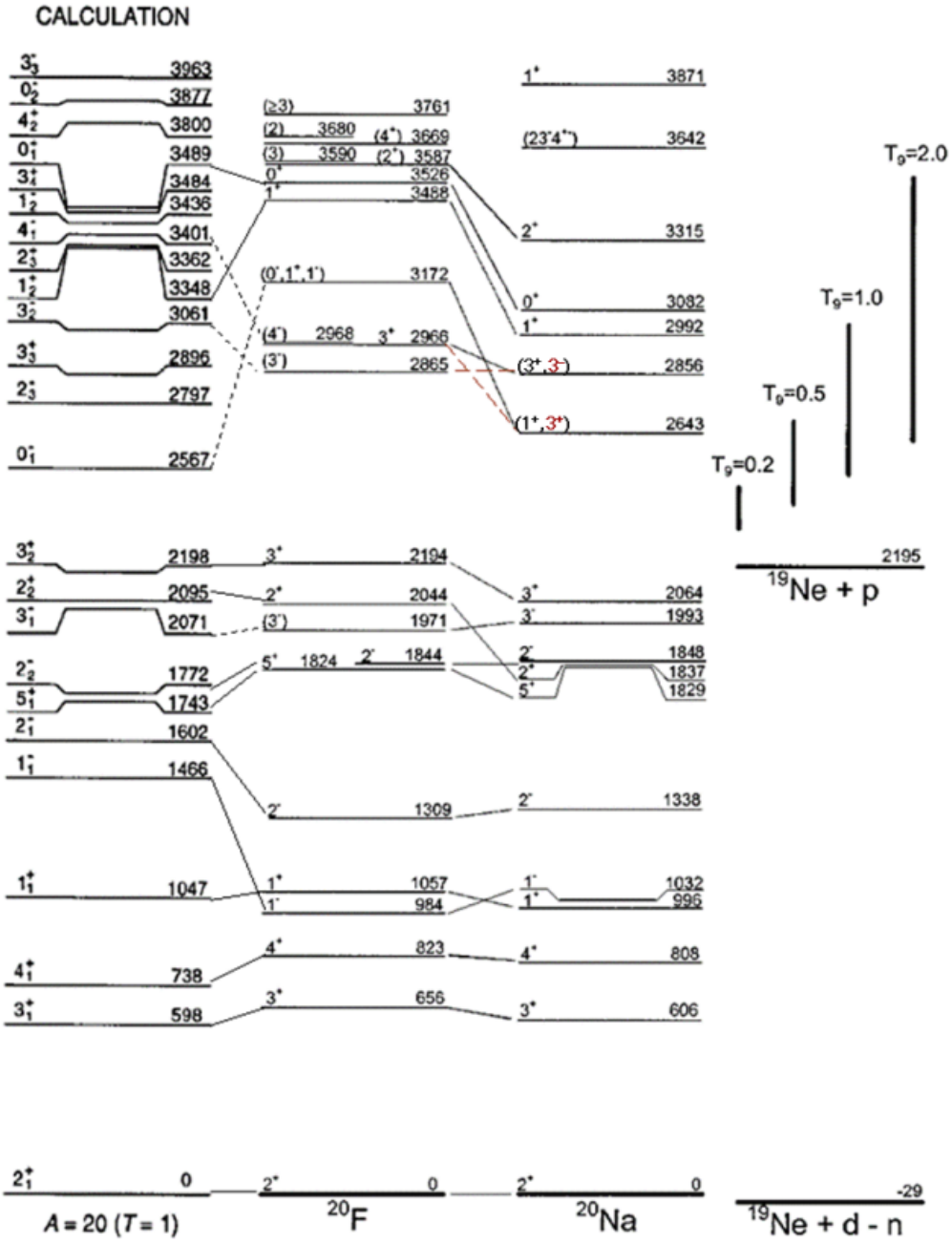

Figure 4.4. Level scheme comparing calculated and experimental energy levels for ^{20}F and ^{20}Na with lines connecting possible analog states. The ^{19}Ne + p threshold is shown on the right with Gamow windows for temperatures ranging from $0.2 \leq T_9 \leq 2$. (Adapted from Ref [**9**], and Ref [**11**])

analog states in ^{20}F – the 1^+ state at 3.172 MeV, the 3^+ state at 2.966 MeV, and the 3^- state at 2.865 MeV (see Figure 4.4).

The two spin assignments lead to different predictions for the resonance strength of this state and, hence, different values for the thermonuclear reaction rate. The single particle proton widths have been calculated [**9**] using a folding Woods-Saxon potential and scaled by the spectroscopic factors measured for the mirror states in ^{20}F converted to their equivalent in ^{20}Na using the shell model code OXBASH. For the proposed 1^+ intruder state, however, experimental neutron spectroscopic factors were used [**71**]. The gamma widths were estimated from lifetimes that were calculated, as described in reference [**61**]. Fortune et al. [**82**] used the measured upper limit on the lifetime of the 2.966 MeV 3^+ mirror state in ^{20}F [**83**] to place an upper limit on the gamma width of the 2.645 MeV state in ^{20}Na. If the latest value of $\tau(^{20}\text{F}, 3^+, 2.966) = 5.2$ fs [**11**] is used, this leads to a value for the resonance strength, $\omega\gamma(^{20}\text{Na}, 3^+, 2.645) = 36.4$ meV, which is inconsistent with the experimental upper limit [**70**] of $\omega\gamma \leq 15$ meV. It should be noted that Fortune et al. used earlier, less stringent limits on both the lifetime of the ^{20}F 2.966 MeV analog state and on the proton capture through the ^{20}Na 2.645 MeV state and therefore concluded that the inferred and measured resonances strengths were consistent. The results of the calculations are summarized in Table 5.1 along with the current results.

To resolve this discrepancy, either a better measurement of the ^{19}Ne(p,γ) reaction is necessary, or the spin of the 2.645 MeV state needs to be determined. The following two experiments, conducted between March 2003 and April 2006, set out to resolve this controversy. The first experiment discussed below attempted to determine the spin of the 2.645 MeV state via a measurement of the angular distribution of the ^{3}He(^{19}Ne,d)^{20}Na

reaction. The second experiment populated the 2.645 and 2.849 MeV states via the ^{3}He(^{20}Ne,t)^{20}Na reaction and measured the branching ratio Γ_p/Γ_γ of the subsequent decay for each state.

4.3. Determining the spin of the 2.645 MeV state from the ^{3}He(^{19}Ne,d)^{20}Na angular distribution

4.3.1. Background

One way to resolve this issue is to obtain an angular distribution for feeding this state in a transfer reaction and compare it to DWBA calculations. The ^{3}He(^{19}Ne,d)^{20}Na reaction was chosen using a ^{19}Ne beam impinging on a ^{3}He target. In this reaction a 1^+ state in ^{20}Na can be populated via an angular momentum transfer $\ell = 0$ or 2, while the 3^+ assignment requires an $\ell = 2$ or 4 transfer. Previous attempts to determine the spin of this state from angular distributions were made using the charge exchange reactions ^{20}Ne(^{3}He,t)^{20}Na [**56, 58, 12, 59**] and ^{20}Ne(p,n)^{20}Na [**56, 63**] discussed above. Because (^{3}He,d) is a "stripping" reaction and does not require exchanging a nucleon with the target nucleus, the angular momentum transfer should be easier to determine from the angular distribution of the outgoing deuterons than for charge exchange or "knock out" reactions. The code PTOLEMY was used to perform DWBA calculations for the ^{19}Ne(^{3}He,d)^{20}Na reaction with a bombarding energy of 4.0 MeV/u. The results are shown in Figure 4.5. The calculations reveal a distinctively different shape for $\ell = 0$ and $\ell = 2$ transfers over the angular range $30 - 50^o$ in the center of mass system (cm). In this region there is a clear minimum and maximum in the angular distribution for $\ell = 0$ transfer compared with a continuous falloff for $\ell = 2$. If the measured angular distribution over this angular

range exhibits the characteristic shape of an $\ell = 0$ transition, we should be able to rule out the $J^{\pi} = 3^{+}$ spin assignment.

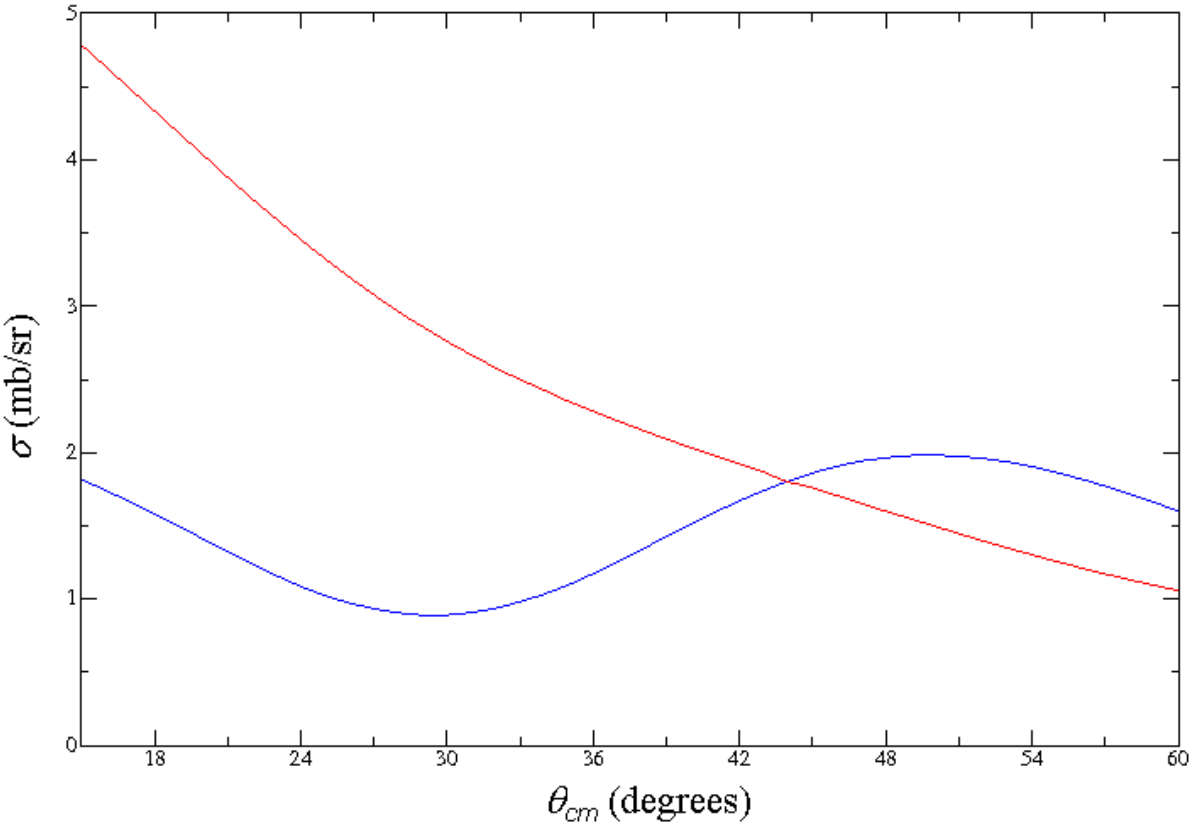

Figure 4.5. DWBA calculation of the ^{19}Ne(^{3}He,d)^{20}Na reaction at 4 MeV/u populating the 2.645 MeV state in ^{20}Na. The calculation reveals distinctly different behavior for $\ell = 0$ transfer (blue) and $\ell = 2$ transfer (red) in the angular range $30 \leq \theta_{cm} \leq 50°$

4.3.2. Experimental details

The reaction was measured in inverse kinematics using a ^{19}Ne beam produced via the p(^{19}F,n)^{19}Ne reaction using the in-flight technique as described in Section 2.1. The gas target was filled with ^{3}He to 700 mbar and cooled with LN_2 providing a target thickness of

≈ 40 μg cm^{-2}. The critical center-mass angle region of $30-50^{\circ}$ corresponds to laboratory deuteron angles ranging from $51.5-53^{\circ}$ for the 2.645 MeV state for an incident ^{19}Ne beam energy of 76 MeV (4 MeV per nucleon). The Ludwig detector setup (described in Section 2.2, and shown in Figures 2.2 and 3.3) was used with the annular DSSD covering angles from $45 \leq \theta_{lab} \leq 61^{\circ}$ for the outgoing deuterons. The annular IC/PPAC was positioned to cover the angular range of $1-5^{\circ}$ for the recoiling ^{20}Na which were detected in coincidence with the deuterons.

4.3.3. Discussion

Due to the low secondary beam intensity of $\approx 10^5$ ^{19}Ne s^{-1} and the ^{19}F contamination from the primary beam this measurement relied heavily on the kinematic coincidence technique and therefore on accurate particle identification of the recoils and on good angular resolution in detecting the deuterons. In order to separate the 2.645 MeV state from the neighboring 2.849 MeV state, an angular resolution of $\approx 1^{o}$ was required for the outgoing deuterons. Prior to the run, energy loss and angular scattering calculations were performed using the SRIM 2006 [**31**] code for the outgoing deuterons passing through the exit foils, which were usually titanium or Havar®. These calculations revealed that the angular straggling of deuterons through the exit foil was $1 \leq \Delta\theta \leq 1.5^{\circ}$. The same calculation for a plastic Kapton® exit foil resulted in $\Delta\theta \leq 0.5^{\circ}$. Therefore, it was determined to replace the usual Havar exit foil with a 1.36 mg cm^{-2} Kapton foil. However, the plastic exit foil stretched under pressure when the gas cell was filled. It was estimated to stretch between 1.5 to 3 mm, more than doubling the effective length of the gas cell, resulting in an angular resolution of $\Delta\theta \approx 1.5^{\circ}$. More significantly, the protons from the

elastic scattering by the hydrogen in the plastic foil gave a very high count rate in the DSSD. There was additional background from the carbon, nitrogen and oxygen in the Kapton, which was first discovered a few days into the run when the gas cell was emptied for a background measurement. The resulting spectra obtained during the empty target run looked identical to the previous runs with the ^{3}He gas. Much effort was made to clean up the spectra. However, due to the combined effects of the 1.5 × 1.5 mm beam spot, the angular uncertainty due to the stretching of the exit foil, and the difficulty separating the recoil nuclei of interest from the background, we were unable to obtain an angular distribution for the ^{19}Ne(^{3}He,d)^{20}Na reaction and, thus, any information about the spin of the 2.645 MeV state.

4.4. Measuring the branching ratio Γ_p/Γ_γ of the 2.645 MeV state in ^{20}Na

4.4.1. Background

For a measurement of the branching ratio Γ_p/Γ_γ the states in ^{20}Na were populated by the charge exchange reaction ^{3}He(^{20}Ne,t)^{20}Na in inverse kinematics. While the previous measurements of the ^{20}Ne(^{3}He,t)^{20}Na reaction in normal kinematics were able to achieve good energy resolution for the levels in ^{20}Na, they were unable to determine the branching ratio or partial widths for the 2.645 MeV state (see Section 4.2.1). The nucleus ^{20}Na* can decay either by γ-ray emission thus remaining ^{20}Na, or it can break up into p + ^{19}Ne. One way to determine the branching ratio of the 2.645 MeV state is to look for tritons in coincidence with γ-rays as attempted by Hofstee et al. [**60**]. In the current work, we set out to identify the ^{20}Na and ^{19}Ne recoil nuclei in coincidence with the tritons. For this purpose, inverse kinematics was essential for producing recoil nuclei with energies

sufficient for A and Z determination. Figure 4.6 shows the relationship between the laboratory angle and energy of the recoiling ^{20}Na nucleus produced via ^{3}He(^{20}Ne,t) and ^{20}Ne(^{3}He,t) reactions at 7.7 MeV per nucleon for comparison.

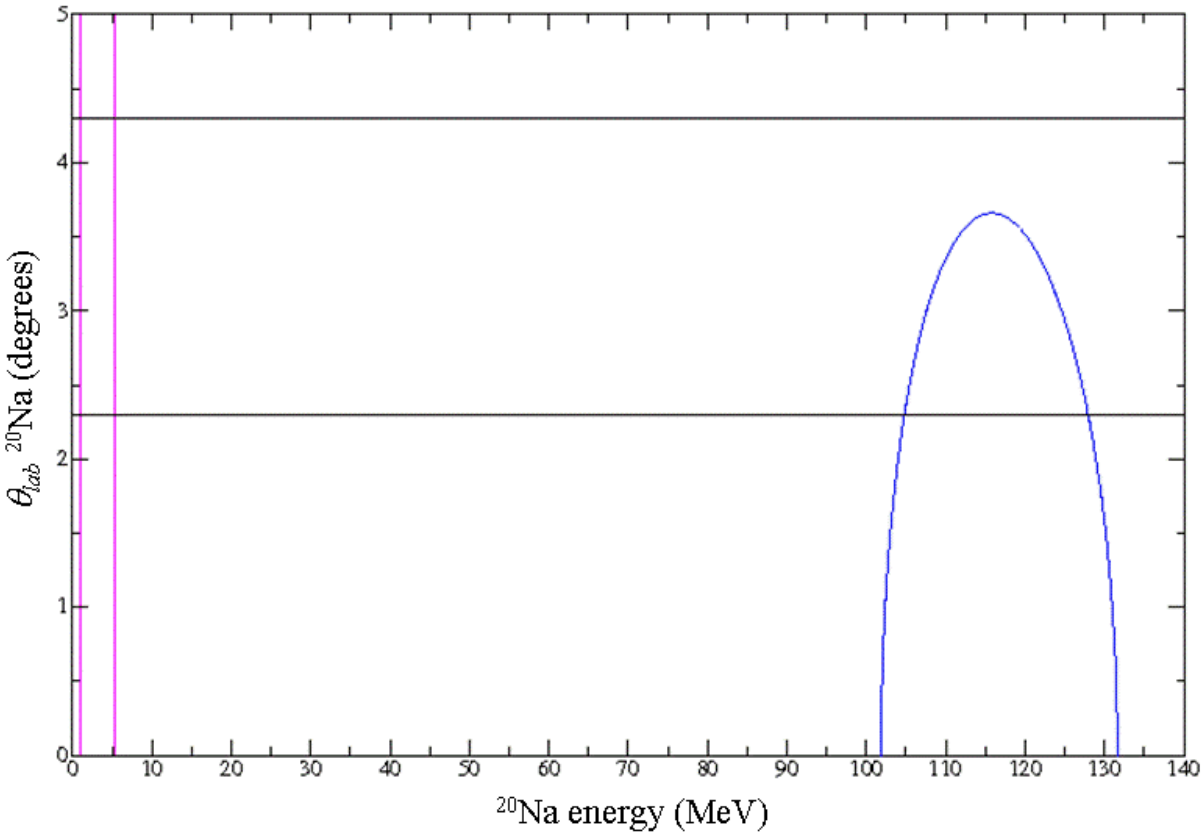

Figure 4.6. Comparison of the kinematics for the ^{20}Ne(^{3}He,t)^{20}Na* (pink) and ^{3}He(^{20}Ne,t)^{20}Na* (blue) reactions populating the 2.645 MeV state in ^{20}Na at 7.7 MeV per nucleon. The black horizontal lines indicate the angular acceptance of the spectrograph.

In normal kinematics (pink) the recoiling ^{20}Na nuclei have energies $E \leq 5$ MeV with an opening angle $\theta_{max} = 25.5°$. Populating the same state via inverse kinematics results in recoil energies $100 \leq E_{lab} \leq 130$ MeV confined to a cone with an opening angle $\theta_{max} = 3.7°$. The higher recoil energies make it possible to detect and identify both the

^{20}Na and the ^{19}Ne using the techniques described in Chapter 2. The ratio of the number of ^{19}Ne ions to the number of ^{20}Na ions in coincidence with a triton feeding a given state provides a measure of the branching ratio Γ_p/Γ_γ. The kinematical-coincidence technique had been used successfully to put a stringent upper limit on the branching ratio Γ_α/Γ in the ^{3}He(^{20}Ne,α)^{19}Ne* experiment discussed in Section 3.3. For states in the region just above the proton threshold $\Gamma = \Gamma_p + \Gamma_\gamma$. Here $\Gamma_p = \Gamma_{p0} + \Gamma_{p1} + \Gamma_{p2}$, where p_i represents transitions to the $1/2^+$ ground state, the $5/2^+$ 238 keV state, and the $1/2^-$ 275 keV state in ^{19}Ne, respectively. Similarly, Γ_γ includes transitions to all the bound states of ^{20}Na. However, because we did not measure the protons or γ-rays, the ratio of the total number of ^{19}Ne to ^{20}Na in coincidence with a triton, gives the ratio of the total widths of each channel Γ_p/Γ_γ. For the $J^\pi = 1^+$ assignment, the partial widths for decay to the excited states in ^{19}Ne are negligible. However, this is not the case for the $J^\pi = 3^+$ assignment where there could be significant branching to ^{19}Ne excited states (see Table 5.1 and the accompanying discussion).

4.4.2. Experimental details

A 160 MeV ^{20}Ne beam was incident on the 1.5 mm long gas cell target filled with ^{3}He at a pressure of 700 mbar. The beam current varied between 0.03 and 0.175 pnA or (2 – 10) $\times 10^8$ ^{20}Ne s^{-1}. The ^{3}He gas was contained by 1.9 mg cm^{-2} Havar® foils and cooled to LN_2 temperatures, resulting in an overall ^{3}He thickness of around 40 μg cm^{-2}. The same detector setup (shown in Figure 2.3) and target were used as for the ^{3}He(^{20}Ne,α)^{19}Ne* experiment. A 500 μm thick square DSSD (described in Section 2.3.2) was positioned to cover triton angles from $19 \leq \theta_{lab} \leq 29°$. The incident ^{20}Ne ions lost about 6 MeV

in the entrance foil resulting in 154 MeV ^{20}Ne on target. At this incident beam energy, states populated above 2.0 MeV in ^{20}Na produce tritons with a maximum opening angle of around 28° and energies $5.5 \leq E_{lab} \leq 30$ MeV at the angles covered by the DSSD. Kinematic curves of triton angle vs. energy for the 2.057, 2.645 and 2.849 MeV states in ^{20}Na are shown in Figure 4.7.

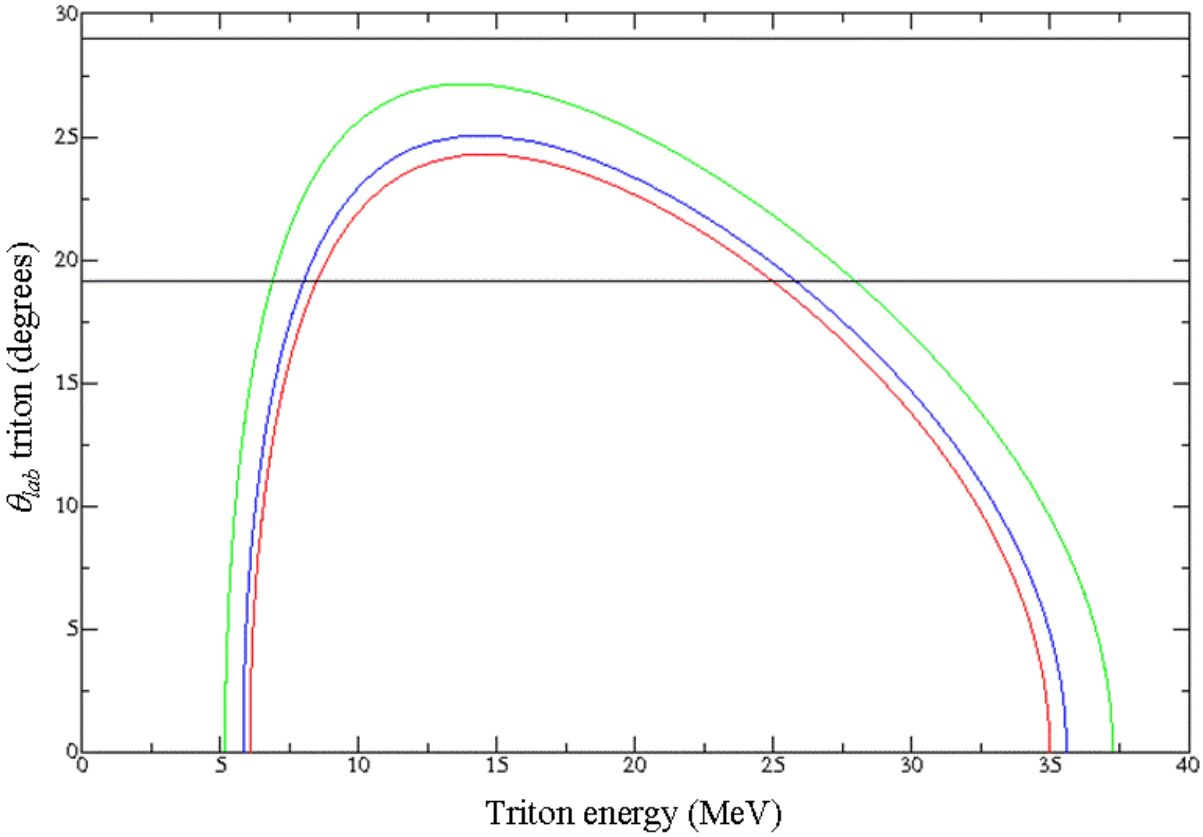

Figure 4.7. Kinematic curves of laboratory angle vs. energy for tritons populating the 2.057 (green), 2.645 (blue), and 2.849 (red) MeV states in ^{20}Na for ^{3}He(^{20}Ne,t)^{20}Na* reaction at 154 MeV. The DSSD covers angles between $19 \leq \theta_{lab} \leq 29°$ (black).

A 21 mg cm^{-2} Mylar® absorber foil was placed in front of the DSSD to stop the elastically scattered ^{20}Ne beam particles. The Enge split-pole magnetic spectrograph (SPS) was

used to detect the recoil nuclei and was positioned to cover angles from $2.3 \leq \theta_{SPS} \leq 4.3°$. The magnetic field was set to cover 95 – 135 MeV Ne and Na ions. Figure 4.8 shows the angular coverage for ^{20}Na-t coincidence detection of the ^{3}He(^{20}Ne,t)^{20}Na* reaction at 154 MeV for states at 2.057, 2.645, and 2.849 MeV.

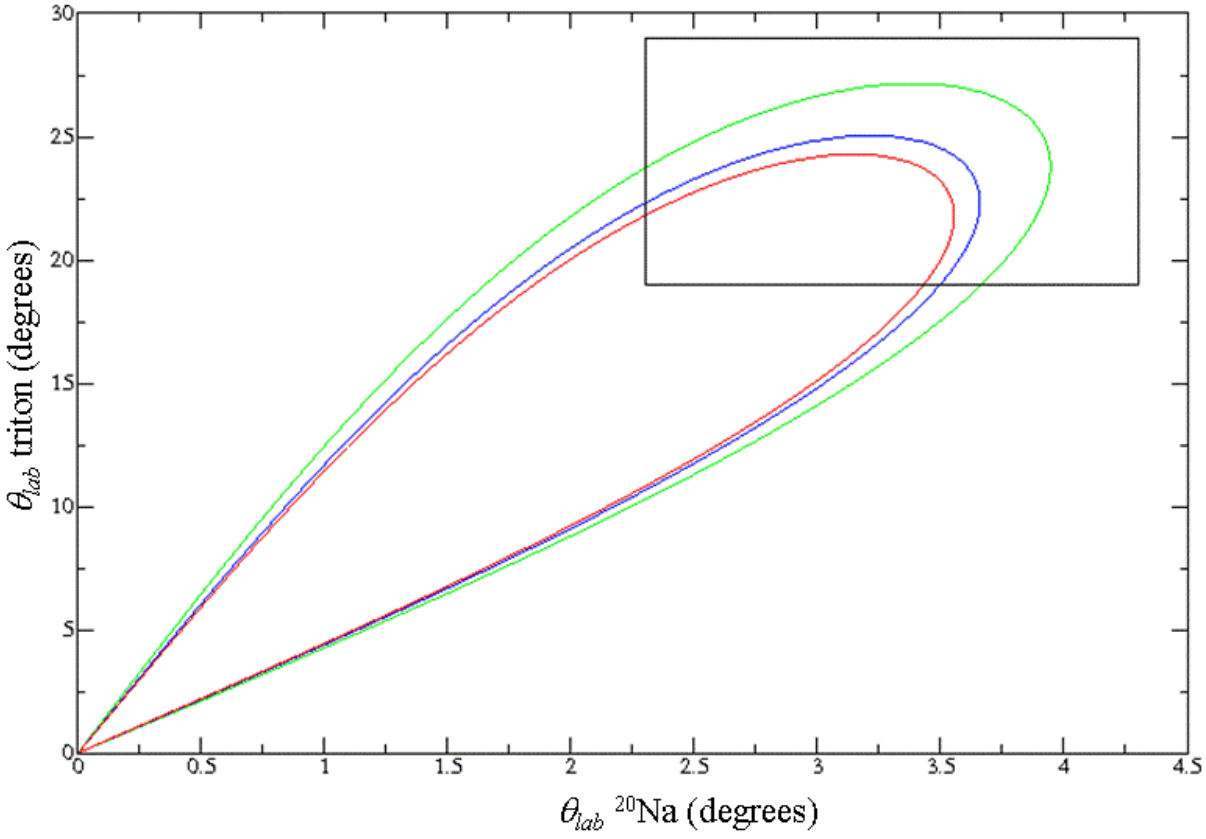

Figure 4.8. Triton angle vs. ^{20}Na angle for the ^{3}He(^{20}Ne,t)^{20}Na* reaction at E_{lab} = 154 MeV. Kinematic curves are shown for the 2.057 (green), 2.645 (blue) and 2.849 (red) MeV states in ^{20}Na. The angular coverage of the DSSD (y-axis) and the spectrograph (x-axis) is shown by the black box.

4.4.3. Data Analysis

The electronics used for this experiment have been described in Section 2.3.2 and shown as a block diagram in Figure 2.4. The parameters are summarized in Table 4.1.

Table 4.1. Summary of the relevant parameters used for particle identification and data analysis.

Parameter	**Description**
E	Total integrated charge under the Bragg curve measured in the IC/BCD
Z	Height of the Bragg peak measured in the IC/BCD
RANGE	Electron drift time through the ionization chamber determined from the TAC between the PPAC and the IC anode and is proportional to $(dE/dx)^{-1}$
POSPP	Focal plane position derived from the time difference between the PPAC wire grid signals *HEPO*, *HEPI*, *LEPO*, and *LEPI*
TSI	Coincidence time between the spectrograph PPAC and the DSSD
ESI	Calibrated energy signal from the front (*EF*) and back (*EB*) of the DSSD

A logical OR between the DSSD and the spectrograph PPAC was used as the event trigger for all signals to be read out and written to tape. The data acquisition program DAPHNE [**84**] provided the interface between the CAMAC ADC signals and the VAX-α computer used for data storage and on-line analysis. The data from each of the output signals shown in Figure 2.4 were sorted and binned into histograms. A broad window placed on the one-dimensional coincidence time spectrum *TSI* was applied as a gating condition to eliminate the large number of singles events. Additional software gates required that both the front and the back of the DSSD produced a signal, *EF* and *EB*,

respectively, and that these energy signals be the same. The logical AND of these conditions together with the *TSI* window comprised the preliminary conditions applied to the two-dimensional spectra used for particle identification.

To identify the heavy ion species the particles were first sorted by their nuclear charge Z. Two-dimensional histograms of $RANGE$ vs. E^2 (Figure 4.9) and Z vs. E (Figure 4.10) were used to separate the Na (Z = 11) from the Ne (Z = 10) groups as described in Section 2.3.2.

The Na and Ne groups were better separated in the $RANGE$ vs. E^2 spectrum; therefore, these windows were used as the primary Z gate for ion species identification. The Z vs. energy windows were used to help clean up the spectra. The windows from these two spectra were then applied as conditions on the two-dimensional spectrum of Energy vs. focal plane position ($POSPP$) to identify the respective isotopes. The focal plane position is proportional to the particles magnetic rigidity, $B\rho$, as discussed in Section 2.3, providing separation by their mass and atomic charge state squared when plotted against the energy signal. Figure 4.11 shows the E vs. POSPP spectrum before applying the Z gates.

Applying the Z gates to this spectrum reveals the different charge state groups for Na and Ne. Windows are drawn around the two charge states of ^{20}Na (Figure 4.12) and ^{19}Ne (Figure 4.13).

The dominant groups in Figure 4.12 are ^{21}Na from the ^{3}He(^{20}Ne,d) reaction. The high-energy tail of the $^{21}Na^{10+}$ group extends beyond the edge of the focal plane, which cuts off around channel 215. Leakage from the tails of the neighboring Ne Z gates (see

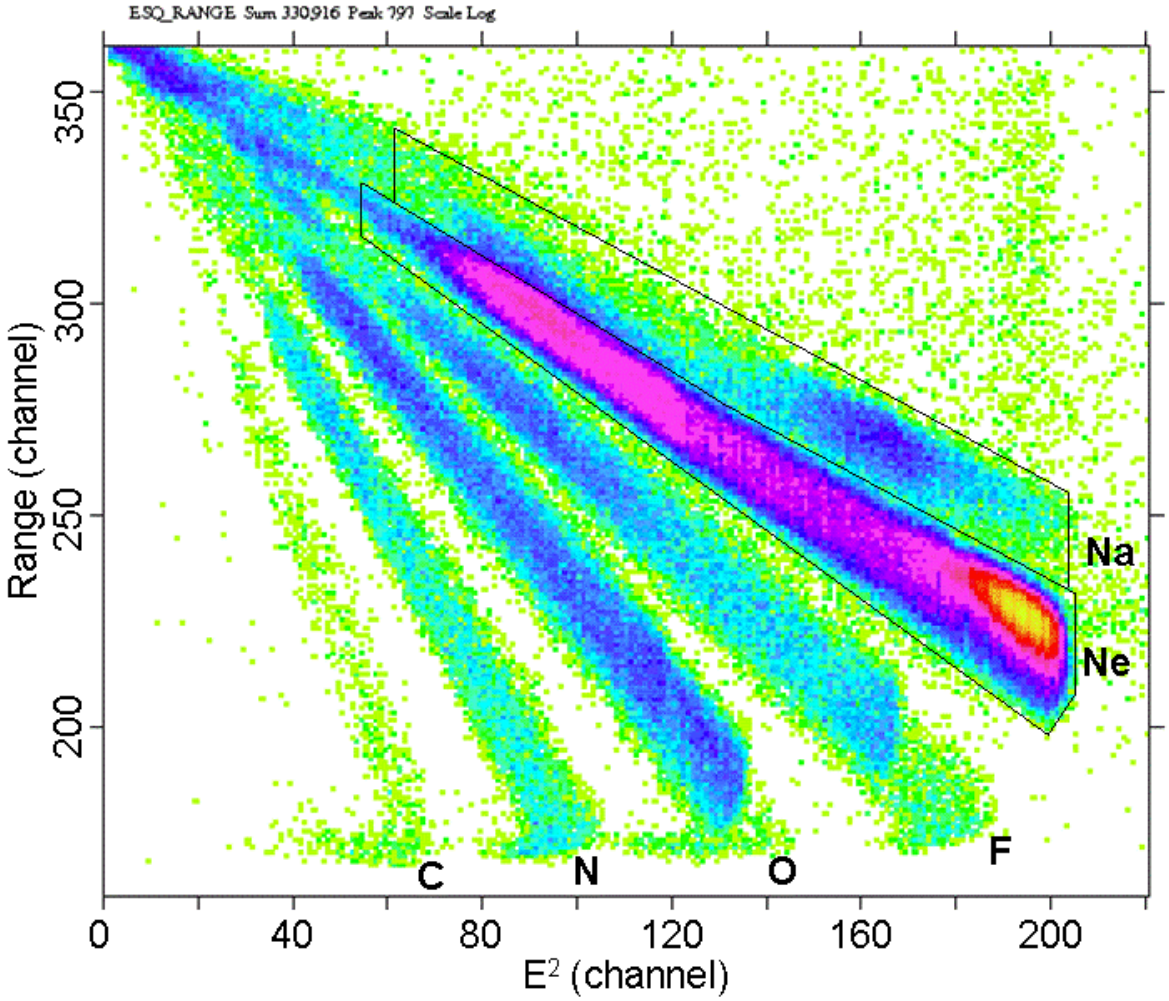

Figure 4.9. Range vs. E^2 spectrum with the preliminary gating conditions applied. The various ion species are indicated and windows are drawn around the Na and the Ne groups.

Figure 4.13 and Figure 4.14) can be seen just above the 10^+ charge states of Na. However, the 11^+ charge states of Na are well isolated from the Ne background.

The dominant groups in Figure 4.13 are ^{20}Ne from the scattered beam, flanked by ^{19}Ne (above) and ^{21}Ne (below), respectively for each charge state. ^{21}Ne can be produced via 2-p evaporation of the compound nucleus ^{23}Mg. The groups to the left of ^{19}Ne are

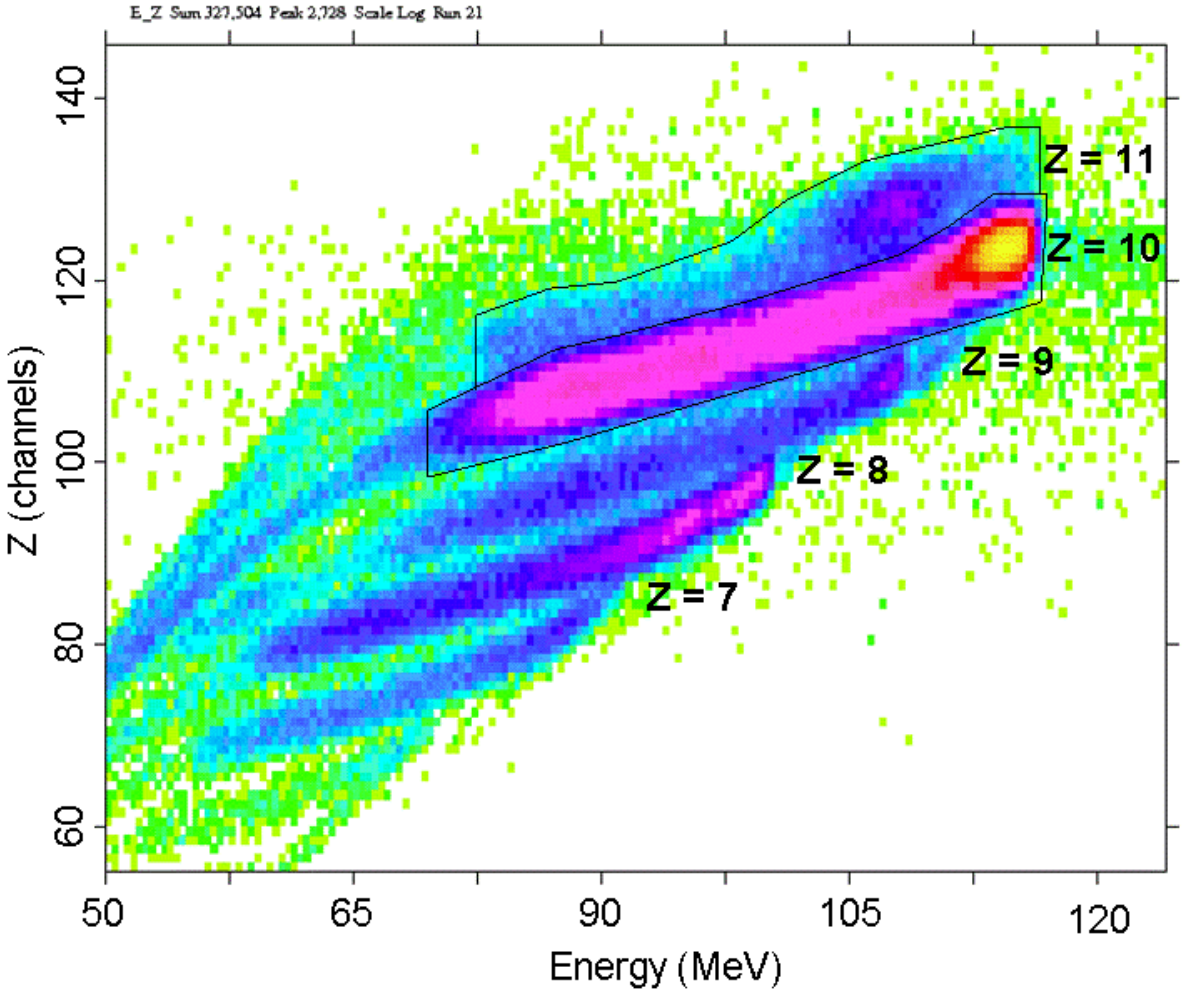

Figure 4.10. Nuclear charge Z vs. energy spectrum with the same gating conditions applied. The Z groups are indicated and windows are drawn around the Z = 11 and Z = 10 groups.

most likely due to leakage from the low-energy tails of the neighboring Na Z gates (see Figures 4.9 and 4.10).[a] The windows in Figures 4.12 and 4.13 were used to define the final particle identification condition and were combined as a logical AND with the Z gates, the coincidence time, and the DSSD conditions described previously.

[a]Some of these events can also be $^{18}Ne^{10+}$ and $^{17}Ne^{10+}$, due to the breakup of the compound nucleus $^{23}Mg^{*}$ into ^{18}Ne α + n and ^{17}Ne + α + 2n, respectively.

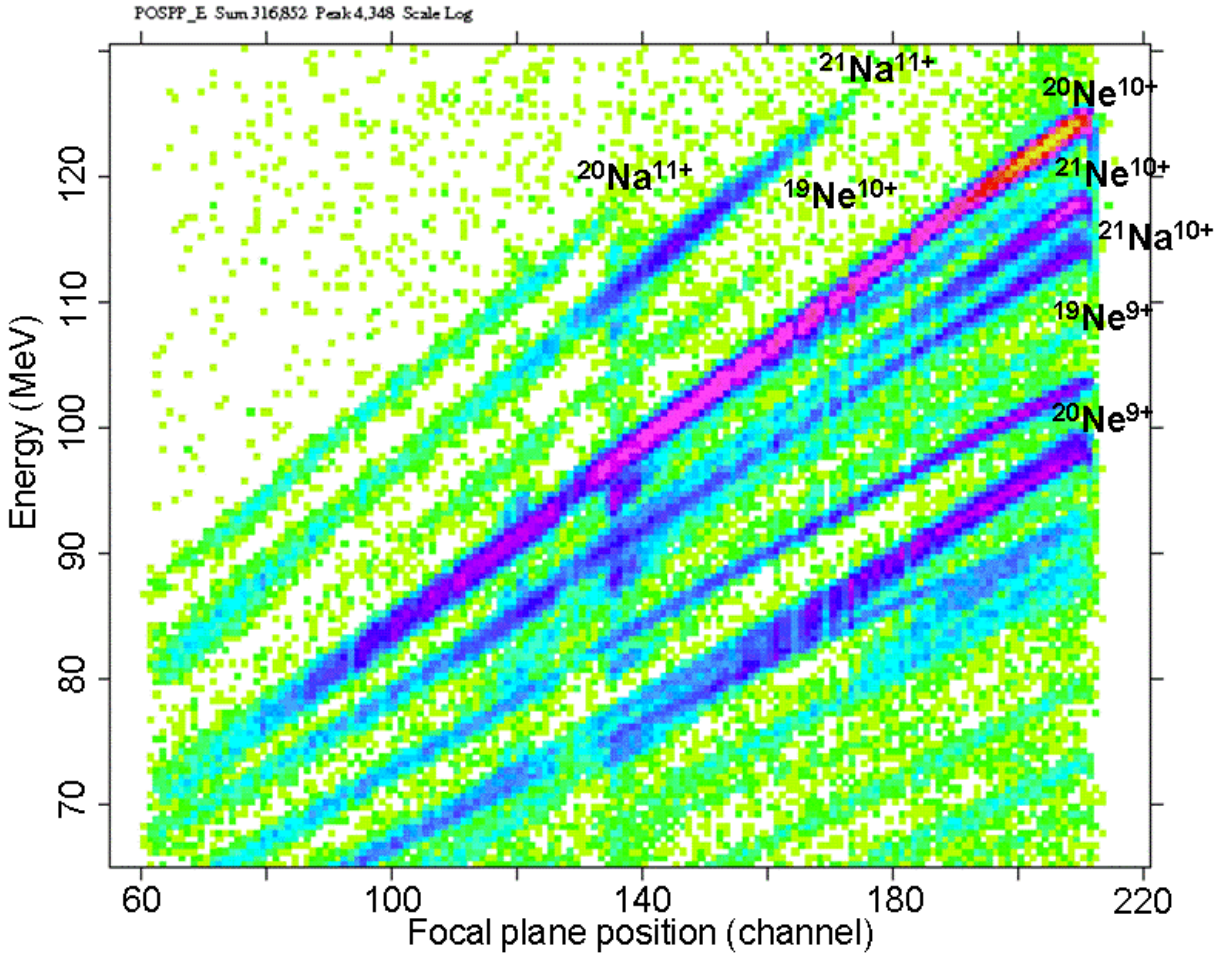

Figure 4.11. Energy vs. position spectrum without the Z gates applied. Ion species are separated by their momentum and the square of their charge state. The dominant group is $^{20}Ne^{10+}$ due to the scattered beam.

The DSSD was not thick enough to stop tritons with energies greater than 12 MeV, which resulted in a partial energy signal[b]. Therefore, an additional gate was required to determine if the particle stopped in the detector. A two-dimensional spectrum of the recoil energy measured in the spectrograph ionization chamber versus the triton energy measured in the DSSD is shown in Figure 4.14.

[b]Particles that do not stop in a detector are sometimes referred to as "punch-throughs."

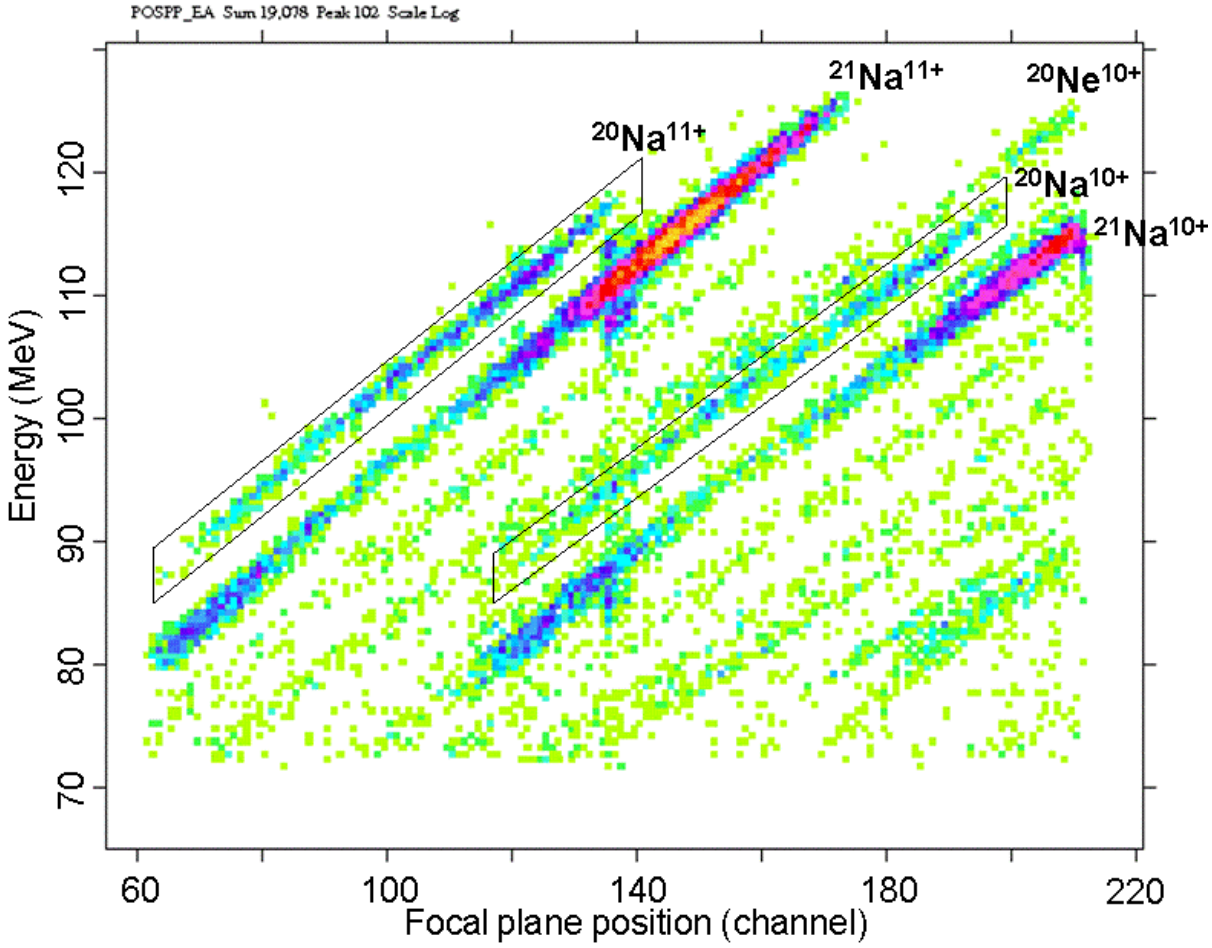

Figure 4.12. Energy vs. position spectra with the Na Z gates applied. The relevant groups are labeled and windows are drawn around the two charge states of ^{20}Na.

The spectrum in Figure 4.14 has been gated for ^{20}Na-t coincidences, which includes the coincidence time, the DSSD conditions, the Na Z gates and the ^{20}Na m/q gates. The turning point where the tritons punch through the detector is indicated by the wedge-shaped window at the right. A spectrum was also generated for ^{19}Ne-t coincidence and similar windows were drawn. The stopped triton windows were used as a final gating condition and used to calculate the Q-value.

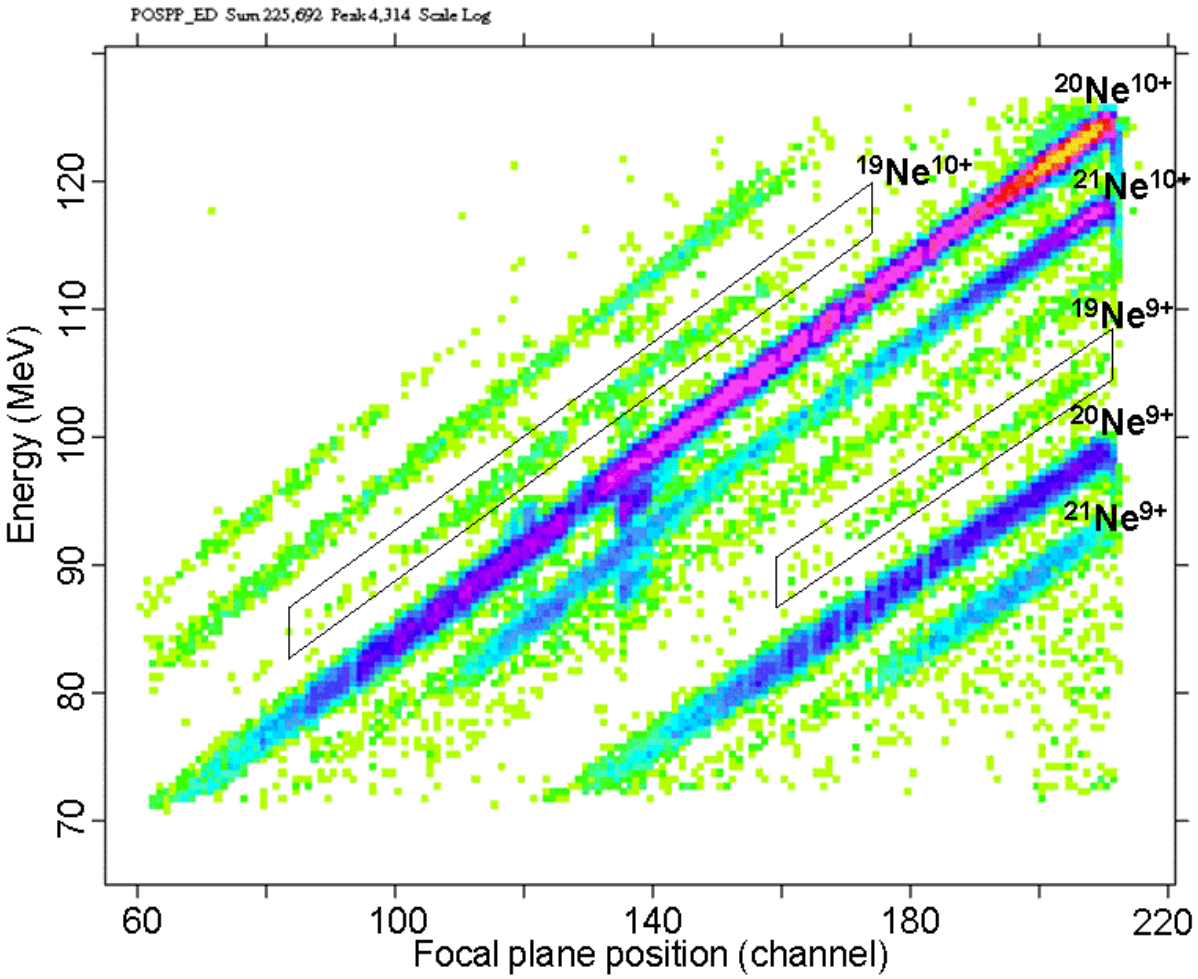

Figure 4.13. Energy vs. position spectra with the Ne Z gates applied. Windows are drawn around the two charge states of ^{19}Ne.

A Q-value spectrum was generated from the energy and angle of the ejectile provided by the DSSD[c]. For a reaction of the form 1(2,3)4, where 1 is the target, 2 is the incident beam, 3 and 4 are the reaction products, the reaction Q-value is given by

$$Q = T_3\left(1+\frac{m_3}{m_4}\right) - T_2\left(1-\frac{m_2}{m_4}\right) - 2\sqrt{\frac{m_2 m_3 T_2 T_3}{m_4^2}}\cos(\theta_3) \tag{4.3}$$

[c]This equation is also valid when the ^{20}Na breaks up in ^{19}Ne + p because we only use the measured energy and position of the triton, which is fully determined by 2-body reaction kinematics. The Q-value then represents the excitation energy in ^{20}Na before it decays by proton or gamma ray emission.

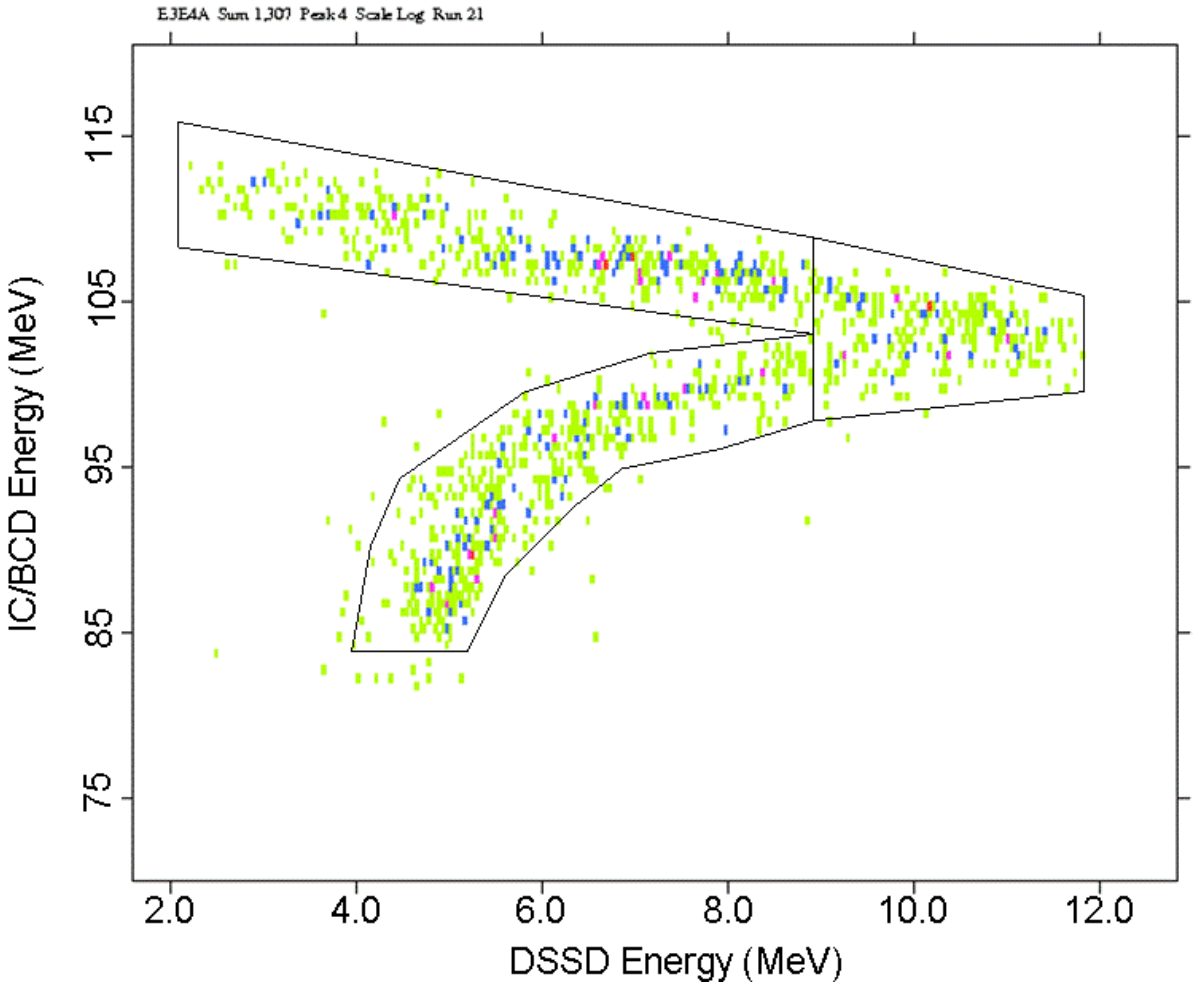

Figure 4.14. IC/BCD (^{20}Na) energy vs. DSSD (triton) energy spectrum gated for ^{20}Na-t coincidences. The windows indicate three regions that were used to separate the tritons that stopped in the DSSD as described in the text.

Where T_i is the kinetic energy and m_i the mass of particle i, and θ_3 is the angle of particle 3 relative to the beam direction. The beam energy (T_2) was taken at the center of the gas target and the scattering angles θ_3 were calculated from the XY-pixel position on the DSSD. The triton energy (T_3) was measured in the DSSD and corrected for the energy lost

by the tritons in passing through the Havar and the Mylar foils using the code ENELOSS [**85**].

The Q-value resolution depends on both the angular resolution and the energy resolution. The angular resolution depends on the geometry of the experiment, the size of the DSSD pixels (1 mm^2), the diameter and position of the beam spot, and on the location within the gas cell where the reaction takes place. In this case, the beam spot diameter (3 mm) and the length of the gas cell ($\approx$ 1.5 mm) are the dominant source of the angular uncertainty. Adding these together in quadrature gives an overall angular uncertainty $\Delta\theta = 0.84°$. Contributions to the energy resolution come from the uncertainty of the beam energy and from the uncertainty in the energy of the outgoing tritons. The uncertainty in the beam energy is due to the energy straggling in the entrance foil, 120 keV, the energy straggling in the gas cell, 20 keV, and the uncertainty due to the energy loss in the ^{3}He gas, 150 keV. Adding these in quadrature gives $\Delta E = 193$ keV. For a triton with 11 MeV emitted towards the center of the DSSD at $\theta = 24°$, the uncertainty in energy comes from the intrinsic energy resolution of the silicon detector and electronics, 50 keV, and the energy and angular straggling of the tritons through the Havar exit foil and the Mylar absorber foil, 5 and 40 keV, respectively. The energy lost by the tritons on the ^{3}He gas is negligible. Adding these in quadrature gives 64 keV, for a total energy resolution of about 203 keV, in reasonable agreement with the observed Q-value resolution (see Figures 4.15 – 4.17). This simple estimate gives the average energy resolution in the Q-value spectrum near the center of the DSSD. The Q-value resolution is slightly better at smaller angles and higher energies and slightly worse at larger angles and lower energies[d]. The overall

[d]Additionally, some of the quantities here are strongly correlated; therefore, calculations that are more detailed should be made which include the full range of triton energies and angles.

Q-value resolution depends very much on the reaction kinematics. The kinematic curves for tritons populating the 2.057, 2.645, and 2.849 MeV states in Figure 4.7 (above) shows the effect of the relationship between angle and energy. It is clear from the figure that the best way to separate closely spaced states is to measure them near the maximum triton angle (top of the curves) for each state. This portion of the kinematic curves for the 2.645 and 2.849 MeV states occurs near the central angle of the detector by design of the experiment. At 24° the energy changes with angle by $dE/d\theta \approx 1.3$ MeV, while at 22°, $dE/d\theta \approx 600$ keV. Hence, these two states that are only 200 keV apart in excitation energy, are separated by 600 keV near 22° and by 1.3 MeV near 24° on the low energy side of the curve. Figure 4.15 shows the resulting Q-value spectrum generated after gating with the appropriate conditions for ^{20}Na-t coincidences and the stopped tritons.

The Q-value spectrum exhibits a large peak near excitation energy $E_x = 1.9$ MeV in ^{20}Na that contains contributions from three closely spaced states indicated in the figure. The weighted mean energy of these states $\langle E \rangle = 1.94$ MeV and the well-resolved 1.346 MeV state was used to calibrate the energy scale. The states were identified by comparing our Q-value spectrum with the previous ^{20}Ne(^{3}He,t)^{20}Na experiments discussed in Section 4.2.1. As expected, very few counts appear to the left of the proton threshold at 2.195 MeV. Figure 4.16 shows the same spectrum gated for ^{19}Ne-t coincidence events.

In Figure 4.16, most of the counts appear above the proton threshold, as expected. However, some counts appear in the "forbidden" region below threshold. These events are due to protons from the breakup of ^{20}Na* into ^{19}Ne + p and are discussed below in more detail. Figure 4.17 combines these two spectra to give the complete ^{20}Na excitation energy spectrum for the states below 3.5 MeV.

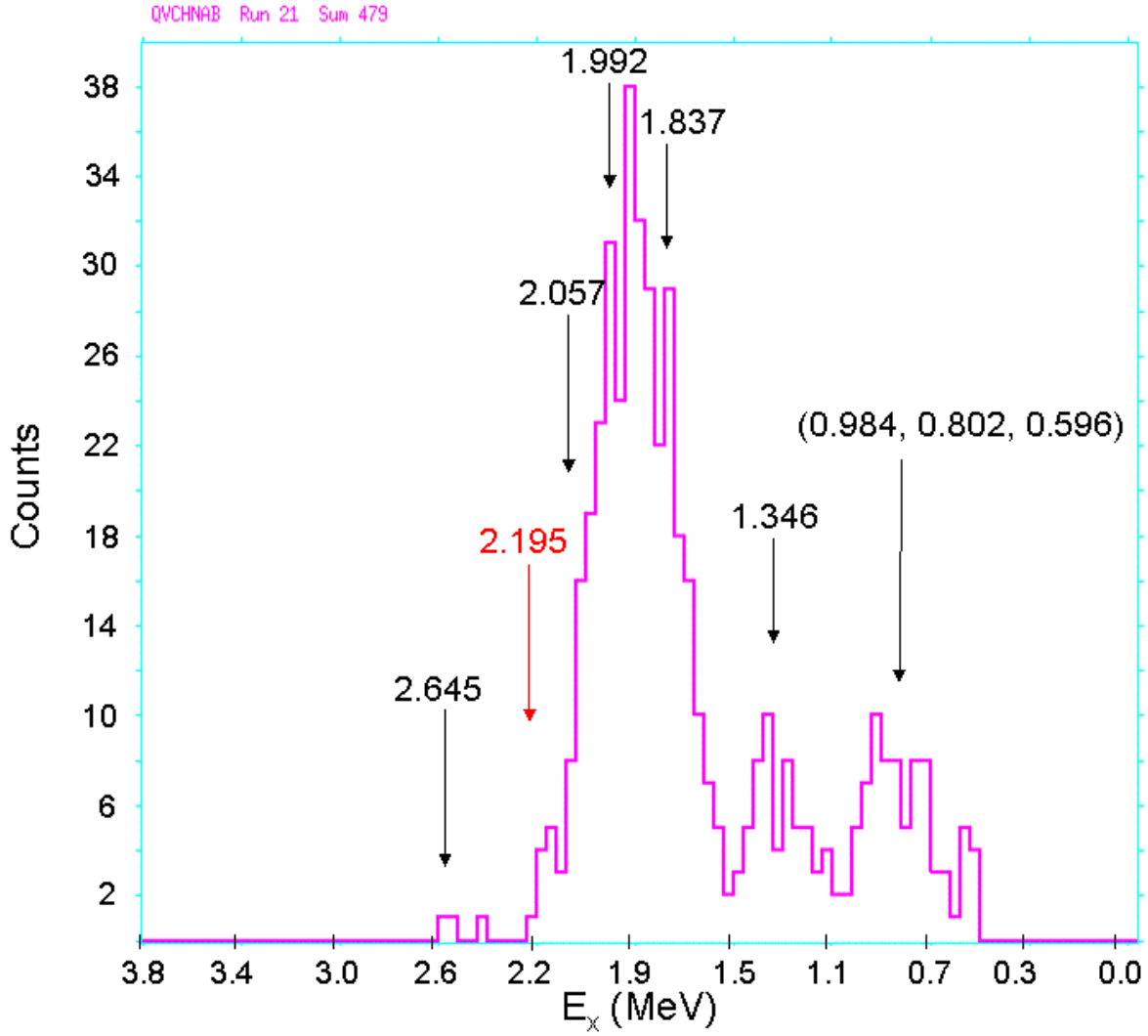

Figure 4.15. Q-value spectrum for ^{20}Na-t coincidence events. The known states (black) and the proton threshold (red) are indicated.

The ground state was not observed. At the angles covered in this work, tritons populating the ground state in ^{20}Na have energies that are either too low, $E_t < 6$ MeV, to pass through the Mylar absorber foil, or too high, $E_t > 15$ MeV to stop in the DSSD. The triton energy spectrum measured for the ^{20}Ne(^{3}He,t)^{20}Na reaction at $E_{beam} = 33.4$ MeV by Clarke et al.[**12**] is shown in Figure 4.18 for comparison

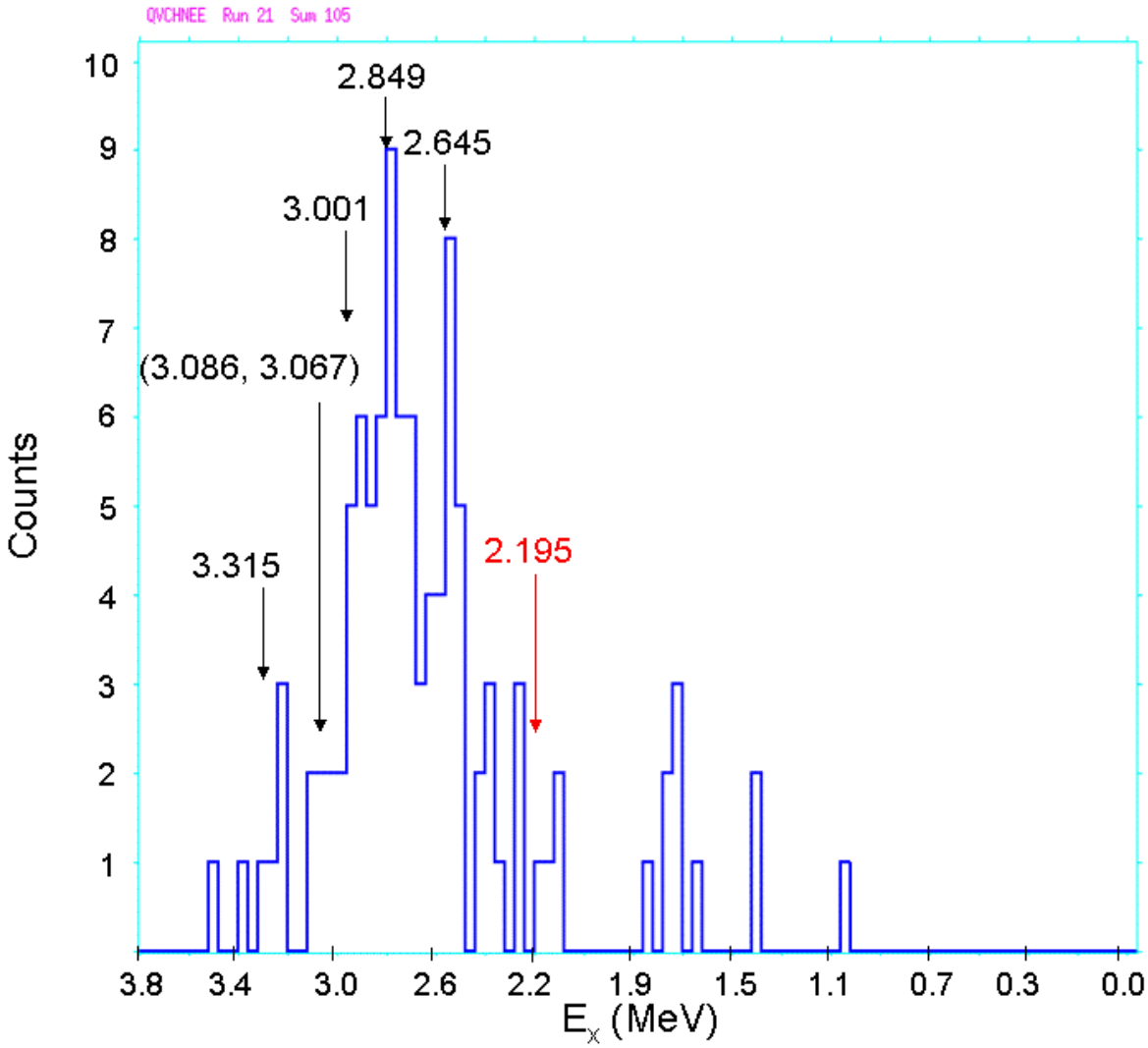

Figure 4.16. Q-value spectrum for ^{19}Ne-t coincidences.

The resolution achieved by Clarke et al. was very much better and the reasons for the width of the peaks in the present experiment are discussed in detail above. While some of the effects may be unique to the present work the rapid variation of reaction product energy with angle is inherent in inverse kinematics and means that even reasonably good angular resolution can lead to poor Q-value resolution. However, we were able to observe

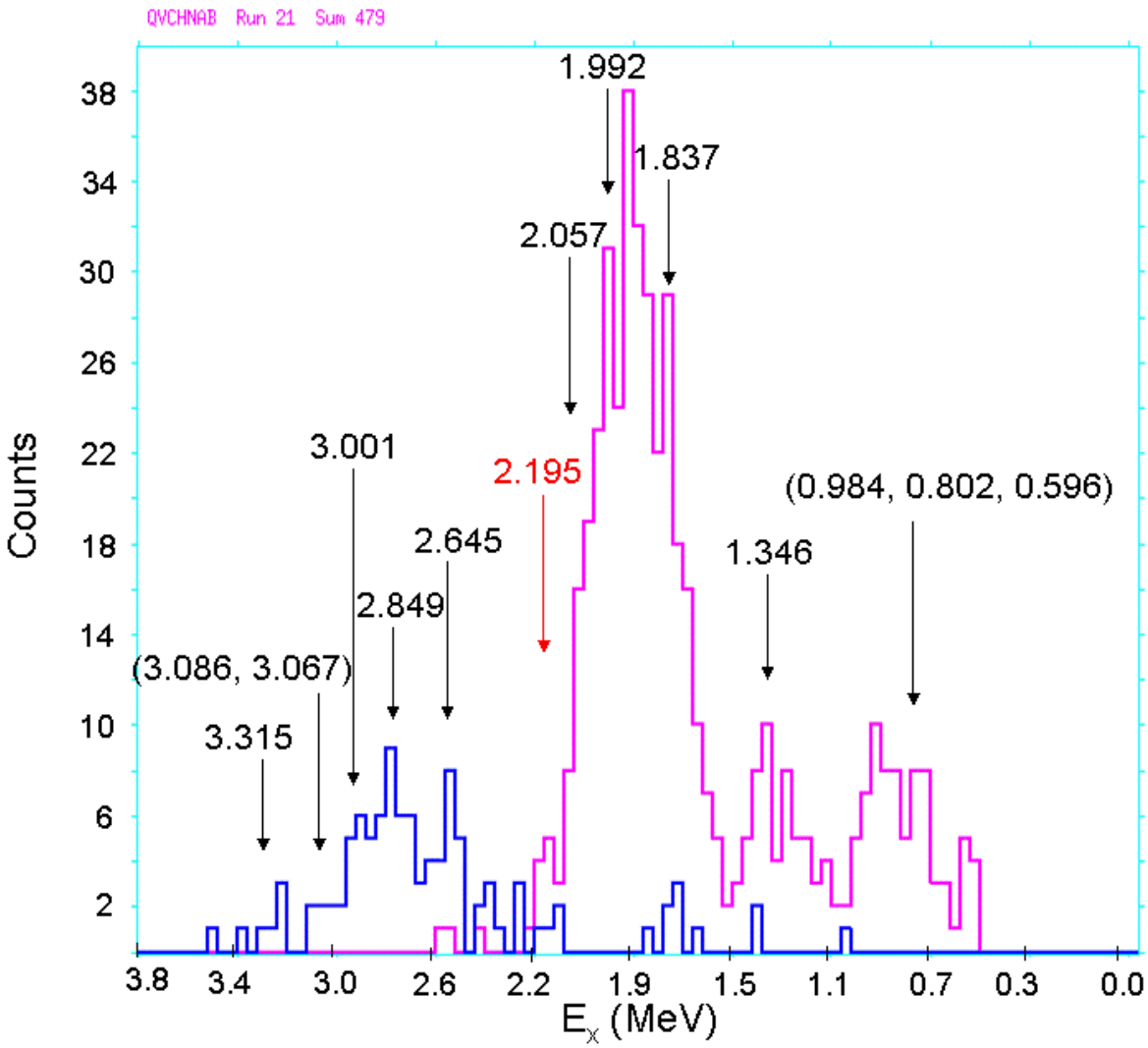

Figure 4.17. The composite Q-value spectrum for ^{20}Na showing excitation energies below 3.5 MeV obtained from ^{20}Na-t (pink) and ^{19}Ne-t (blue) coincidences.

how the states decayed which Clarke et al. and the others using normal kinematics could not do. The energy region of the Q-value spectrum of Figure 4.17 is indicated by the vertical red bars in Figure 4.18. The 2.645 and 2.849 MeV states of interest in this work are labeled as peak numbers 8 and 9, respectively, in Figure 4.18. Both spectra

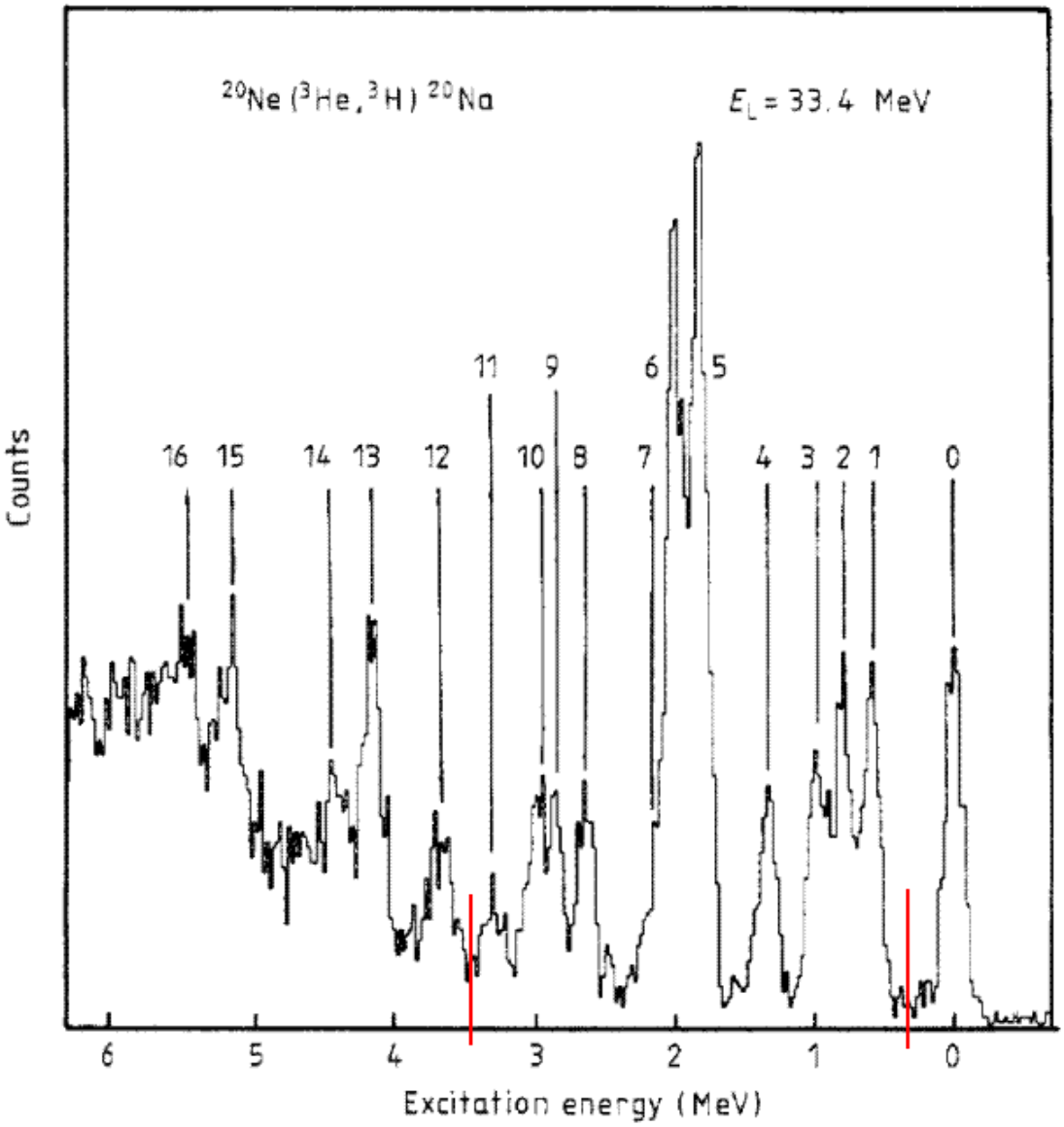

Figure 4.18. Triton energy spectrum taken from Ref [**12**] is shown here for comparison. The energy region covered in the current work is indicated by the vertical red bars (states 1– 11). (Courtesy of Nobby Clarke)

(Figures 4.17 and 4.18) show a large peak near 2.0 MeV corresponding to two strongly-fed states at 1.847 and 1.992 MeV, labeled 5 and 6, respectively, and a relatively weak state at 2.057 MeV (labeled 7). Peak number 4 in Figure 4.18 corresponds to the 1.346

MeV state in Figure 4.17. These two groups were used to calibrate the Q-value spectrum in Figure 4.17 in the following way: ^{20}Na-t and ^{19}Ne-t coincidence events for tritons that were stopped in the DSSD were plotted with the kinematic curves for the known energy levels $\leq$ 3.0 MeV for the angular coverage of the DSSD (Figure 4.19).

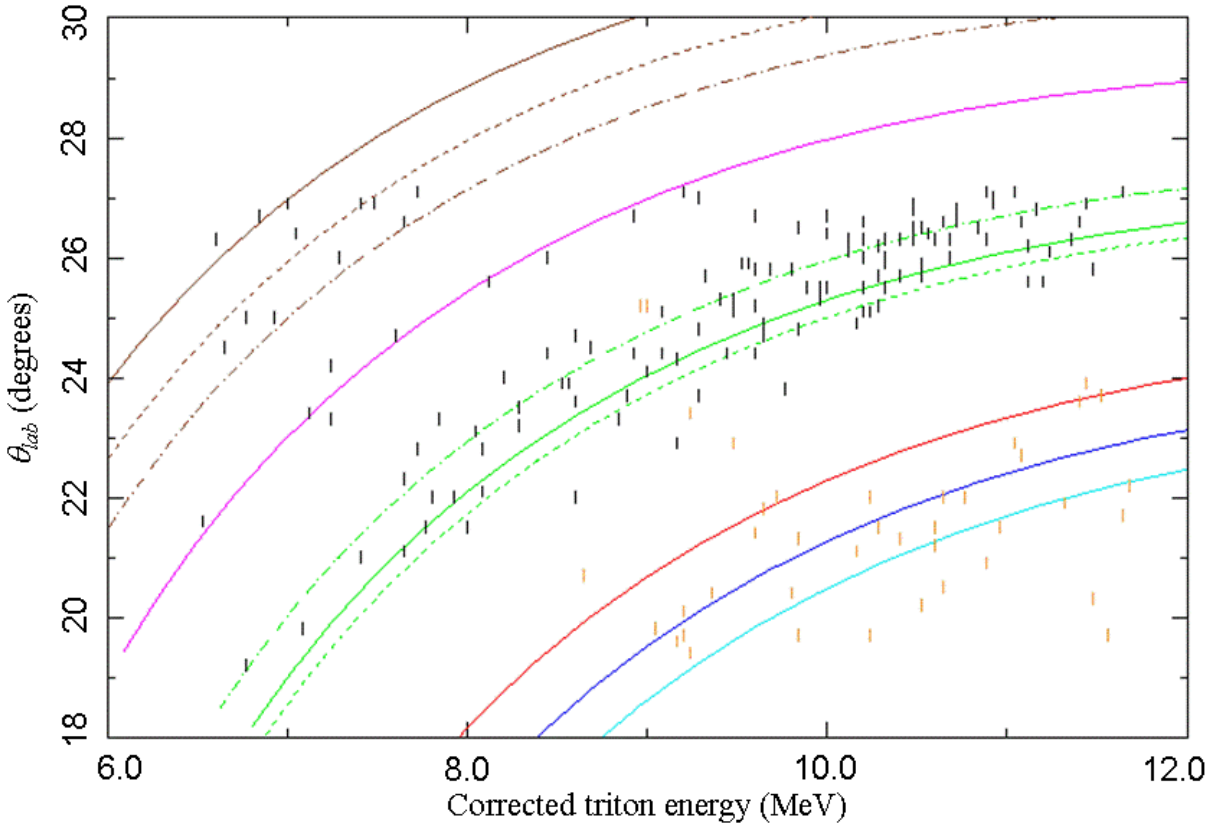

Figure 4.19. Kinematic curves for tritons produced via the ^{3}He(^{20}Ne,t)^{20}Na reaction at 154 MeV. States between 0.5 and 3.0 MeV in ^{20}Na are shown for the angular and energy range covered by the DSSD. The data are shown with the corrected triton energies in coincidence events with ^{20}Na (black) and ^{19}Ne (orange).

From the upper left to the lower right of the figure, curves are shown for 600, 800, and 984 keV (brown), 1.346 MeV (pink), the 1.847, 1.992, and 2.057 MeV triplet (green),

followed by the 2.645 (red), 2.849 (blue), and 3.001 MeV (cyan) states. The energy-corrected data shown in Figure 4.19 were restricted to the middle ten horizontal strips of the DSSD to minimize the angular spread due to the pixel size.

As expected, very few ^{20}Na-t coincidence counts appear to the left of the large peak in the region above the proton threshold at 2.195 MeV of the Q-value spectrum (Figure 4.19). Conversely, when gating on ^{19}Ne-t coincidences, very few counts appear below the proton threshold, with most counts coming in groups at 2.645, 2.849 and 3.001 MeV as indicated. The ^{19}Ne-t events (blue) that do appear to the right of the proton threshold in the "forbidden" region below the proton threshold can be understood by considering that the Q-value calculation (Eqn 4.3) assumes that all the particles detected in the silicon detector in coincidence with a ^{20}Na or ^{19}Ne ion in the spectrograph are tritons. For states in ^{20}Na below 3.0 MeV, the opening angle of the protons emitted by the recoiling nucleus is less than 20° with respect to the ^{20}Na trajectory and, therefore, these protons do not reach the DSSD with a ^{19}Ne coincidence in the spectrograph. However, for states in ^{20}Na between 3.0 – 5.5 MeV, which are energetically allowed at this beam energy, the emitted protons have sufficient energies and opening angles to hit the DSSD. These events can mimic "good" ^{19}Ne-t coincidence events with respect to the gating conditions while yielding incorrect Q-values. As a further check, these data were analyzed using the Data Desk 6.1 [**86**] software, which allows one to correlate the data appearing in different histograms on a point-by-point basis. The ^{19}Ne-t events that appear in the "forbidden" region were evenly dispersed throughout the gating windows. Therefore, we were not able to eliminate them by gating with narrower windows.

The assumption of zero background for the ^{20}Na-t coincidences can be justified by a closer inspection of the gated energy vs. focal plane spectra shown in Figures 4.12 and 4.13. The ^{19}Ne and ^{20}Na windows are well separated from the stronger groups of ^{20}Ne and ^{21}Na, with the exception of the ^{20}Na^{10+} group, which has some overlap with the ^{20}Ne^{10+} group. However, no additional counts from the ^{20}Na^{10+} window appear near the interesting 2.645 and 2.849 MeV states in the Q-value spectrum. A further justification for assuming zero background can be seen from observing the effect of the particle identification gates on the Q-value spectrum as shown in Figure 4.20. The upper (black) spectrum requiring only a general coincidence between the DSSD and the spectrograph together with the conditions on the DSSD shows the number of counts steadily increasing with decreasing excitation energies (more positive Q-values). Applying the Ne (dark blue) and Na (purple) Z gates (Figures 4.13 and 4.14) significantly reduces the background in the astrophysically interesting region above the proton threshold at 2.195 MeV. The number of gated Na events is about an order of magnitude smaller than the number of gated Ne events throughout the spectrum, as expected.

The spectra resulting from adding the m/q and the stopped triton gates obtained for ^{20}Na-t (pink) and ^{19}Ne-t (blue) coincidences are shown for reference. The ^{20}Na-t coincidences obtained at 2.645 MeV appear to be the first observation of the γ-decay of this state.

For the "forbidden" ^{19}Ne-t coincidences, the 14 counts in Figure 4.20 to the right of 2.2 MeV cover 35 channels for 0.4 counts per channel. The 2.645 and 2.849 MeV states are 7 channels wide, therefore 2.8 counts per state were subtracted as background for

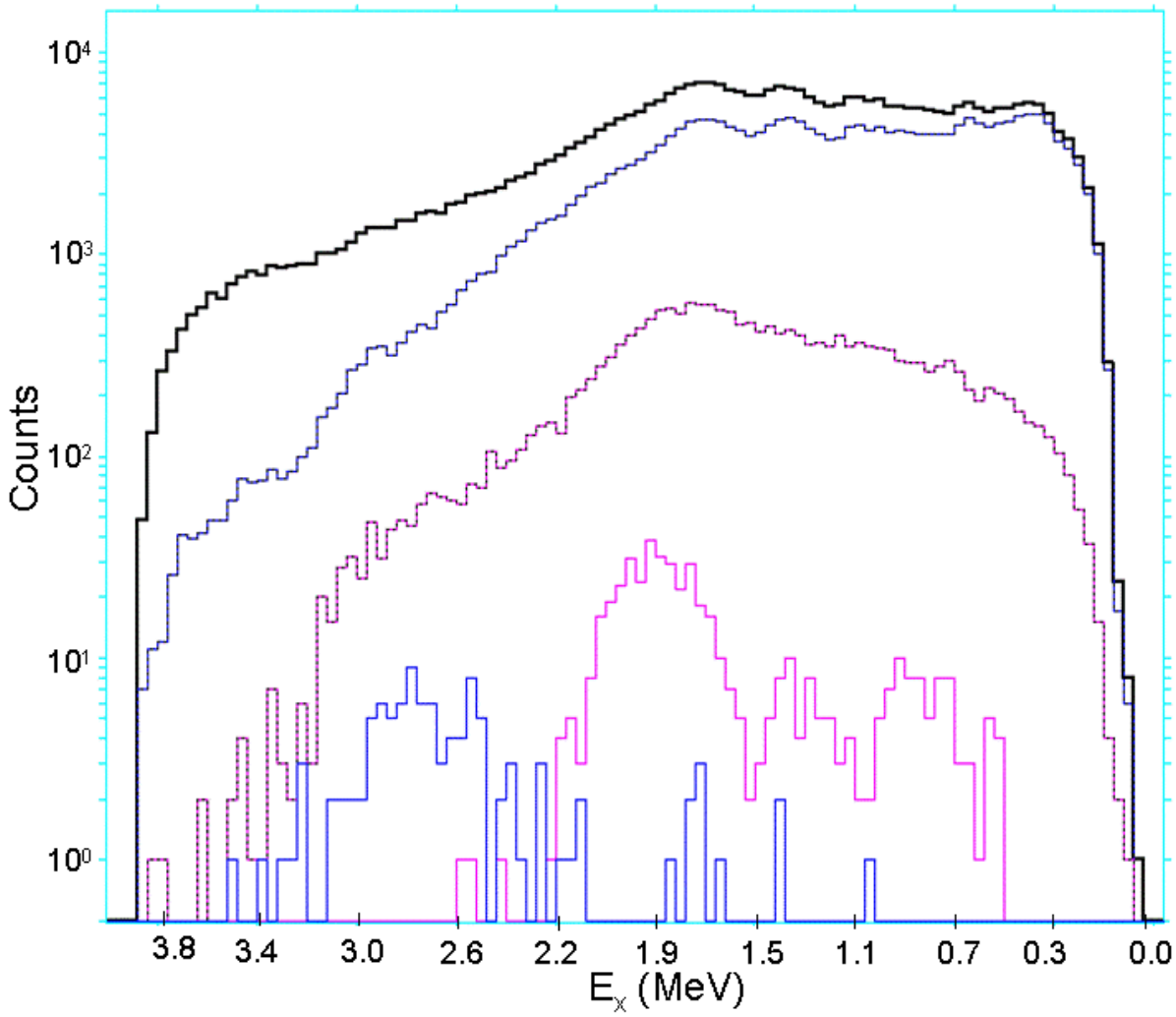

Figure 4.20. Q-value spectrum from Figure 4.17 with some of the gating conditions removed. The upper spectrum (black) includes only coincidence and DSSD conditions. Z gates for Ne (dark blue) and Na (purple) were applied to obtain the next two spectra. The lower Q-value spectra include the additional isotope separation for ^{20}Na (pink) and ^{19}Ne (blue) and the stopped triton condition.

the counts given in Table 4.2. However, based on the previous discussion, this simple background approximation most likely overestimates the background in this region.

4.5. Results

The following results were obtained from the efficiency and background corrected number of counts within the 2.645 and 2.849 MeV peaks in the Q-value spectrum (Figure 4.19). The overall detection efficiency includes the relative efficiency for detecting ^{20}Na-t and ^{19}Ne-t coincidences due to the geometry of the detector setup. Because we detect the tritons in both cases, the intrinsic detection efficiency and solid angle coverage of the DSSD are the same in both cases and cancel when taking the ratio. Therefore, the relative efficiency is determined completely by the relative numbers of ^{20}Na and ^{19}Ne ions detected in the spectrograph. The ^{19}Ne ions produced from the proton decay of ^{20}Na are emitted in the direction of the original ^{20}Na into cones with opening angles that increase with increasing excitation energy. The relative numbers of ^{19}Ne and ^{20}Na that make it into the finite entrance aperture of the spectrograph were calculated using a Monte Carlo simulation that accounts for the reaction kinematics, the detector geometry, and the diameter of the beam spot. Further, some of the ^{19}Ne ions with charge state $q = 9^+$ did not make it to the focal plane of the spectrograph. Therefore, only the counts from the $q = 10^+$ charge state were used. However, for ^{20}Na both the $q = 11^+$ and 10^+ charge states were accessible (compare Figures 4.16 and 4.17). The relative efficiencies for detecting ^{19}Ne and ^{20}Na were also corrected for the focal plane acceptance of the charge state distributions. The efficiency corrected number of counts for both the 2.645 and 2.849 MeV states are given in Table 4.2. Also shown is the ratio of counts N_p/N_γ, which is equivalent to the branching ratio Γ_p/Γ.

We have assumed no background ^{20}Na-t (N_γ) events. For the ^{19}Ne-t (N_p) events, we have extrapolated the small background observed in the "forbidden" region. The upper

Table 4.2. The corrected number of counts in the Q-value coincidence spectra and the resulting branching ratios for the first two states above the proton threshold in ^{20}Na. The upper and lower limits (UL/LL) are shown for 84.13% (1σ), 90% and 95% confidence levels (CL).

$\mathbf{E}_x$ **(MeV)**	$\mathbf{N}_p$	$\mathbf{N}_\gamma$	$\mathbf{N}_p/\mathbf{N}_\gamma$	**UL**	**LL**	**CL (%)**
2.645	31.2	2.06	15.1	43.9	6.28	84.13
				57.9	5.42	90.0
				85.7	4.53	95.0
2.849	48.8	0	∞	∞	26.0	84.13
					20.7	90.0
					15.8	95.0

and lower limits and the confidence limits were calculated from the approximations for Poisson statistics with small numbers of events given by Gehrels [**87**]. For two kinds of distinguishable events, each assumed to be randomly distributed according to Poisson statistics, the distribution of the ratio of the frequency of the two events is determined by binomial statistics. The upper and lower limits on the ratio of the two events are given by equations (19) and (20) of Gehrels.

$$r_{12u} = \frac{p_{1u}}{(1 - p_{1u})} \tag{4.4}$$

$$r_{12l} = \frac{p_{1l}}{(1 - p_{1l})} = \frac{1 - p_{2u}}{p_{2u}} \tag{4.5}$$

Here, r_{12u} and r_{12l} are the upper and lower limits for the ratio of events of type 1 to type 2, and p_{1u} and p_{2u} are the single-sided upper limits for the ratio of type 1 and type 2 events to the total number of events respectively. The quantity p_{1l} can be obtained

from the upper limit p_{2u} by using the same expression as for p_{1u} and switching n_1 and n_2. For the 2.645 MeV state with $N_p = 31.2$ and $N_\gamma = 2.06$, p_{1u} was approximated by the expression

$$p_{1u} \approx \frac{(n_1+1)\,e^{2w} + \varepsilon n_2}{(n_1+1)\,e^{2w} + n_2}\,, \text{ where } \varepsilon = 0.64\,(1-S)\,e^{-n_2} \tag{4.6}$$

Here n_1 and n_2 are the number of events of type 1 (N_p) and type 2 (N_γ) respectively, S is the number of standard deviations, or Gaussian σ. The w that appears in the exponent is a complicated function defined in the Gehrels paper and has been derived from the relationship between the binomial sum and the incomplete beta function ([**87**], page 344, and references therein).

For the 2.849 MeV state, $N_\gamma = 0$ is a special case with an exact expression for the single-sided lower limit given by $p_{1l}\,(n_2 = 0) = (1 - \mathrm{CL})^{1/n_1}$. The lower limit on the ratio r_{12l} was obtained by inserting this expression into Eqn (4.5).

4.6. Summary

The current work reports the first measurement of the branching ratio $\Gamma_p/\Gamma_\gamma = 15.1^{+28.8}_{-8.9}$ (1-σ CL) for the 2.645 MeV in ^{20}Na. For the 2.849 MeV state, a lower limit on the branching ratio $\Gamma_p/\Gamma_\gamma \geq 26.0$ (1-σ CL) was also obtained. The current measurement of the branching ratio of the 2.645 MeV state corresponds to $\Gamma_\gamma/\Gamma \approx 0.06$ in good agreement with the previous estimate of $\Gamma_\gamma/\Gamma \approx 0.1$ [**60**] and with the calculated value for the $J^\pi = 1^+$ assignment in Table 4.2.

CHAPTER 5

Conclusion

5.1. Status of the 2.645 MeV state in ^{20}Na

The branching ratios for the decay of the 2.645 and 2.849 MeV states can now be compared with the predicted values of the ^{19}Ne(p,γ)^{20}Na* resonance parameters in Table 5.1, which has been updated from Table II of Vancraeynest [**9**].

Table 5.1. Comparison of the calculated ^{19}Ne(p,γ)^{20} Na* resonance parameters for the 2.645 and 2.849 MeV states in ^{20}Na for the proposed spin-parity assignments with the experimental branching ratios.

$\mathbf{E}_x$ **(MeV)**	$\mathbf{E}_r$ **(keV)**	$\boldsymbol{J}^{\pi}$	Γ_γ **(meV)**	Γ_{p0} **(eV)**	Γ_{p1} **(eV)**	$\omega\gamma_{calc}$ **(meV)**	$\omega\gamma_{exp}$ **(meV)**	Γ_p/Γ_γ **calc**	Γ_p/Γ^e_γ **exp**
2.645	450	1^+	9.3	.083	$\ll \Gamma_{p0}$	6	≤ 15	8.9[a]	6.3 – 43.9
2.645	450	3^+	81[b]	0.28	0.73	36.4[b]	≤ 15	12.5[b]	6.3 – 43.9
2.849	654	3^+	164	14	387	10		2445[a]	≥ 26.0
2.849	654	3^-	23[c]	0.016	0.275	2		13.5[b*]	≥ 26.0

[a][**58**] Assumes an $\ell = 2$ transition in the calculation of the resonance strength $\omega\gamma$.
[b][**82**] Corrected for the measured lifetime of the 2.966 MeV state in ^{20}F [**11**].
[c][**9**] Deduced from the measured lifetime of the 2.865 MeV state in ^{20}F [**11**]
[e]Current work
[*]includes a small contribution from p2 transitions, Γ_{p2}= 0.0196.

For the 2.645 MeV state, the branching ratios predicted for both $J^{\pi} = 1^+$ and 3^+ spin assignments fall within the experimental limits at the 1-σ level. However, for the 2.849 MeV state the experimental lower limit $\Gamma_p/\Gamma_\gamma \geq 26.0$ is well above the calculated branching ratio $\Gamma_p/\Gamma_\gamma = 13.5$ for the 3^- assignment, but consistent with the calculated branching ratio for$J^{\pi} = 3^+$. The calculated branching ratio for this state predicts that

3 to 4 ^{20}Na-t coincidences should have been observed at this energy but no counts were observed. It is unlikely that the 2.645 and the 2.849 MeV states have the same spin-parity. Therefore, if the spin of the 2.849 MeV state is 3^+, we can infer that the spin of the 2.645 state is more likely $J^\pi = 1^+$.

Taking the most stringent upper limit on the resonance strength of the 2.645 MeV state, $\omega\gamma \leq 15$ meV [**70**], together with the present branching ratio result, strengthens the argument for a $J^\pi = 1^+$ 2.645 MeV state and a $J^\pi = 3^+$ 2.849 MeV state. These results are shown graphically in a "semi-exclusion/inclusion" plot of Γ_{p0} vs Γ_γ for each of the two spin assignments for the 2.645 MeV state. The values for Γ_{p0} and Γ_γ allowed by the upper limit on the resonance strength along with their calculated values are shown in Figure 5.1 ($J^\pi = 1^+$) and Figure 5.2 ($J^\pi = 3^+$). An uncertainty factor of 1.7 is assigned to widths calculated from the properties of mirror states as determined by Iliadis et al. [**88**].

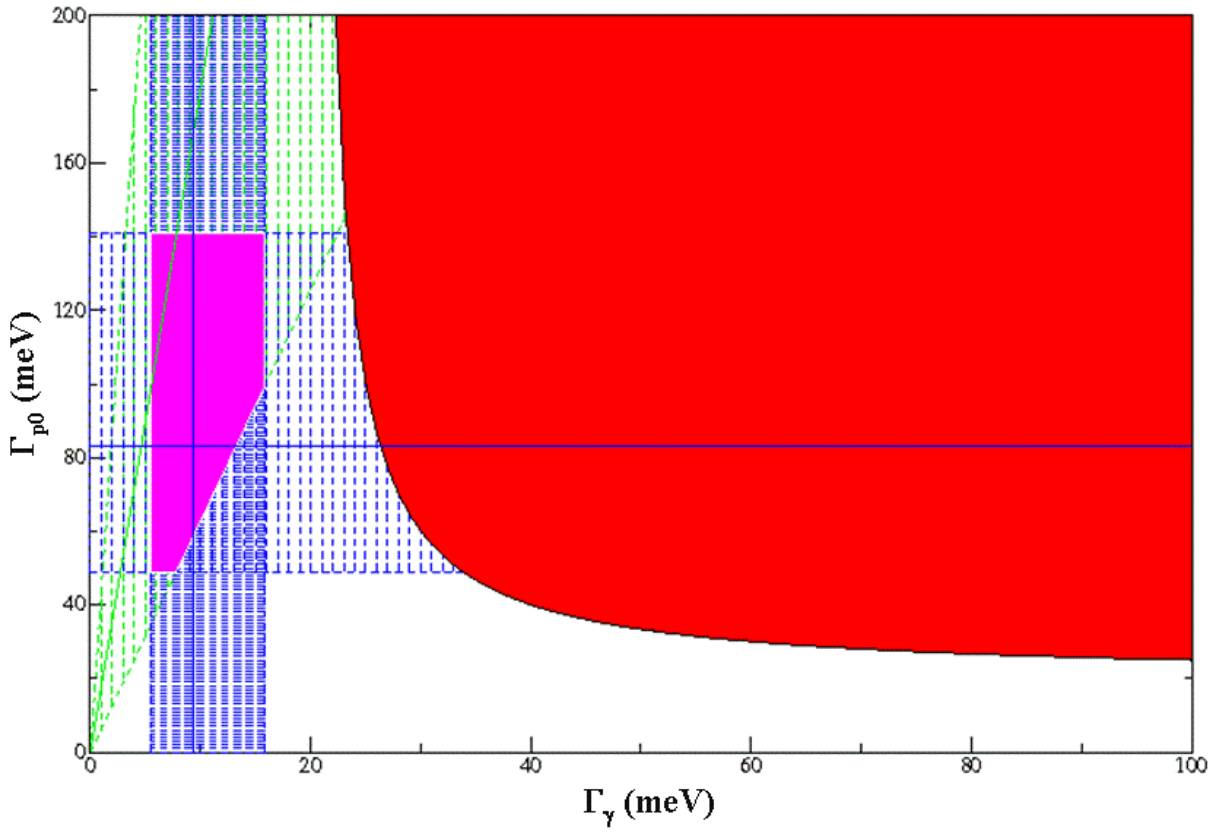

Figure 5.1. Semi-exclusion/inclusion plot comparing the experimental limits with the calculated partial widths for the 2.645 MeV state with $J^\pi = 1^+$. The experimental Γ_p/Γ_γ is the diagonal green line with the 1-σ upper and lower limits shaded in green. The experimental upper limit on $\omega\gamma$ is the black curve with the restricted area to the upper right shaded in red. The calculated partial widths are shown as blue lines with the uncertainties shaded in blue. The pink shaded area defines the region where the calculated partial widths and the measured branching ratio overlap.

For the $J^\pi = 1^+$ assignment (Figure 5.1), Γ_{p1} is negligible and therefore the measurement of Γ_p/Γ_γ is a measure of $\Gamma_{p0}/\Gamma_\gamma$. However, for $J^\pi = 3^+$ Γ_{p1} is significant, in fact dominant, and therefore the error in Γ_{p1} has to be taken into account. Again, this error is taken to be a factor of 1.7. The effect of this uncertainty on $\omega\gamma$ is illustrated by the dashed black lines in Figure 5.2.

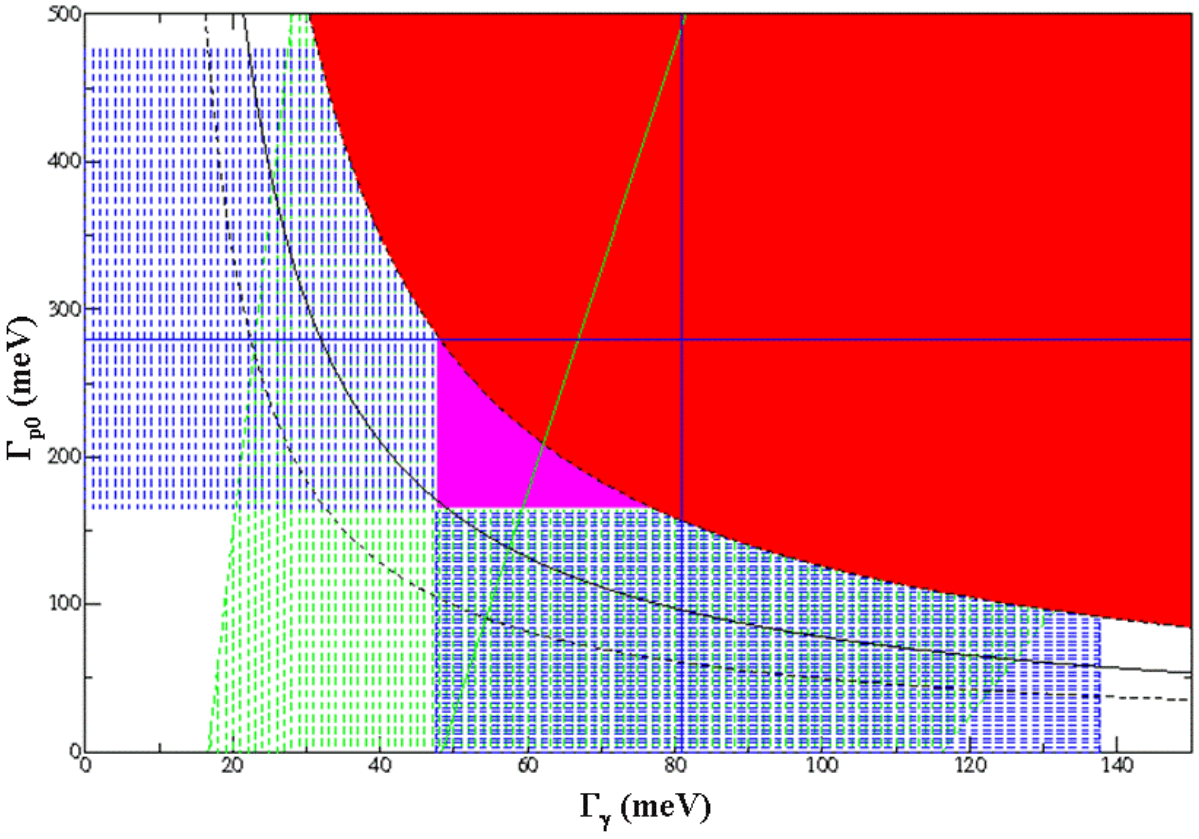

Figure 5.2. Same as Figure 5.1 calculated for $J^\pi = 3^+$. Here the uncertainty in $\omega\gamma$ due to the uncertainty in Γ_{p1} is indicated by the dashed black curves.

The evidence about the spin of the 2.645 MeV state can be summarized as follows:

Favoring $J^\pi = 3^+$:

(1) The re-analysis by Clarke et al. [**62**] comparing the ^{20}Ne(^{3}He,t)^{20}Na and the ^{20}Ne(t,^{3}He)^{20}F mirror reactions.

(2) The absence of $\ell = 0$ strength in Anderson's [**63**] ^{20}Ne(p,n)^{20}Na data, and in the ^{22}Mg β-decay experiments. Some have argued that these could be explained by a 1^+ intruder state configuration.

(3) Brown and Fortune [**61, 82**] have used Shell Model calculations to argue that the Coulomb shift is too large for the proposed 1^+ analog state in ^{20}F.

Favoring $J^\pi = 1^+$:

(1) ^{20}Ne(^{3}He,t)^{20}Na angular distributions by Kubono and Lamm [**55, 58**].

(2) ^{20}Ne(p,n)^{20}Na angular distributions by Kubono [**56**].

(3) Calculated resonance strength, $\omega\gamma$, using a combination of shell-model calculations and properties of states in ^{20}F compared to the experimental upper limit. This was the conclusion of Vancraeynest [**9**] and is the result of the Fortune [**82**] calculation if the latest data is used.

(4) Fortune and Bishop's $2J + 1$ data [**10**] confirming the spin of the proposed analog state in ^{20}F as $J^\pi = 1^+$.

(5) The absence of observed ^{20}Na-t coincidences feeding the 2.845 MeV state in the current branching ratio experiment favors $J^\pi = 3^+$ for this state, inferring that the 2.645 MeV state is therefore $J^\pi = 1^+$ [current work].

5.2. Outlook

The branching ratios, Γ_p/Γ_γ, were measured for the 2.645 and the 2.849 MeV states in ^{20}Na by populating the states via the ^{3}He(^{20}Ne,t)^{20}Na* reaction at 4.5 MeV per nucleon and observing the heavy particle recoils in coincidence with the tritons. The observation of ^{20}Na from the 2.645 MeV state represents, for the first time, an observation of the γ-decay of this state.

While the totality of evidence appears to favor the$J^\pi = 1^+$ assignment for the 2.645 MeV state and $J^\pi = 3^+$ for the 2.849 MeV state in ^{20}Na it cannot be said that the issue has been settled. Possible improvements to the present experiment would include:

1. Addition of particle identification for the light particle, e.g. adding a *dE/dx* detector to identify the light particle.

2. Thicker DSSD's that would stop all of the tritons of interest. While such detectors are presently not commercially available, one would expect that they will become available in the not too distant future.

3. Better angular and energy resolution so that the inelastic scattering could be observed, thus providing a measure of Γ_{p1}.

Even if all of these improvements could be made it is not certain that the spin of the ^{20}Na 2.645 MeV state, much less the resonance strength, would be definitively established. A more fruitful path would be another attempt at measuring the resonance capture directly. The gamma decay of the state observed here implies that the resonance strength is within about a factor of two of the present upper limit. Therefore, there is a good chance that sufficient improvements over previous measurements could be made so that the capture could be observed and the role of the radiative capture through the 2.645 MeV state in ^{20}Na in the breakout from the hot CNO cycle to the *rp*-process could be definitively established.

References

[1] M. Wiescher, J. Görres, and H. Schatz. Break-out reactions from the CNO cycles. *Journal of Physics G: Nuclear and Particle Physics*, 25(6):R133–R161, 1999.

[2] Claus E. Rolfs and William S. Rodney. *Cauldrons in the Cosmos*. The University of Chicago Press, Chicago and London, 1988.

[3] A. E. Champagne and M. Wiescher. Explosive hydrogen burning. *Annual Review of Nuclear and Particle Science*, 42:39–76, 1992.

[4] S. Kubono. Nuclear Astrophysics with Radioactive Nuclear Beams. *Progress of Theoretical Physics*, 96:275–306, August 1996.

[5] B. Harss, R. C. Pardo, K. E. Rehm, F. Borasi, J. P. Greene, R. V. F. Janssens, C. L. Jiang, J. Nolen, M. Paul, J. P. Schiffer, R. E. Segel, J. Specht, T. F. Wang, P. Wilt, and B. Zabransky. Production of radioactive ion beams using the in-flight technique. *Review of Scientific Instruments*, 71:380–387, February 2000.

[6] D. Groombridge, A. C. Shotter, W. Bradfield-Smith, S. Cherubini, T. Davinson, A. Di Pietro, J. Görres, J. S. Graulich, A. M. Laird, P. Leleux, A. Musumarra, A. Ninane, A. N. Ostrowski, J. Rahighi, H. Schatz, M. Wiescher, and P. J. Woods. Breakout from the hot CNO cycle via the ^{18}Ne(α,p)^{21}Na reaction. II. Extended energy range $E_{c.m.} \sim 1.7 - 2.9$ MeV . *Phys. Rev. C*, 66(5):055802, Nov 2002.

[7] W. Bradfield-Smith, T. Davinson, A. DiPietro, A. M. Laird, A. N. Ostrowski, A. C. Shotter, P. J. Woods, S. Cherubini, W. Galster, J. S. Graulich, P. Leleux, L. Michel, A. Ninane, J. Vervier, J. Görres, M. Wiescher, J. Rahighi, and J. Hinnefeld. Breakout from the hot CNO cycle via the ^{18}Ne(α,p)^{21}Na reaction. *Phys. Rev. C*, 59(6):3402–3409, Jun 1999.

[8] Tilley D. R., Cheves C. M., Kelley J. H., Raman S., and Weller H. R. Energy levels of light nuclei, A = 20. *Nuclear Physics A*, 636:249–364 28 29 30 31, 29 June 1998.

[9] G. Vancraeynest, P. Decrock, M. Gaelens, M. Huyse, P. Van Duppen, C. R. Bain, T. Davinson, R. D. Page, A. C. Shotter, P. J. Woods, F. Binon, P. Duhamel, J. Vanhorenbeeck, R. Coszach, Th. Delbar, W. Galster, J. S. Graulich, P. Leleux, E. Liénard, P. Lipnik, C. Michotte, A. Ninane, J. Vervier, H. Herndl, H. Oberhummer, Cs. Sükösd, and M. Wiescher. ^{19}Ne(p,γ)^{20}Na and ^{19}Ne(d,n)^{20}Na reactions and its astrophysical implications for the transition of the hot CNO cycle to the *rp* process. *Phys. Rev. C*, 57(5):2711–2723, May 1998.

[10] H. T. Fortune and J. N. Bishop. Study of the ^{14}N(^{7}Li, p)^{20}F reaction. *Nuclear Physics A*, 293(1 - 2):221–229, Dec 1977.

[11] S. Raman, E. K. Warburton, J. W. Starner, E. T. Jurney, J. E. Lynn, P. Tikkanen, and J. Keinonen. Spectroscopy of ^{20}F levels. *Phys. Rev. C*, 53(2):616–646, Feb 1996.

[12] N. M. Clarke, P. R. Hayes, M. B. Becha, C. N. Pinder, and S. Roman. BRIEF REPORT: Charge exchange reactions leading to the mirror nuclei ^{20}Na and ^{20}F. *Journal of Physics G Nuclear Physics*, 16:1547–1552, Oct 1990.

[13] E. M. Burbidge, G. R. Burbidge, W. A. Fowler, and F. Hoyle. Synthesis of the Elements in Stars. *Reviews of Modern Physics*, 29:547–650, 1957.

[14] R. K. Wallace and S. E. Woosley. Explosive hydrogen burning. *ApJ. Supp.*, 45:389–420, Feb 1981.

[15] Donald D. Clayton. *Principles of Stellar Evolution and Nucleosynthesis*. The University of Chicago Press, Chicago and London, 1984.

[16] H. A. Bethe. Energy Production in Stars. *Phys. Rev.*, 55(5):434–456, Mar 1939.

[17] C. F. von Weizsäcker. About the Transmutation of Elements inside of Stars. *Phys. Z.*, 39:633–646, Sep 1938.

[18] B. Warner. Observations of Dwarf Novae. In P. Eggleton, S. Mitton, and J. Whelan, editors, *Structure and Evolution of Close Binary Systems*, volume 73 of *IAU Symposium*, pages 85–140. D. Reidel Publishing Co., 1976.

[19] J. S. Gallagher and S. Starrfield. Theory and observations of classical novae. *Annual Review of Astronomy and Astrophysics*, 16:171–214, 1978.

[20] S. Starrfield, W. M. Sparks, and J. W. Truran. CNO abundances and hydrodynamic models of the nova outburst. II - 1.00 solar mass models with enhanced carbon and oxygen. *ApJ. Supp.*, 28:247–270, August 1974.

[21] H. L. Ravn. Experiments with intense secondary beams of radioactive ions. *Physics Reports*, 54:201–259, Aug 1979.

[22] H. H. Heckman, D. E. Greiner, P. J. Lindstrom, and F. S. Bieser. Fragmentation of Nitrogen-14 Nuclei at 2.1 GeV per Nucleon. *Science*, 174:1130–1131, December 1971.

[23] H. H. Heckman, D. E. Greiner, P. J. Lindstrom, and F. S. Bieser. Fragmentation of ^{14}N Nuclei at 29 GeV: Inclusive Isotope Spectra at 0^0. *Phys. Rev. Lett.*, 28(14):926–929, Apr 1972.

[24] H. A. Grunder, W. D. Hartsough, and E. J. Lofgren. Acceleration of Heavy Ions at the Bevatron. *Science*, 174:1128–1129, December 1971.

[25] R. C. Haight, G. J. Mathews, R. M. White, L. A. Aviles, and S. E. Woodward. A new system for astrophysical nuclear reaction studies with radioactive ion beams. *Nuclear Instruments and Methods*, 212:245–247, 1983.

[26] R. N. Boyd, L. Rybarcyk, H. J. Hausman, W. Kim, and P. Schmalbrock. Uses of radioactive ion beams in astrophysical research. *Nuclear Instruments and Methods in Physics Research B*, 10:378–381, May 1985.

[27] M. S. Smith and K. Ernst Rehm. Nuclear Astrophysics Measurements with Radioactive Beams. *Annual Review of Nuclear and Particle Science*, 51:91–130, 2001.

[28] Boris Harss. *Development of a Radioactive ^{17}F Beam and its use in Nuclear Astrophysics Experiments*. PhD thesis, Technischen Universität München, Jul 2001.

[29] D. J. Morrissey and B. M. Sherrill. Radioactive nuclear beam facilities based on projectile fragmentation. *Philosophical Transactions of the Royal Society of London A*, 356:1985–2006, 1998.

[30] K. E. Rehm, I. Ahmad, J. Blackmon, F. Borasi, J. Caggiano, A. Chen, C. N. Davids, J. Greene, B. Harss, A. Heinz, D. Henderson, R. V. F. Janssens, C. L. Jiang, J. Nolen, R. C. Pardo, P. Parker, M. Paul, J. P. Schiffer, R. E. Segel, D. Seweryniak, R. H. Siemssen, M. S. Smith, J. Uusitalo, T. F. Wang, and I. Wiedenhöver. Experiments with radioactive beams at ATLAS. In *American Institute of Physics Conference Series*, volume 576 of *American Institute of Physics Conference Series*, pages 261–264, July 2001.

[31] James Ziegler. *Stopping Ranges of Ions in Matter*, 2006, http://www.srim.org.

[32] W. N. Catford, D. M. Pringle, D. G. Lewis, A. E. Smith, E. F. Garman, I. F. Wright, and J. Lukasiak. Kinematic coincidence technique to identify γ-decaying

highly excited states in light nuclei. *Nuclear Instruments and Methods in Physics Research A*, 247:367–378, June 1986.

[33] C. Schiessl, W. Wagner, K. Hartel, P. Kienle, H. Korner, W. Mayer, and K. Rehm. A bragg-curve spectroscopy detector. *Nuclear Instruments and Methods*, 192:291–294, February 1982.

[34] K. E. Rehm, M. Paul, A. D. Roberts, D. J. Blumenthal, J. Gehring, D. Henderson, C. L. Jiang, J. Nickles, J. Nolen, R. C. Pardo, J. P. Schiffer, and R. E. Segel. Study of the ^{18}F(p,α)^{15}O reaction at astrophysical energies using a ^{18}F beam. *Phys. Rev. C*, 52(2):R460–R463, Aug 1995.

[35] K. E. Rehm, M. Paul, A. D. Roberts, C. L. Jiang, D. J. Blumenthal, S. M. Fischer, J. Gehring, D. Henderson, J. Nickles, J. Nolen, R. C. Pardo, J. P. Schiffer, and R. E. Segel. Astrophysical reaction rate for the ^{18}F(p,α)^{15}O reaction. *Phys. Rev. C*, 53(4):1950–1954, Apr 1996.

[36] K. E. Rehm, C. L. Jiang, M. Paul, D. Blumenthal, L. A. Daniel, C. N. Davids, P. Decrock, S. M. Fischer, D. Henderson, C. Lister, J. Nickles, J. Nolen, R. C. Pardo, J. P. Schiffer, D. Seweryniak, and R. E. Segel. Exploring the ^{18}F(p,γ)^{19}Ne gateway to the formation of heavy elements in hot stars. *Phys. Rev. C*, 55(2):R566–R569, Feb 1997.

[37] R. V. Wagoner. Synthesis of the Elements Within Objects Exploding from Very High Temperatures. *ApJ. Supp.*, 18:247, June 1969.

[38] S. E. Woosley, W. A. Fowler, J. A. Holmes, and B. A. Zimmerman. Semiempirical Thermonuclear Reaction-Rate Data for Intermediate-Mass Nuclei. *Atomic Data and Nuclear Data Tables*, 22:371, 1978.

[39] B. Harss, C. L. Jiang, K. E. Rehm, J. P. Schiffer, J. Caggiano, P. Collon, J. P. Greene, D. Henderson, A. Heinz, R. V. F. Janssens, J. Nolen, R. C. Pardo, T. Pennington, R. H. Siemssen, A. A. Sonzogni, J. Uusitalo, I. Wiedenhöver, M. Paul, T. F. Wang, F. Borasi, R. E. Segel, J. C. Blackmon, M. Smith, A. Chen, and P. Parker. Widths of astrophysically important resonances in ^{18}Ne. *Phys. Rev. C*, 65(3):035803, Feb 2002.

[40] K. Langanke, M. Wiescher, W. A. Fowler, and J. Görres. A new estimate of the ^{19}Ne(p,γ)^{20}Na and ^{15}O(α,γ)^{19}Ne reaction rates at stellar energies. *Astrophysical Journal*, 301:629–633, February 1986.

[41] Z. Q. Mao, H. T. Fortune, and A. G. Lacaze. Alpha-particle spectroscopic strengths in ^{19}F and ^{20}Ne. *Phys. Rev. C*, 53(3):1197–1204, Mar 1996.

[42] W. R. Dixon, T. J. M. Symons, A. A. Pilt, K. W. Allen, C. H. Zimmerman, F. Watt, and S. P. Dolan. The lifetime of the 3907 keV state of ^{19}F. *Physics Letters A*, 62:479–482, October 1977.

[43] P. V. Magnus, M. S. Smith, A. J. Howard, P. D. Parker, and A. E. Champagne. Measurement of ^{15}O(α,γ)^{19}Ne resonance strengths. *Nuclear Physics A*, 506:332–345, January 1990.

[44] S. Kubono, Y. Yanagisawa, T. Teranishi, S. Kato, Y. Kishida, S. Michimasa, Y. Ohshiro, S. Shimoura, K. Ue, S. Watanabe, and N. Yamazaki. New low-energy RIB separator CRIB for nuclear astrophysics. *European Physical Journal A*, 13:217–220, 2002.

[45] A. M. Laird, A. N. Ostrowski, S. Cherubini, C. Spitaleri, M. Aliotta, T. Davinson, A. Di Pietro, P. Figuera, W. Galster, J. S. Graulich, D. Groombridge, J. Hinnefeld, M. Lattuada, P. Leleux, A. Musumarra, A. Ninane, M. G. Pellegriti, A. C. Shotter, A. Tumino, J. Vervier, and P. Woods. Hot CNO breakout: Status of the d(^{18}Ne,p)^{19}Ne*(α)^{15}O reaction. *Nuclear Physics A*, 688:134–137, May 2001.

[46] J. D. Garrett, R. Middleton, and H. T. Fortune. Hole States in ^{19}Ne. *Phys. Rev. C*, 2:1243–1254, October 1970.

[47] K. E. Rehm, A. H. Wuosmaa, C. L. Jiang, J. Caggiano, J. P. Greene, A. Heinz, D. Henderson, R. V. F. Janssens, E. F. Moore, G. Mukherjee, R. C. Pardo, T. Pennington, J. P. Schiffer, R. H. Siemssen, M. Paul, L. Jisonna, and R. E. Segel. Branching ratio $\Gamma_\alpha/\Gamma_\gamma$ of the 4.033 MeV $3/2^+$ state in ^{19}Ne. *Phys. Rev. C*, 67(6):065809, Jun 2003.

[48] B. Davids, A. M. van den Berg, P. Dendooven, F. Fleurot, M. Hunyadi, M. A. de Huu, K. E. Rehm, R. E. Segel, R. H. Siemssen, H. W. Wilschut, H. J. Wörtche, and A. H. Wuosmaa. α-decay branching ratios of near-threshold states in ^{19}Ne and the astrophysical rate of ^{15}O$(\alpha, \gamma)^{19}$Ne . *Phys. Rev. C*, 67(1):012801, Jan 2003.

[49] J. L. Fisker, J. Görres, M. Wiescher, and B. Davids. The Importance of ^{15}O$(\alpha, \gamma)^{19}$Ne to X-Ray Bursts and Superbursts. *Astrophysical Journal*, 650:332–337, October 2006.

[50] W. P. Tan, J. L. Fisker, J. Görres, M. Couder, and M. Wiescher. ^{15}O$(\alpha, \gamma)^{19}$Ne Breakout Reaction and Impact on X-Ray Bursts. *Physical Review Letters*, 98(24):242503, June 2007.

[51] W. P. Tan, J. Görres, J. Daly, M. Couder, A. Couture, H. Y. Lee, E. Stech, E. Strandberg, C. Ugalde, and M. Wiescher. Lifetime of the astrophysically important 4.03-MeV state in ^{19}Ne. *Phys. Rev. C*, 72(4):041302, October 2005.

[52] R. Kanungo, T. K. Alexander, A. N. Andreyev, G. C. Ball, R. S. Chakrawarthy, M. Chicoine, R. Churchman, B. Davids, J. S. Forster, S. Gujrathi, G. Hackman, D. Howell, J. R. Leslie, A. C. Morton, S. Mythili, C. J. Pearson, J. J. Ressler, C. Ruiz, H. Savajols, M. A. Schumaker, I. Tanihata, P. Walden, and S. Yen. Lifetime of ^{19}Ne*(4.03 MeV). *Phys. Rev. C*, 74(4):045803, October 2006.

[53] S. Mythili, B. Davids, T. K. Alexander, G. C. Ball, M. Chicoine, R. S. Chakrawarthy, R. Churchman, J. S. Forster, S. Gujrathi, G. Hackman, D. Howell, R. Kanungo, J. R. Leslie, E. Padilla, C. J. Pearson, C. Ruiz, G. Ruprecht, M. A. Schumaker, I. Tanihata, C. Vockenhuber, P. Walden, and S. Yen. Lifetimes of states in Ne19 above the ^{15}O+α breakup threshold. *Phys. Rev. C*, 77(3):035803, March 2008.

[54] S. Kubono, N. Ikeda, M. Yasue, T. Nomura, Y. Fuchi, H. Kawashima, S. Kato, H. Orihara, T. Shinozuka, H. Ohnuma, H. Miyatake, and T. Shimoda. Experimental determination of the Ne-19(p, gamma)Na-20 reaction rate and the breakout problem from the hot CNO cycle. *Zeitschrift für Physik A Hadrons and Nuclei*, 331:359–360, Sep 1988.

[55] S. Kubono, H. Orihara, S. Kato, and T. Kajino. Experimental determination of the ^{19}Ne(p,γ)^{20}Na reaction rate and the breakout problem from the hot CNO cycle. *Astrophysical Journal*, 344:460–463, September 1989.

[56] Shigeru Kubono. Experimental Study of ^{20}Na and Breakout Off the Hot-CNO Cycle. In S. Kubono, M. Ishihara, and T. Nomura, editors, *Proceedings of the International Symposium on Heavy ion Physics and Nuclear Astrophysical Problems*, IAU Symposium, pages 83–95. World Scientific, 1989.

[57] L. O. Lamm, C. P. Browne, J. Görres, M. Wiescher, and A. A. Rollefson. Level structure of ^{20}Na near the proton threshold. *Zeitschrift für Physik A Hadrons and Nuclei*, 327:239–240, 1987.

[58] L. O. Lamm, C. P. Browne, J. Görres, S. M. Graff, M. Wiescher, A. A. Rollefson, and B. A. Brown. The level structure of ^{20}Na and the impact upon the stellar reaction rate for ^{19}Ne(p,γ)^{20}Na. *Nuclear Physics A*, 510:503–517, April 1990.

[59] M. S. Smith, P. V. Magnus, K. I. Hahn, A. J. Howard, P. D. Parker, A. E. Champagne, and Z. Q. Mao. A high-resolution study of the ^{20}Ne(^{3}He, t)^{20}Na reaction and the ^{19}Ne(p,γ)^{20}Na reaction rate. *Nuclear Physics A*, 536:333–348, January 1992.

[60] M. A. Hofstee, J. C. Blackmon, A. E. Champagne, N. P. T. Bateman, Y. Butt, P. D. Parker, S. Utku, K. Yildiz, M. S. Smith, R. B. Vogelaar, and A. J. Howard. Measurement of the $\Gamma_\gamma/\Gamma_{tot}$ of the $E_x = 2.646$ MeV State in ^{20}Na. In M. Busso, C. M.

Raiteri, and R. Gallino, editors, *Nuclei in the Cosmos III*, volume 327 of *American Institute of Physics Conference Series*, page 195, 1995.

[61] B. A. Brown, A. E. Champagne, H. T. Fortune, and R. Sherr. Nature of the ^{20}Na 2646-keV level and the stellar reaction rate for ^{19}Ne(p,γ)^{20}Na. *Phys. Rev. C*, 48(3):1456–1459, Sep 1993.

[62] N. M. Clarke, S. Roman, C. N. Pinder, and P. R. Hayes. A comparison of angular distributions for charge exchange reactions to analogue states in ^{20}Na and ^{20}F. *Journal of Physics G Nuclear Physics*, 19:1411–1416, September 1993.

[63] B. D. Anderson, B. Wetmore, A. R. Baldwin, L. A. C. Garcia, D. M. Manley, R. Madey, J. W. Watson, W. M. Zhang, B. A. Brown, C. C. Foster, and Y. Wang. Excitation of the 2.65 MeV state in the ^{20}Ne(p,n)^{20}Na reaction at 135 MeV. *Phys. Rev. C*, 52(4):2210–2215, Oct 1995.

[64] S. Kubono, N. Ikeda, Y. Funatsu, M. H. Tanaka, T. Nomura, H. Orihara, S. Kato, M. Ohura, T. Kubo, N. Inabe, A. Yoshida, T. Ichihara, M. Ishihara, I. Tanihata, H. Okuno, T. Nakamura, S. Shimoura, H. Toyokawa, C. C. Yun, H. Ohnuma, K. Asahi, A. Chakrabarti, T. Mukhopadhyay, and T. Kajino. Decay property of ^{20}Na for the onset mechanism of the rapid-proton process. *Phys. Rev. C*, 46(1):361–365, Jul 1992.

[65] J. Görres, M. Wiescher, K. Scheller, D. J. Morrissey, B. M. Sherrill, D. Bazin, and J. A. Winger. β-delayed proton decay of ^{20}Mg and its astrophysical implications. *Phys. Rev. C*, 46(3):R833–R837, Sep 1992.

[66] A. Piechaczek, M. F. Mohar, R. Anne, V. Borrel, B. A. Brown, J. M. Corre, D. Guillemaud-Mueller, R. Hue, H. Keller, S. Kubono, V. Kunze, M. Lewitowicz, P. Magnus, A. C. Mueller, T. Nakamura, M. Pfützner, E. Roeckl, K. Rykaczewski, M. G. Saint-Laurent, W.-D. Schmidt-Ott, and O. Sorlin. Beta-decay of ^{20}Mg. *Nuclear Physics A*, 584:509–531, February 1995.

[67] W.-T. Chou, E. K. Warburton, and B. A. Brown. Gamow-Teller beta-decay rates for A$\leq$18 nuclei. *Phys. Rev. C*, 47(1):163–177, Jan 1993.

[68] R. D. Page, G. Vancraeynest, A. C. Shotter, M. Huyse, C. R. Bain, F. Binon, R. Coszach, T. Davinson, P. Decrock, Th. Delbar, P. Duhamel, M. Gaelens, W. Galster, P. Leleux, I. Licot, E. Lienard, P. Lipnik, C. Michotte, A. Ninane, P. J. Sellin, Cs. Sükösd, P. Van Duppen, J. Vanhorenbeeck, J. Vervier, M. Wiescher, and P. J. Woods. First Experimental Limit on the ^{19}Ne(p,γ)^{20}Na Resonance Strength, of Astrophysical Interest. *Phys. Rev. Lett.*, 73(23):3066–3069, Dec 1994.

[69] C. Michotte, C. R. Bain, F. Binon, R. Coszach, T. Davinson, P. Decrock, Th. Delbar, P. Duhamel, M. Gaelens, W. Galster, M. Graulich, J. S.and Huyse, P. Leleux, E. Lienard, P. Lipnik, A. Ninane, A. C. Shotter, Cs. Sükösd, G. Vancraeynest, P. Van Duppen, J. Vanhorenbeeck, J. Vervier, M. Wiescher, and P. J. Woods. New limits on the ^{19}Ne(p,γ)^{20}Na astrophysical reaction rate from direct measurements using radioactive beams. *Physics Letters B*, 381:402–406, Jul 1996.

[70] M. Couder, C. Angulo, E. Casarejos, P. Demaret, P. Leleux, and F. Vanderbist. New direct study of the ^{19}Ne(p,γ)^{20}Na reaction cross section. *Phys. Rev. C*, 69(2):022801, Feb 2004.

[71] H. T. Fortune and R. R. Betts. Weak states in ^{19}F(d,p)^{20}F. *Phys. Rev. C*, 10(4):1292–1298, Oct 1974.

[72] R. Medoff, L. R. Medsker, S. C. Headley, and H. T. Fortune. Additional 1^+ states in ^{20}F. *Phys. Rev. C*, 14(1):1–3, Jul 1976.

[73] P. A. Quin, G. A. Bissinger, and C. P. R. The low-lying levels of ^{20}F. *Nuclear Physics A*, 155:495–512, Oct 1970.

[74] L. A. Alexander, W. K. Collins, B. P. Hichwa, J. C. Lawson, D. S. Longo, E. D. Berners, and P. R. Chagnon. Gamma-Ray Transitions in ^{20}F. *Phys. Rev. C*, 6(3):817–819, Sep 1972.

[75] D. E. Alburger, G. Wang, and E. K. Warburton. Beta decay of ^{20}O. *Phys. Rev. C*, 35(4):1479–1484, Apr 1987.

[76] P. Hungerford, T. von Egidy, H. H. Schmidt, S. A. Kerr, H. G. Börner, and E. Monnand. The ^{19}F(n,γ)^{20}F reaction. *Zeitschrift fur Physik*, 313:339–347, December 1983.

[77] T. J. Kennett, W. V. Prestwich, and J. S. Tsai. A re-examination of the ^{19}F(n,γ)^{20}F reaction. *Canadian Journal of Physics*, 65:1111–1118, September 1987.

[78] P. Descouvemont and D. Baye. The ^{20}F and ^{20}Na nuclei and the ^{19}Ne(p,γ)^{20}Na reaction in a microscopic three-cluster model. *Nuclear Physics A*, 517:143–158, Oct 1990.

[79] E. K. Warburton and B. A. Brown. Effective interactions for the $0p1s0d$ nuclear shell-model space. *Phys. Rev. C*, 46(3):923–944, Sep 1992.

[80] E. K. Warburton, I. S. Towner, and B. A. Brown. First-forbidden β decay: Meson-exchange enhancement of the axial charge at A$\sim$ 16. *Phys. Rev. C*, 49(2):824–839, Feb 1994.

[81] B. H. Wildenthal. Empirical strengths of spin operators in nuclei. *Progress in Particle and Nuclear Physics*, 11:5–51, 1984.

[82] H. T. Fortune, R. Sherr, and B. A. Brown. $\omega\gamma$ for ^{19}Ne(p,γ)^{20}Na(2.64 MeV). *Phys. Rev. C*, 61(5):057303, Apr 2000.

[83] J. Görres, J. Meissner, J. G. Ross, K. W. Scheller, S. Vouzoukas, M. Wiescher, and J. D. Hinnefeld. Lifetimes of levels in ^{20}F. *Phys. Rev. C*, 50(3):R1270–R1271, Sep 1994.

[84] T. Moog. *Experimenter's Guide To Daphne Data Acquisition System*. Argonne National Laboratory, revised 1/25/1995 edition, Jul 1988.

[85] H. Ernst. ENELOSS. Technical report, Argonne National Laboratory, Oct 1981, modified by K. Lesko (1984).

[86] Paul F. Velleman. *DataDesk version 6.0 Handbook*. Data Description, Inc., 1997, http://www.datadesk.com.

[87] N. Gehrels. Confidence limits for small numbers of events in astrophysical data. *Astrophysical Journal*, 303:336–346, Apr 1986.

[88] C. Iliadis, P. M. Endt, N. Prantzos, and W. J. Thompson. Explosive Hydrogen Burning of ^{27}Si, ^{31}S, ^{35}Ar, and ^{39}Ca in Novae and X-Ray Bursts. *Astrophysical Journal*, 524:434–453, October 1999.